博士論文

Development of Efficient and Semitransparent Perovskite Solar Cells by Nanooptical and Plasmonic Approaches

（ナノ光学およびプラズモニクスを利用した半透明ペロブスカイト太陽電池の開発と効率化）

金　揆昊

Table of contents

Chapter 1

Preface

1-1 Outline of the work

Due to the tremendous demand for the energy resources since industrial evolution, air pollution and the depletion of fossil fuels have become serious issues of mankind. Development of renewable energy resources can be one of the solution to the issues. Solar cells have attracted great attention as a clean and sustainable energy source because the amounts of solar energy are unlimited. Since the first invention of the solar cell in 1941,[1] power conversion efficiency (PCE) has been improved largely. Although solar cells have noticeable potentials, commercialization in market still lags behind pre-existing energy sources such as fossil fuels mainly because of the high costs of silicon-based materials.

The organic solar cells (OSCs) have been emerged by taking advantage of cost-effectiveness due to roll-to-roll and solution processing. However, the intrinsic limitation of absorption capacity and low diffusion length of electrons and holes of organic materials prevents OSCs from achieving high PCE. Metal nanoparticles (MNPs) can enhance the performances of the OSCs by localized surface plasmon resonance (LSPR).[2, 3] LSPR is the interaction between free electron oscillation of MNPs and electric field of incident light. Due to the near-field antenna and far-field scattering effects of LSPR, photocurrents of solar cells can be enhanced.

Recently, unprecedentedly superior solar cells have been developed, which are based on organic-inorganic hybrid perovskites. Despite their short history, the solar cells based on perovskites, which are named perovskite solar cells (PVSCs), have recorded the PCE of 22.1% in 2016.[4] Because of the simple process and the low cost of PVSCs comparable to OSCs, the PVSC is currently considered as an influential candidate for renewable energy resources. Though the PVSCs have many advantages regarding high PCE and low costs, several problems such as hysteresis, instability in air and low reproducibility still exist, which prevent being commercialized in the market.

In the present work, PVSCs with smooth and semi-transparent perovskite films have been proposed, and applied to semi-transparent PVSCs using a transparent electrode. For superior transparency of a perovskite layer, a novel method to suppress scattering of the perovskite surface has been developed, which can also improve moisture sensitivity during the fabrication process. Then, application of plasmonic MNPs to PVSCs also has been studied for further enhancement of photocurrents based on LSPR. The typical LSPR from MNPs cannot further increase absorption of the perovskite layer because perovskites have extremely high absorption coefficients. Thus, the shifting of plasmon peaks to the low absorption region of perovskite layer has been designed in this work.

In this chapter, the overall history and the principle of solar cells and the PVSCs are

introduced. Then, the semi-transparent solar cells, which are also one of the research topics in the present work, are dealt with. Further, the mechanism and the application of LSPR recent days are mentioned. Finally, the purpose of the present research is briefly explained.

1-2 Solar Cells

1-2-1 Current status of solar cells

Solar cells are devices that convert sunlight into electricity. The development of solar cells stemmed from the photovoltaic effect that has been discovered by Antoine Henri Becquerel. Since the first solar cell was invented in 1941, which are based on silicon, a variety of structures and materials have been used in solar cells.

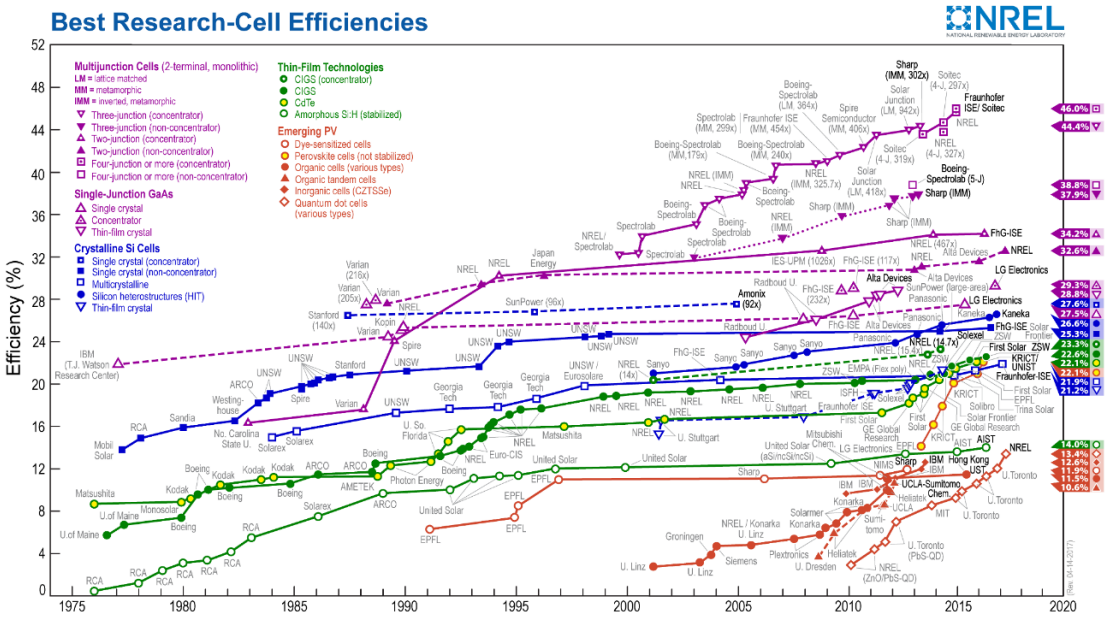

Figure 1-1. Best research-cell efficiencies. Reprinted with permission from Ref. 4. Copyright 2017 National Renewable Energy Laboratory (NREL).

Figure 1-1 shows the best efficiencies of various types of solar cells confirmed in national renewable energy laboratory (NREL). The high performance cells, of which the power conversion efficiency is over 25%, are composed of materials based on silicon or gallium arsenide (GaAs). Despite their high efficiencies, the use of solar cells as energy sources in the world is under 0.1%.[5] The application of solar cells is mostly confined in space industry, in which other energy sources cannot be utilized than solar energy. The low market share of solar cells are mainly caused by low cost performances compared to the other energy sources such as fossil fuels.

The emerging photovoltaics (PV), shown in the chart in Figure 1-1, such as dye-sensitized solar cells (DSSCs), organic solar cells (OSCs) and quantum dot cells (QDCs) have been considered breakthrough for cost inefficiency of PV by taking advantage of roll-to-roll and large area processing.[6]

Despite economic advantages of emerging PV, the development speeds still lag behind

those of silicon or GaAs-based solar cells mainly because of high resistance and low diffusion lengths of electrons and holes.[7] These intrinsic drawbacks hinder recording more than 15% of PCE, which is the requirement for commercialization in the market.

The advent of perovskite solar cells, in which organic-inorganic hybrid perovskites are employed, attracted great attentions due to the high value of PCE with low costs comparable to silicon-based solar cells. The potentials of PV have been raised and will boost the increase in market share of PV as next generation energy sources.

1-2-2 Principle of solar cells

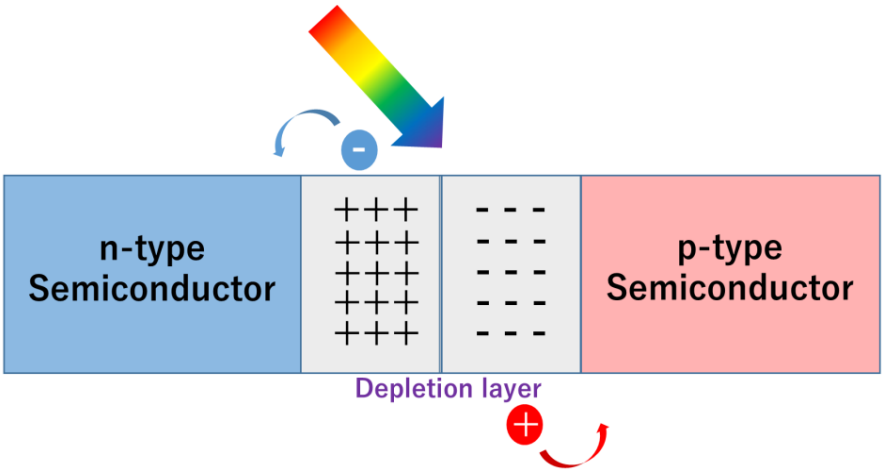

Figure 1-2. P-n junction and the charge separation by incident light.

Photo-induced charge separation at a p-n junction is the basic mechanism of the silicon-based PVs. A p-n junction is created by positioning a p-type semiconductor next to an n-type semiconductor. A depletion layer, which forms at the p-n junction, causes internal electric field and internal voltage. The rectification property of p-n junction is caused by the depletion layer, by which a diode is formed (Figure 1-2).

When the light is irradiated in the depletion layer of p-n junction, electron-hole (e-h) pairs are created, which eventually move toward each semi-conductor, generation photocurrents. This is a simple mechanism of PV. Thus, the basic structure of PV has many things in common with that of diode.

The current of solar cells can be expressed as eq. 1-1 based on integrated circuit model (Figure 1-3).[8]

$$I = I_0\left(exp^{\frac{q(V-IR_S)}{nkT}}\right) + \frac{V-IR_S}{R_{SH}} - I_{ph} \qquad \text{(eq. 1-1)}$$

(I: current, I_0: dark saturated current, q: elementary electronic charge, V: applied voltage,, n: ideal factor, k: Boltzmann's constant, T: temperature, R_S: series resistance, R_{SH}: parallel resistance, I_{ph}: photo-generated current)

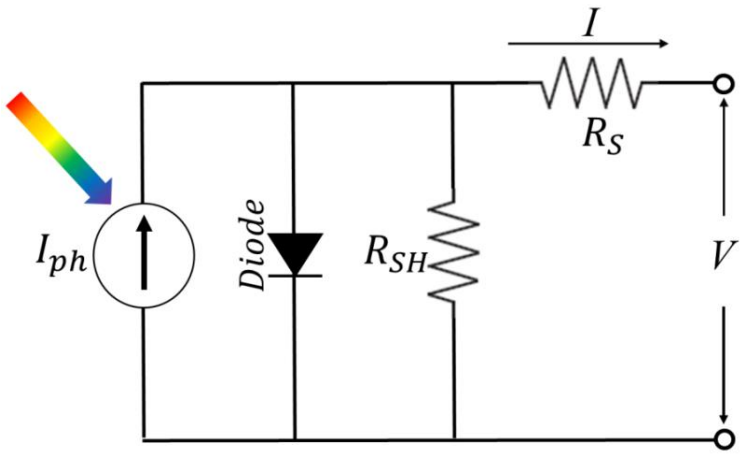

Figure 1-3. Integrated circuit model of solar cells.

As shown in eq. 1-1 and Figure 1-3, the equation of solar cells is based on the diode equation; the only difference is the addition of the parameter of I_{ph}, which is the currents created by irradiated light. The current-voltage (*I*-*V*) curves of solar cells based on eq 1-1 are shown in Figure 1-4a.

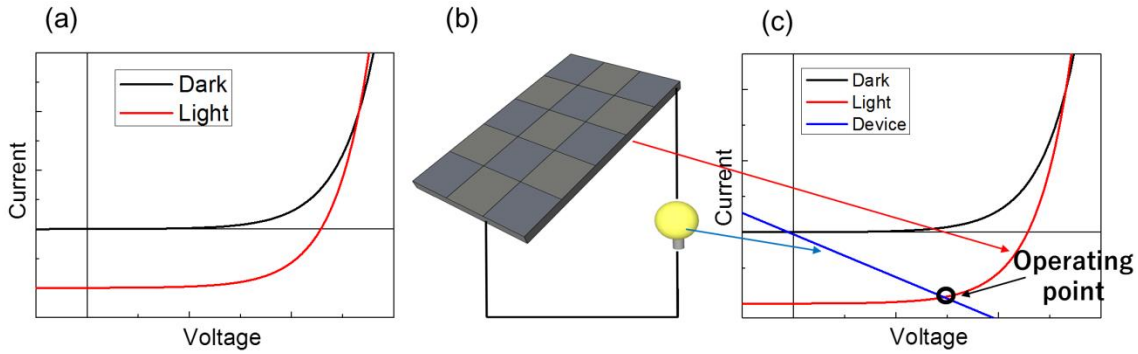

Figure 1-4. (a) *I-V* characteristics of solar cells under light and dark conditions. (b) Serial connection of the solar cell and the device operated by it. (c) The *I-V* characteristic of solar cells shown in Figure 1-4a and that of the device; intersection (black circle) is the operating point.

Without light irradiation, *I-V* characteristics resemble the diode curve, which shows the rectification property (the black line in Figure 1-4a). Under light irradiation, photocurrents are created (I_{ph}), which shift the curves along the vertical axis based on eq. 1-1, as shown by the red line in Figure 1-4. The shift is not parallel to the dark curve and the dark and light curves intersect. This is because the variable I exists both on the right and left terms (eq. 1-1). A solar cell is meaningful as a power sources when it is connected to a device such as light bulb (Figure 1-4b). In this case, the actual operating point of the solar cell is the intersection between the *I-V* curve of the device and that of the solar cell (Figure 1-4c). For any kinds of devices connected to a solar cell, the intersection point is always located in the fourth quadrant. Thus, when the performances of solar cells are evaluated, the *I-V* curves under light irradiation in the fourth quadrant should be analyzed. The next section explains the way the performances of solar cells are measured.

1-2-3 Measurement of solar cells

(a) Solar spectrum

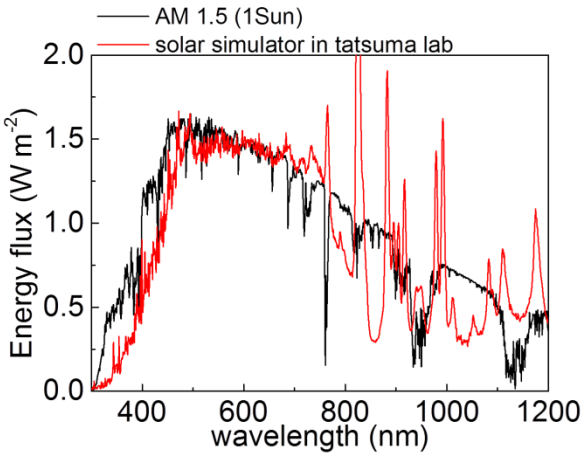

Figure 1-5. Spectrum of AM 1.5[9] and that of the solar simulator in Tatsuma lab.

The efficiency of a solar cell is calculated from the amount of the energy created by the solar cell over the power of sun light irradiated to the solar cell. In most cases, a solar simulator that follows AM 1.5 spectrum is used as a light source to measure a solar cell. Solar simulators that exactly match AM 1.5 is practically difficult to be realized because of the complex spectrum of sun light in wide range of wavelength (the black line in Figure 1-5). The spectrum of the solar simulator in Tatsuma lab was measured and compared to AM 1.5 (the red line in Figure 1-5). The spectrum of the solar

simulator in the range of λ < 800 nm matches quite well AM 1.5. However, in the range of λ > 800 nm, the spectrum of solar simulator somewhat deviates from that of AM 1.5. Therefore, when a solar cell which absorbs near IR light is measured, a solar simulator that matches the spectrum of AM 1.5 in the near IR range should be used, which could be quite costly. Fortunately, the absorption edge of most solar cells that are dealt with in this study is under 800 nm. Thus, the solar simulator in Figure 1-5 can be used for the measurements.

(b) Power conversion efficiency (PCE)

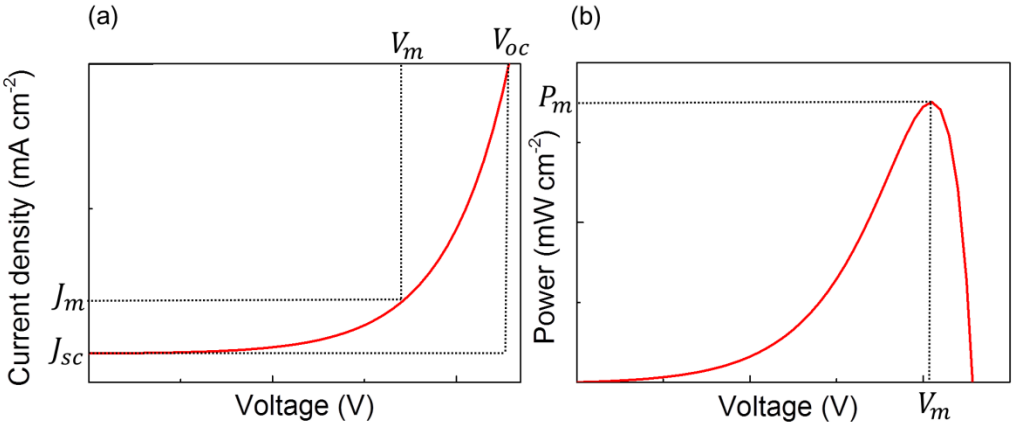

Figure 1-6. (a) The parameters from the *I-V* curves under light irradiation. (b) Power calculated from the multiplication of current density and voltage; J_m: current density at the maximum power point, J_{sc}: short circuit current density, V_m: voltage at the maximum power point, V_{oc}: open circuit voltage, P_m: maximum power.

As mentioned previously, the whole area of the fourth quadrant of the *I-V* curve of a solar cell under light is the operating area. The power of the solar cell is calculated from multiplication of the current density and the voltage. (Figure 1-6a,b)

The power conversion efficiency (PCE) is the maximum power of the solar cell (Figure 1-6b) over the power of the sun light incident onto the cell. The standard power of solar simulator based on AM 1.5 is 100 mW cm^{-2}, thereby the PCE is expressed as follows (eq. 1-2). For high PCE, improvements of J_{sc}, V_{oc} and FF are critical.

$$\text{PCE (\%)} = \frac{P_m}{100\ mW\ cm^{-2}} = \frac{J_{sc}*V_{oc}*FF}{100\ mW\ cm^{-2}} \quad \text{(eq. 1-2-1)}$$

$$\text{Fill factor } (FF) = \frac{J_{m}*V_{m}}{J_{sc}*V_{oc}} \quad \text{(eq. 1-2-2)}$$

(c) Incident photon-to-current conversion efficiency (IPCE)

IPCE indicates the external quantum efficiency of photocurrent generation at a given wavelength and expressed as eq.1-3.

$$\mathrm{IPCE}(\lambda)\ (\%) = \frac{the\ number\ of\ carriers\ flown\ per\ unit\ time\ and\ unit\ area}{the\ number\ of\ photons\ (\lambda)\ per\ unit\ time\ and\ unit\ area} * 100 \quad \text{(eq. 1-3)}$$

In order to evaluate IPCE, the currents of solar cells are measured without applied bias voltage (0 V) under the light at a given wavelength. The photon number of monochromatic light is not necessarily the same when the current of the solar cell increases linearly with the power of monochromatic light. However, when the IPCE of a low performance cell, the currents of which are normally non-linear to the power of monochromatic light, are measured, the photon number of each wavelength should be the same. The number of photon can be calculated from the power of light that is measured by spectrophotometry. The measurement of the number of photons should be done periodically as the power of light sources change in time.

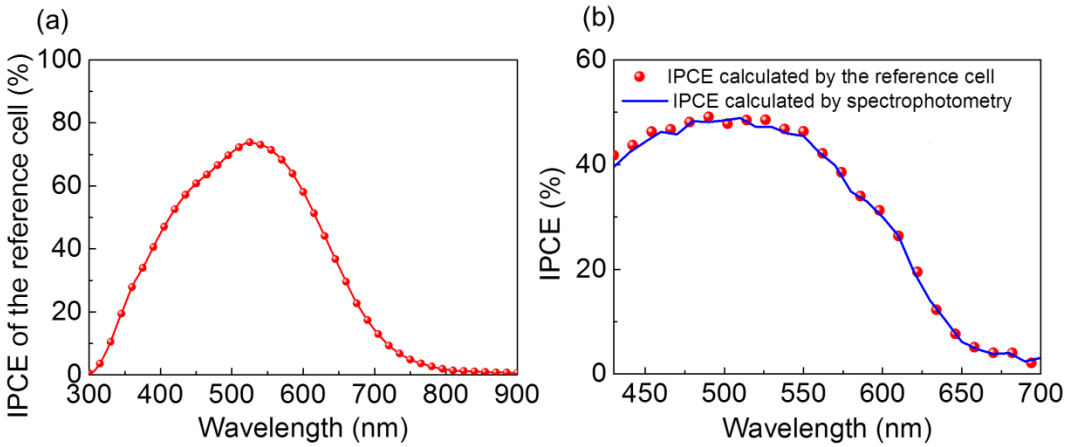

Figure 1-7. (a) IPCE spectrum of the reference cell based on Si. (b) IPCEs of organic solar cell calculated by the reference cell and the spectrophotometry.

Here, the easy measurement of the power of light is introduced for IPCE calculation by using a reference cell. The whole IPCE data used in this thesis have been measured based on the use of the reference cell. The reference cell is mainly used for the calibration of the power of solar simulator to check whether the power is 100 mW cm^{-2}. The reference cell used in Tatsuma lab is a Si-based solar cell (BS-520 BK, Bunkokeiki) and shows the IPCE spectrum shown in Figure 1-7a. The number of photon is inversely

calculated on the basis of eq. 1-4.

$$the\ number\ of\ photons\ (\lambda)\ per\ unit\ time\ and\ unit\ area = \frac{the\ number\ of\ carriers\ per\ unit\ time\ and\ unit\ area}{\mathrm{IPCE}(\lambda)\ (100\%)} * 100 \quad \text{(eq. 1-4)}$$

Thus, by measuring a current of the reference cell and the IPCE of the reference (Figure 1-7a), the number of photon at a given wavelength is easily obtained from eq. 1-4. In the case of BS-520 BK as a reference cell, the range of IPCE over 0% is between 300 to 800 nm. Thus, the region of the number of photon that can be calculated from the reference cell is confined in $300 < \lambda < 800$. If the photo-responsive range of the solar cells is beyond that of the reference cell, other reference cells that can respond to wide range of wavelength should be used. Figure 1-7b shows the IPCE spectra based on the number of photons obtained from the reference cell and the spectrophotometry of the organic solar cells consisting of ITO/polyethyleneimine (PEI)/P3HT (poly-3-hexylthiophene):PCBM (phenyl-C_{61}-butyric acid methyl ester)/molybdenim trioxide (MoO_3)/silver (Ag), which have the photo-responsive region smaller than that of the reference cell. Both IPCEs measured from different ways, have nearly the same value at each wavelength, implying that the number of photons obtained from the reference cell is accurate. For this reason, the whole IPCE data used here have been based on the photon number calculated from the reference cell.

The J_{sc} values of the solar cells are also theoretically calculated from the integration of the convolution of IPCE and photon flux of AM 1.5 on the basis of eq. 1-5.

$$calculated\ J_{sc} = \int_{\lambda}\ IPCE(\lambda) * photon\ flux\ of\ AM\ 1.5\ (\lambda) d\lambda \quad \text{(eq. 1-5)}$$

1-3 Perovskite solar cells

1-3-1 History

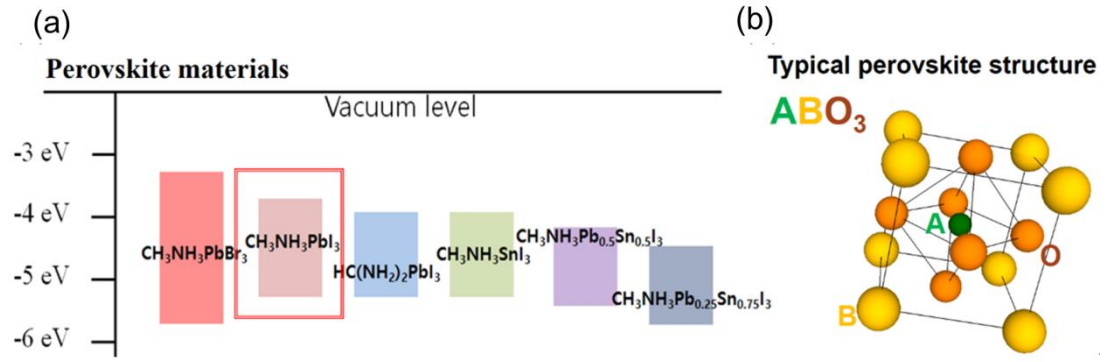

Figure 1-8. (a) Energy level of several kinds of perovskite materials. (b) Typical structure of perovskite materials, having the composition of ABO_3.

Perovskite solar cells (PVSCs), composed of perovskite compounds which are organic-inorganic hybrid materials, were invented in 2009.[10] Perovskite materials were at first used in dye-sensitized solar cells (DSSCs) recording the PCE of 3.8%. Among many kinds of perovskite materials, which have different band gap and energy levels (Figure 1-8a), $CH_3NH_3PbI_3$ and $CH_3NH_3PbBr_3$-based perovskite materials have been prevalently used in solar cells because of the adequate bandgap and large value of diffusion length and mobilities.[11] The typical structure of perovskite materials is based on 3-dimensional ABO_3 (Figure 1-8b).

The turning point to the rapid development of PVSCs stemmed from the advent of the solid-state PVSCs, which boosted the PCE up to 22.1% in 2016[4] as shown in Figure 1-1.

1-3-2 Structure and fabrication methods

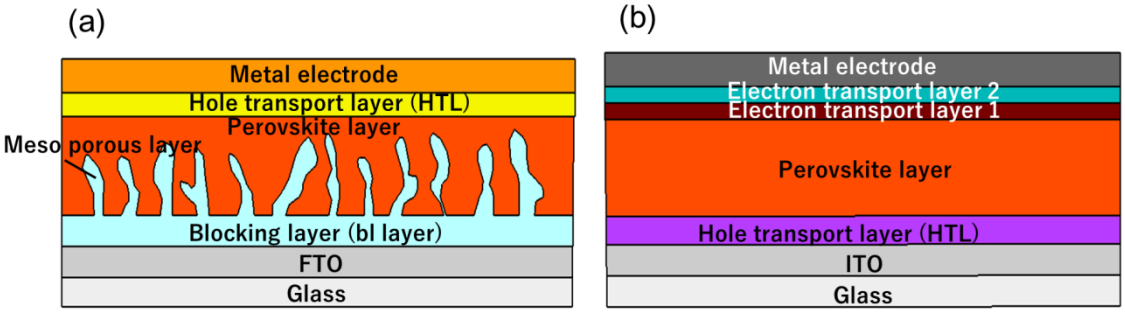

Figure 1-9. (a) The typical structure of meso-porous type PVSCs and (b) planar type PVSCs.

Solid-state PVSCs are mainly categorized into two groups; mesoporous PVSCs and planar PVSCs. The typical structure of mesoporous PVSCs are shown in Figure 1-9a. A titanium dioxide (TiO_2) is mainly used as a blocking layer, which flattens the rough surface of FTO, and a mesoporous layer, which is filled with a perovskite material. Since the formation of TiO_2 requires high temperature, a thermally resistive transparent electrode such as FTO is commonly used for mesoporous PVSCs. To flatten the rough surface of perovskite layer on mesoporous TiO_2 and transport holes to the metal electrode, a hole transport layers (HTLs) such as P3HT[11, 12] and 2,2′,7,7′-tetrakis(*N*, *N*-di-p-methoxyphenylamine)-9,9′spirobifluorene (spiro-OMETAD)[13] is coated on the peroskite layer, followed by evaporation of metal electrode. The PVSCs having high PCEs are based on the mesoporous structure with high photocurrents and photovoltages. The planar type PVSCs have been recently studied a lot by taking advantages of easy processability similar to OSCs. Unlike the mesoporous PVSCs, a HTL is prepared on the transparent electrode such as NiO and a composite of poly(3,4-ethylenedioxythiophene):poly(styrene sulfonate) (PEDOT:PSS), which are also used in OSCs. The overall structure of the planar PVSCs is shown in Figure 1-9b. In a similar manner to the mesoporous PVSCs, the electron transport layer (ETL) is coated on the perovskite layer for smoothening the perovskite layer surface and transportation of electrons to the metal electrode. PCBM is mainly used as the ETL. However, since the contact resistance between the metal electrode and PCBM is high because of the unmatched energy level, other ETLs such as LiF,[14] Ca,[15] bathocuproine (BCP)[16] are commonly used as the second ETL for the ohmic contact with the electrode. The PCEs of the planar PVSCs have been inferior to that of the mesoporous PVSCs despite their good processability.

1-3-3 Fabrication method of a perovskite layer

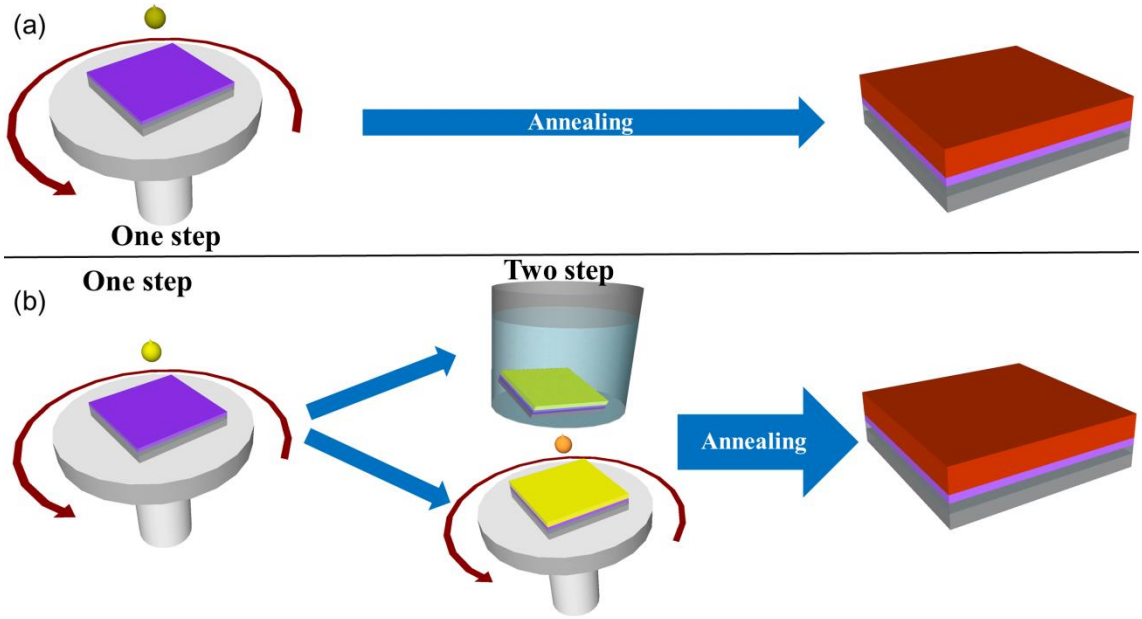

Figure 1-10. (a) One-step method and (b) two-step method for the fabrication of a perovskite layer.

Lead-based PVSCs are mainly composed of $CH_3NH_3PbI_3$ as a perovskite material. $CH_3NH_3PbI_3$ can be obtained from 1:1 molar ratio of CH_3NH_3I and PbI_2 in DMF or 1:3 molar ratio of CH_3NH_3I and $PbCl_2$ in DMF based on eq. 1-6.

$$CH_3NH_3I + PbI_2 \rightarrow CH_3NH_3PbI_3 \quad \text{(eq. 1-6-1)}$$

$$3CH_3NH_3I + PbCl_2 \rightarrow CH_3NH_3PbI_3 + 2CH_3NH_3Cl\,(g)\uparrow \quad \text{(eq. 1-6-2)}$$

In solid-state PVSCs, the precursor of CH_3NH_3I and PbI_2 has been utilized for the fabrication of perovskite layers. Later, Snaith group in 2013 found out that the use of $PbCl_2$ instead of PbI_2 leads to higher PCE value compared to the cells based on the use of PbI_2.

It was considered that the doping of Cl into the perovskite, namely $CH_3NH_3PbI_{3-x}Cl_x$, was the main factor to increase the carrier diffusion length of perovskite layer.[17] Diffusion lengths of both electron and hole are confirmed to be more than 1 μm for mixed halide perovskite ($CH_3NH_3PbI_{3-x}Cl_x$), while those of for triiodide ($CH_3NH_3PbI_3$) are one order smaller, which lead to high PCE values.[17]

However, it was found later that the superior diffusion length from the use of $PbCl_2$ is not caused by the doping of Cl because the chloride ions were not detected by the

thorough analysis by X-ray diffraction. Thus, the factor for the improvements have been considered to be the better morphology obtained by the use of $PbCl_2$ and the use of $CH_3NH_3PbI_{3-x}Cl_x$ has been no longer effective.[18]

For getting good morphology, several methods to fabricate perovskite layers have been developed, mainly categorized into two; one-step method and two-step method. Figure 1-10a shows the one-step method to fabricate perovskite layers. Here, the precursor of a perovskite ink is coated by spincoating on the carrier transport layer one time followed by annealing. As mentioned previously, the morphology of perovskite layers affects the performance largely and the coating precursor of PbI_2 and CH_3NH_3I by one step generally deteriorates the morphology of perovskite layers, forming holes and cracks. Substituting PbI_2 with $PbCl_2$ leads to better morphology in a one-step method, which is the reason that the precursor of $PbCl_2$ and CH_3NH_3I are mainly used in the one-step method.

In the two-step method, there is another step after the first spincoating (Figure 1-10b). Different from the one-step method, the precursor of PbI_2 is widely used in the first step by spincoating as a base substrate. Then, the precursor of CH_3NH_3I is coated on the surface of PbI_2 as the second step followed by annealing. In the second step, two different ways are prevalently used; dipping method and spincoating method as shown in Figure 1-10b. By the two step-method, good morphologies of perovskite layers can be obtained even if PbI_2 is used.

1-3-4 Drawbacks

(a) Instability

Despite high efficiencies of PVSCs, which are comparable to those of silicon PVs, several problems still exist, preventing the PVSCs from being commercialized in the market. Stability is one of the main issues, which is still not solved.

Lead based perovskites are easily hydrolyzed by the moisture. The mechanisms of decomposition of perovskites are based on eq. 1-7.[19]

$$CH_3NH_3PbI_3\ (s) \leftrightarrow PbI_2\ (s) + CH_3NH_3I\ (aq) \quad \text{(eq. 1-7-1)}$$

$$CH_3NH_3I\ (aq) \leftrightarrow CH_3NH_2\ (aq) + HI\ (aq) \quad \text{(eq. 1-7-2)}$$

$$4HI\ (aq) + O_2\ (g) \leftrightarrow 2I_2\ (s)\ 2H_2O\ (l) \quad \text{(eq. 1-7-3)}$$

$$2HI\ (aq) \leftrightarrow H_2\ (g) + I_2\ (s) \quad \text{(eq. 1-7-4)}$$

Equation 1-7-1 shows that the formation of perovskites is reversible, implying the instability of the perovskites. Moisture is not the only factor to degrade the perovskites.

Once the decomposition process occurs in the perovskites, three components of $CH_3NH_3PbI_3$, CH_3NH_2 and HI remain simultaneously on the basis of the eq. 1-7-1 and 1-7-2. Here, the HI is decomposed by two routes; one is the oxidation reaction by oxygen (eq.1-7-3) and another is the photochemical reaction by UV light (eq.1-7-4).[20]

Figure 1-11a shows the absorption spectra of a perovskite layer before and after the degradation by moisture. Considerable drop of absorption is observed for the degraded perovskites. The inset of Figure 1-11a also indicates the color changes of CH_3NH_3I in air under UV irradiation. From the results, it is known that the speed of reverse reaction of perovskites is accelerated by the light irradiation under the moisturized environment. In the XRD pattern in Figure 1-11b, PbI_2 peaks can be detected for the degraded perovskites, suggesting that the perovskite is decomposed to PbI_2 and CH_3NH_3I easily under the humid air. Thus the proper encapsulation process is requisite for the PVSCs.

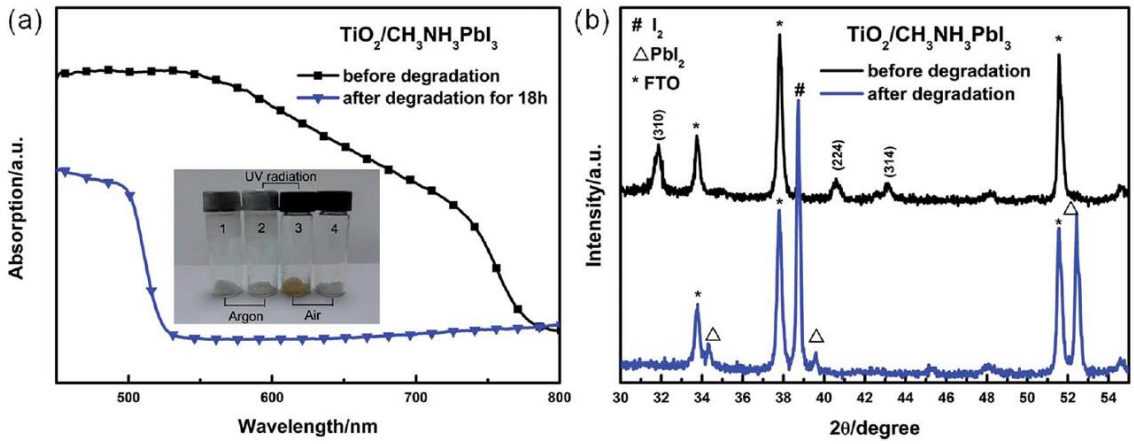

Figure 1-11. Degradation of $CH_3NH_3PbI_3$ in moisture and air atmosphere. (a) UV-vis absorption spectra of a $TiO_2/CH_3NH_3PbI_3$ film before and after degradation. The inset is a photograph of CH_3NH_3I exposed to different conditions: (1) CH_3NH_3I exposed to argon and without UV radiation. (2) CH_3NH_3I exposed to argon and with UV radiation. (3) CH_3NH_3I exposed to air and with UV radiation. (4) CH_3NH_3I exposed to air and without UV radiation. (b) XRD patterns of the $TiO_2/CH_3NH_3PbI_3$ film before and after degradation. Reprinted with permission from Ref. 20. Copyright 2014 Royal Society of Chemistry.

(b) Toxicity

High performance PVSCs are mainly composed of lead-based perovskites such as $CH_3NH_3PbI_3$ and $CH_3NH_3PbBr_3$. Pb is well known for its toxicity as exposure to Pb destructs the nervous and reproductive system in the human body. As mentioned previously, the perovskites are easily decomposed and Pb could be released into the environment.

Substitution with Pb to lead-free perovskites in PVSCs can be a solution to the toxicity caused by Pb. Peroskites based on tin (Sn)[21] and bismuth (Bi)[22] instead of Pb are the candidates for the lead-free PVSCs.

Unlike lead-based PVSCs, coating methods of lead-free perovskite precursors have not been studied. Films of lead-free perovskites have many defect sites such as pin-holes and cracks, which work as short path ways. Thus the PCE of lead-free PVSCs are still low. Recently, using excess tin iodide (SnI_2) with CsI as a precursor, the PCE of PVSCs based on Sn was improved.[23] Figure1-12a shows the energy diagram of perovskites based on Sn. Regardless of cations, which is $CH_3NH_3^+$ (MA), $CH(NH_2)_2^+$(FA) and Cs^+, Sn-based perovskites have low band gap, which can harvest near-IR light. However, the PCEs of $CsSnI_3$ PVSCs are still low, recording 4.81% (Fgure 1-11b) mainly because the EQE is low though they can harvest light to 1000 nm (Figure 1-11c). Thus, the PVSCs without toxic materials still lag behind the existing PVSCs based on lead materials.

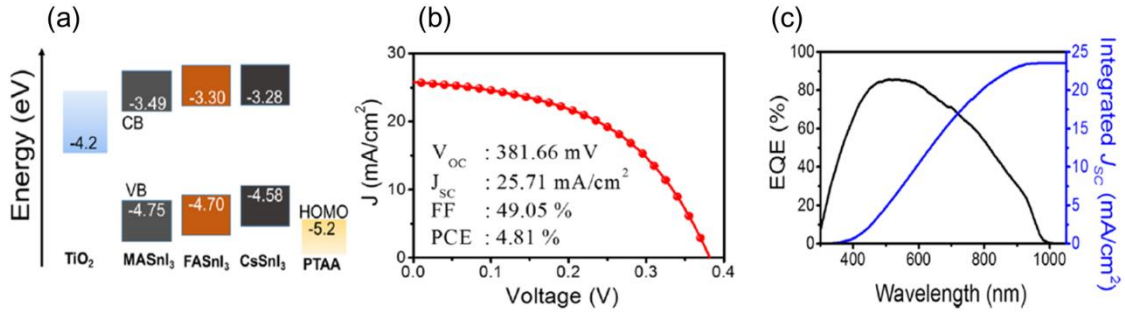

Figure 1-12. (a) Energy-level diagram of $CsSnI_3$. Reported values for $MASnI_3$, $FASnI_3$, TiO_2, and PTAA are also depicted. (b) *J*−*V* characteristic of the 0.4-CsI/SnI_2-based devices that showed the best performance. (b) Representative EQE spectrum and integrated J_{SC}. Reprinted with permission from Ref. 23. Copyright 2017 American Chemical Society.

(c) Hysteresis

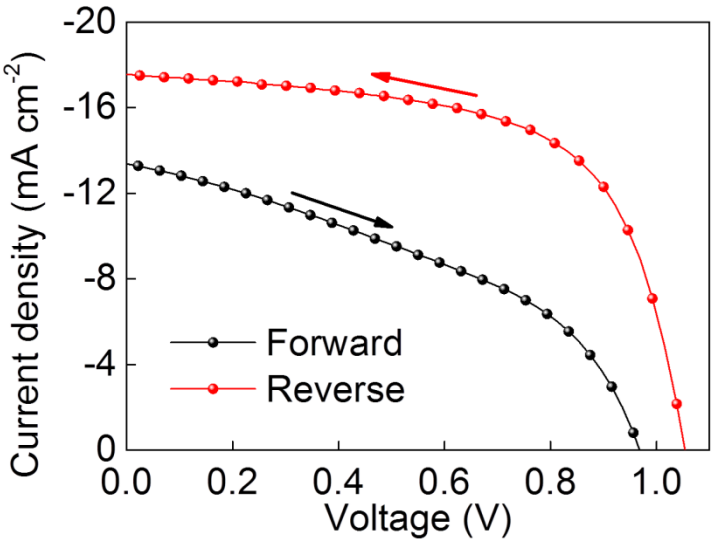

Figure 1-13. J-V characteristics of the PVSC measured from forward and reverse sweep.

Though the PCEs of PVSCs measured from *J-V* curves are high, the actual efficiencies of PVSCs are still under questions.[24, 25] The electrical properties of PVSCs are often affected by the scan rate and the direction of voltage sweep called hysteresis. Figure 1-13 shows the example of hysteresis of PVSCs depending on the sweeping direction. The PCE of the PVSC measured from reverse sweep is higher than that measured from forward sweep because of high J_{sc}, V_{oc} and FF (Figure 1-13). Generally, PCEs measured from reverse sweep tend to be higher for both mesoporous and planar PVSCs.[25] The hysteresis is believed to stem from capacitive charging and discharging effects of perovskite layers and rough interfaces of perovskite layers and HTLs or ETLs.[24] However, the exact reasons are still unclear. These days, hysteresis problem has been somewhat solved by preventing pores of perovskite layers and smoothening surfaces.[26, 27]

1-3-5 Semi-transparent PVSCs

Since the advent of organic solar cells (OSCs), the application of flexible and semi-transparent solar cells has become viable. Solution processed thin films can be easily coated on substrates, resulting in semi-transparent films.[28, 29]

However, the photocurrents of semi-transparent OSCs are lower because the thin and transparent back electrodes such as thin Ag, Au, and Ag nanowire are necessary.[30] The transparent electrodes inevitably lead to the loss of light, which passes through the

electrodes and thereby low photocurrents.

The similarity to OSCs regarding structures and processes enables to realize the fabrication of thin and semi-transparent perovskite films, which can be applied to semi-transparent PVSCs. In addition, the high absorptivity of light that perovskites have can lead to high photocurrents.

Nevertheless, the reports regarding semi-transparent PVSCs are still few because the perovskite films, of which the thickness is over 300 nm, are mostly non-transparent. Two approaches have been used for improving the transparency of perovskite films; the use of thinner perovskite films and the use of island types of perovskite films. The film thickness can be easily controlled by increasing the spin rate during spincoating of perovskite precursor or reducing the concentration of precursors. The latter can be controlled by different solvents and annealing temperature.[31] The evaporation rate of solvents can be changed, resulting in islands form of perovskite layer (Figure 1-14a). The islands form of perovskite layers has pores, through which light can pass through. This enhances the transmittance of the semi-transparent PVSCs (Figure 1-14b). However, the improvement of transmittance weakens the light absorption in the visible range, and decreases the photocurrents. Because of the inevitable decrease in light absorption and photocurrents, semi-transparent PVSCs with good transparency still have low value of PCEs.

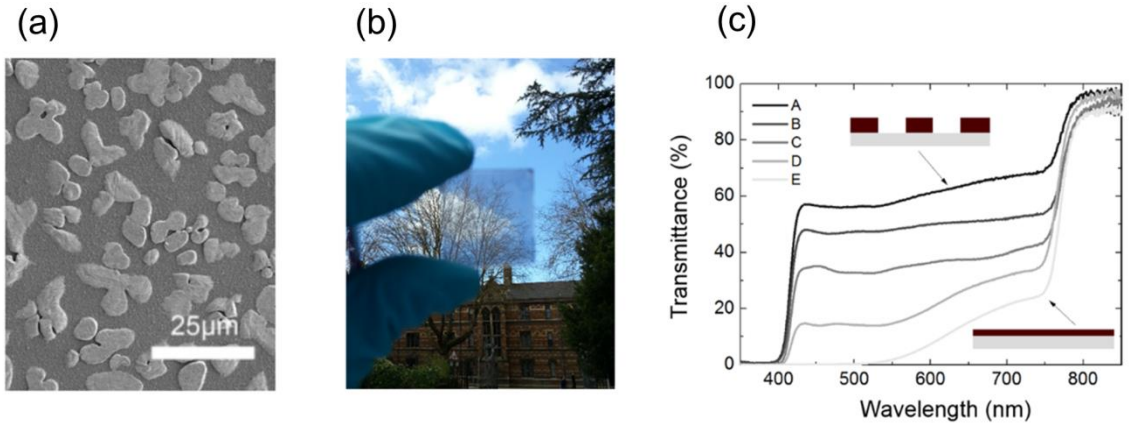

Figure 1-14. (a) Scanning electron micrograph of the top surface of a film of perovskite islands on a TiO_2-coated FTO substrate. (b) Photograph through a typical semitransparent perovskite film formed on glass. (c) Transmittance spectra of active layers of the semi-transparent devices. Reprinted with permission from Ref. 31. Copyright 2014 American Chemical Society.

1-4 Plasmon enhancement effects

1-4-1 Localized surface plasmon resonance (LSPR)

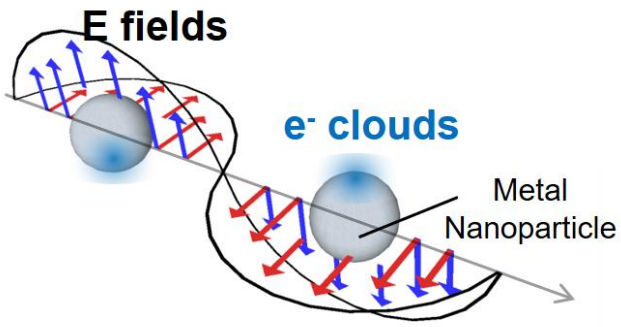

Figure 1-15. Resonance between the free electron oscillation of MNPs and the electric field oscillation of light.

Unlike bulk metals, in metal nanoparticles (MNPs), the free electrons oscillating around MNPs can be resonated with the oscillating electric field of incident light, which is known as localized surface plasmon resonance (LSPR) (Figure 1-15).[32, 33]

By LSPR, a photon is transformed to the plasmon on a MNP, which can be diversely applied to many kinds of materials and devices, such as converting light energy to electrical energy or enhancing photocurrents in solar cells.[34, 35]

1-4-2 Application of LSPR to solar cells

It has been known that MNPs can enhance photocurrents of photovoltaic systems.[34, 35] The enhancement is considered to stem from the optical near-field[36, 37] antenna and far-field scattering effects of MNPs, which excite electrons of active layers in photovoltaic systems.[38] To harvest light by MNPs, the MNPs have to be combined with the active layers in photovoltaic systems.[39]

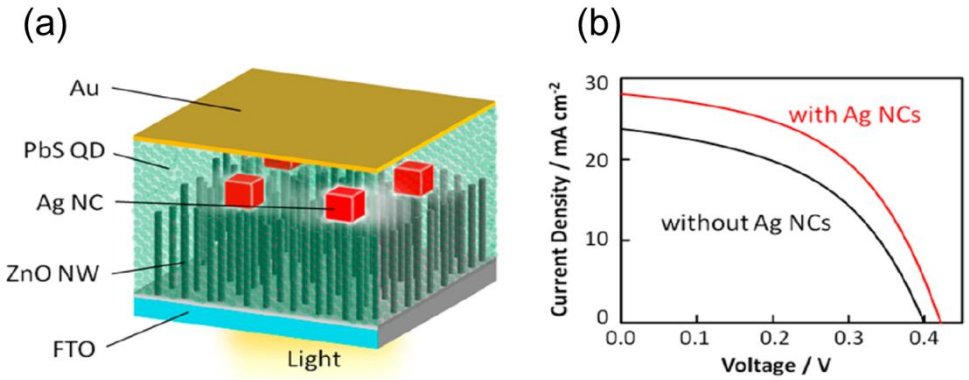

Figure 1-16. (a) Introduction of silver nanocubes (AgNCs) into PbS quantum dot (QD) solar cells. (b) *J-V* characteristics of QD solar cells with and without AgNCs. Reprinted with permission from Ref. 39. Copyright 2015 American Chemical Society.

Figure 1-16a shows the direct introduction of silver nanocubes (AgNCs) to a PbS QD active layer. The photocurrents are enhanced because the near-field antenna effect of AgNCs helps to capture photons near PbS QDs (Figure 1-16b). Also, the strong far-field scattering occurs in the weak absorption region of PbS QDs, which is at long wavelengths. This is because the high refractive index of PbS QD leads to the large red-shift of plasmonic peaks.[40]

The direct use of MNPs inside active layers allows utilization of the near-field and far-field scattering simultaneously. However, the MNPs themselves can work as electron-hole recombination sites, which can degrade the performances.

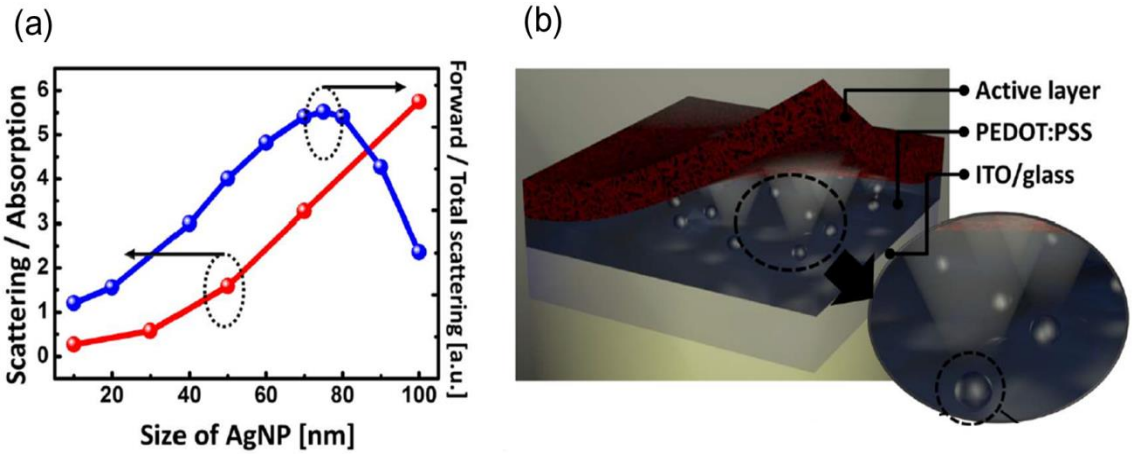

Figure 1-17. (a) Ratio of the forward scattering to the total scattering of a spherical AgNP in PEDOT:PSS. (b) Schematic of a plasmonic OSC. The device structure is glass/ITO/PEDOT:PSS with AgNPs/active layer. Reprinted with permission from Ref. 38. Copyright 2013 Nature.

Combining MNPs in other layers in the vicinity of active layers such as HTL or ETL is an easy approach to this issue since only holes are injected into HTL and electrons are injected into ETL. Figure 1-17b shows the example of silver nanoparticles (AgNP) inserted in PEDOT:PSS, commonly used as a HTL in OSCs.[38] When the value of scattering of MNPs becomes larger than that of absorption, scattering effects become dominant, resulting in an increase of scattering light into the active layers, and thereby enhanced photocurrents. The scattering tends to increase when the size of MNPs is large (Figure 1-17a). Despite the advantage of the use of MNPs in HTL or ETL, near-field effects diminish as the effective length of near field is short (~10 nm). Further, a large size of MNPs could cause short circuiting between the active layer and an electrode because the carrier transport layers are normally thin (~30 nm).

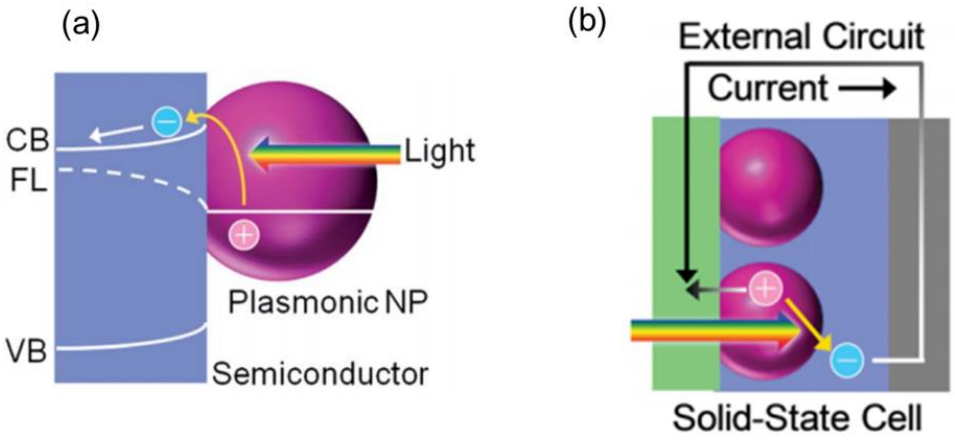

Figure 1-18. (a) The plasmon-induced charge separation (PICS). (b) A solid-state cell on the basis of PICS. Reprinted with permission from Ref. 42. Copyright 2017 Royal Society of Chemistry.

MNPs also have properties to transfer electrons to semiconductors known as plasmon-induced charge separation (PICS).[41, 42] At the interface of MNP and a semiconductor, the Schottky barrier is formed. When the plasmonic MNP absorbs incident light which has higher energy than Schottky barrier, uphill electron transfer occurs from MNP to conduction band (CB) of semiconductor (Figure 1-18a). Solid-state photovoltaic cells can also be developed by using PICS in which MNPs themselves function as active materials to generate electricity (Figure 1-18b).[42]

By exploiting PICS, increasing electronic conductivity of the cells is also possible. Conductivity under light irradiation of a perovskite solar cells with TiO_x layer is increased by introduction of Au NPs into the TiO_x layer.[43] In the same way, when

plasmonic NMPs are embedded in an ETL of a photovoltaic cell such as a PVSC, the electron might be injected from the MNPs to the ETL on the basis of PICS (Figure 1-18a), resulting in an increase of electronic conductivity of the ETL, namely a decrease in the serial resistance.[43] This could lead eventually to improvement in photocurrents and PCE. Hole injection from plasmonic NMPs to a HTL might also be possible.[42] Likewise, carrier injection into an active layer such as a perovskite material might also contribute to improvement of photovoltaic performances.

1-5 Purpose

Despite great advantages of PVSCs when it comes to the cost effectiveness and the PCE comparable to that of silicon-based solar cells, several drawbacks such as instability in air and hysteresis problems still exist. In addition, it is necessary to improve efficiency and transparency of semi-transparent PVSCs. Here, improving the performance of PVSCs including semi-transparent cells is mainly dealt with, and three approaches have been proposed in this research.

First, the development of ultrasmooth perovskite films was focused. It is considered that the perovskite films are sensitively affected by fabrication conditions. Developing a novel method to produce the ultrasmooth perovskite films, high performances of PVSCs are expected, which can be applied to semi-transparent PVSCs. Through optical and electrical analyses, the factors that improve the smoothness and transparency were unveiled.

Second, plasmonic MNPs were introduced into PVSCs. Unlike OSCs, the use of MNPs into PVSCs has not widely conducted mainly because the plasmonic enhancement region of typical MNPs is positioned in the strong absorption region of perovskite layers, in which the external quantum efficiency (EQE) reaches nearly 100%. Thus, the further photocurrent improvements by MNPs are not obvious. Thus, the exploit of LSPR in the low absorption region of perovskite layer is important to harvest light in PVSCs. In this regard, shifting of LSPR peaks by structural change is necessary for the application of MNPs to PVSCs.

Lastly, it is aimed that the performance of semi-transparent PVSCs is improved by introduction of MNPs. Improving transparency and efficiency simultaneously in semi-transparent solar cells have been considered to be difficult. It is expected that the use of MNPs in semi-transparent PVSCs enhances the photocurrents while keeping the adequate thickness of perovskite layer, resulting in good transparency.

1-6 References

1. R. S. Ohl, Google Patents: 1948.
2. L. Qiao, D. Wang, L. Zuo, Y. Ye, J. Qian, H. Chen and S. He, *Appl. Energy*, 2011, **88**, 848-852.
3. S.-S. Kim, S.-I. Na, J. Jo, D.-Y. Kim and Y.-C. Nah, *Appl. Phys. Lett.*, 2008, **93**, 305.
4. http://www.rel.gov/pv/assets/images/efficiency-chart.png.
5. H. Spanggaard and F. C. Krebs, *Sol. Energ. Mat. Sol. Cells*, 2004, **83**, 125-146.
6. C. Lungenschmied, G. Dennler, H. Neugebauer, S. N. Sariciftci, M. Glatthaar, T. Meyer and A. Meyer, *Sol. Energ. Mat. Sol. Cells*, 2007, **91**, 379-384.
7. Y. Terao, H. Sasabe and C. Adachi, *Appl. Phys. Lett.*, 2007, **90**, 103515.
8. A. J. McEvoy, L. Castaner and T. Markvart, *Solar cells: materials, manufacture and operation*, Academic Press, 2012.
9. C. Riordan and R. Hulstron, *IEEE*, 1990, 1085-1088.
10. A. Kojima, K. Teshima, Y. Shirai and T. Miyasaka, *J. Am. Chem. Soc*., 2009, **131**, 6050-6051.
11. F. Di Giacomo, S. Razza, F. Matteocci, A. D'Epifanio, S. Licoccia, T. M. Brown and A. Di Carlo, *J. Power Sources*, 2014, **251**, 152-156.
12. J. H. Heo, S. H. Im, J. H. Noh, T. N. Mandal, C.-S. Lim, J. A. Chang, Y. H. Lee, H.-j. Kim, A. Sarkar and M. K. Nazeeruddin, *Nat. Photon.*, 2013, **7**, 486-491.
13. M. M. Lee, J. Teuscher, T. Miyasaka, T. N. Murakami and H. J. Snaith, *Science*, 2012, **338**, 643-647.
14. J. Seo, S. Park, Y. C. Kim, N. J. Jeon, J. H. Noh, S. C. Yoon and S. I. Seok, *Energy Environ. Sci*., 2014, **7**, 2642-2646.
15. C.-H. Chiang and C.-G. Wu, *Nat. Photon.*, 2016, **10**, 196-200.
16. J. Y. Jeng, K. C. Chen, T. Y. Chiang, P. Y. Lin, T. D. Tsai, Y. C. Chang, T. F. Guo, P. Chen, T. C. Wen and Y. J. Hsu, *Adv. Mater.*, 2014, **26**, 4107-4113.
17. S. D. Stranks, G. E. Eperon, G. Grancini, C. Menelaou, M. J. P. Alcocer, T. Leijtens, L. M. Herz, A. Petrozza and H. J. Snaith, *Science*, 2013, **342**, 341-344.
18. C. Quarti, E. Mosconi, J. M. Ball, V. D'Innocenzo, C. Tao, S. Pathak, H. J. Snaith, A. Petrozza and F. De Angelis, *Energy Environ. Sci*., 2016, **9**, 155-163.
19. G. Niu, X. Guo and L. Wang, *J. Mater. Chem. A*, 2015, **3**, 8970-8980.
20. G. Niu, W. Li, F. Meng, L. Wang, H. Dong and Y. Qiu, *J. Mater. Chem. A*, 2014, **2**, 705-710.
21. K. P. Marshall, R. I. Walton and R. A. Hatton, *J. Mater. Chem. A*, 2015, **3**, 11631-11640.
22. A. H. Slavney, T. Hu, A. M. Lindenberg and H. I. Karunadasa, *J. Am. Chem. Soc*., 2016, **138**, 2138-2141.
23. T.-B. Song, T. Yokoyama, S. Aramaki and M. G. Kanatzidis, *ACS Energy Lett.*, 2017, **2**, 897-903.
24. B. Chen, M. Yang, S. Priya and K. Zhu, *J. Phys. Chem. Lett.*, 2016, **7**, 905-917.

25. H. J. Snaith, A. Abate, J. M. Ball, G. E. Eperon, T. Leijtens, N. K. Noel, S. D. Stranks, J. T.-W. Wang, K. Wojciechowski and W. Zhang, *J. Phys. Chem. Lett.*, 2014, **5**, 1511-1515.
26. N. Tripathi, M. Yanagida, Y. Shirai, T. Masuda, L. Han and K. Miyano, *J. Mater. Chem. A*, 2015, **3**, 12081-12088.
27. D. Bryant, S. Wheeler, B. C. O'Regan, T. Watson, P. R. F. Barnes, D. Worsley and J. Durrant, *J. Phys. Chem. Lett.*, 2015, **6**, 3190-3194.
28. S. K. Hau, H.-L. Yip, J. Zou and A. K. Y. Jen, *Org. Electron.*, 2009, **10**, 1401-1407.
29. R. F. Bailey-Salzman, B. P. Rand and S. R. Forrest, *Appl. Phys. Lett.*, 2006, **88**, 233502.
30. M. G. Kang, T. Xu, H. J. Park, X. Luo and L. J. Guo, *Adv. Mater.*, 2010, **22**, 4378-4383.
31. G. E. Eperon, V. M. Burlakov, A. Goriely and H. J. Snaith, *ACS Nano*, 2013, **8**, 591-598.
32. S. Eustis and M. A. El-Sayed, *Chem. Soc. Rev.*, 2006, **35**, 209-217.
33. K. L. Kelly, E. Coronado, L. L. Zhao and G. C. Schatz, *J. Phys. Chem. B*, 2003, **107**, 668-677.
34. S. Linic, P. Christopher and D. B. Ingram, *Nat. Mater.*, 2011, **10**, 911-921.
35. H. A. Atwater and A. Polman, *Nat. Mater.*, 2010, **9**, 205-213.
36. T. Kawawaki, Y. Takahashi and T. Tatsuma, *J. Phys. Chem. C*, 2013, **117**, 5901-5907.
37. T. Kawawaki and T. Tatsuma, *Phys. Chem. Chem. Phys.*, 2013, **15**, 20247-20251.
38. S.-W. Baek, J. Noh, C.-H. Lee, B. Kim, M.-K. Seo and J.-Y. Lee, *Sci. Rep.*, 2013, **3**.
39. T. Kawawaki, H. Wang, T. Kubo, K. Saito, J. Nakazaki, H. Segawa and T. Tatsuma, *ACS Nano*, 2015, **9**, 4165-4172.
40. A. Moreau, C. Ciraci, J. J. Mock, R. T. Hill, Q. Wang, B. J. Wiley, A. Chilkoti and D. R. Smith, *Nature*, 2012, **492**, 86-89.
41. Y. Tian and T. Tatsuma, *J. Am. Chem. Soc.*, 2005, **127**, 7632-7637.
42. T. Tatsuma, H. Nishi and T. Ishida, *Chem. Sci.*, 2017, **8**, 3325-3337.
43. Z. Yuan, Z. Wu, S. Bai, Z. Xia, W. Xu, T. Song, H. Wu, L. Xu, J. Si and Y. Jin, *Adv. Energy Mater.*, 2015, **5**, 1500038.

Chapter 2

Ultrasmooth and semi-transparent perovskite layers

2-1 Introduction

As mentioned above, the optical and electrical properties of perovskite layers are largely affected by the fabrication conditions. Moisture in air is considered as a main cause for the defects of final perovskite layers. By using humidity-controlled environment such as clean rooms and nitrogen glove boxes, the exposure to moisture during fabrication of perovskite layers is avoidable. However, maintenance of clean rooms, in which the level of humidity is kept throughout whole season, is not cost-effective. Also, the movements in nitrogen glove boxes are limited because of confined spaces. Thus experimenters may not properly conduct the experiment in right procedures, leading to experimental errors.

Here, the fabrication conditions of perovskite layers in ambient air will be dealt with. As the whole procedures do not require the clean rooms and glove boxes, they are considered to be cost-effective.

First, the different dispensing methods of perovskite precursors on ITO/ poly(3,4-ethylenedioxythiophene):poly(styrene sulfonate) (PEDOT:PSS) substrate were introduced; dispensing precursors before the substrate spin (static dispense) and during the substrate spin (dynamic dispense). Then, the optical and electrical properties of perovskite solar cells (PVSCs) processed under the different conditions were measured and compared.

Though the above-mentioned methods are cost-effective, realization of high performance power conversion efficiencies (PCEs) is not easy. In this regard, another procedure to reduce the moisture exposure during fabrication was also developed. By drying and annealing the perovskite precursor under vacuum, the exposure to moisture during the fabrication of perovskite layer is minimized. The final perovskite films processed by this method have unique properties that are not observed in pre-existing perovskite layers fabricated by conventional methods.

Finally, semi-transparent PVSCs were prepared and also analyzed optically and electrically.

2-2 Experimental

2-2-1 preparation of PVSCs by dynamic or static dispense

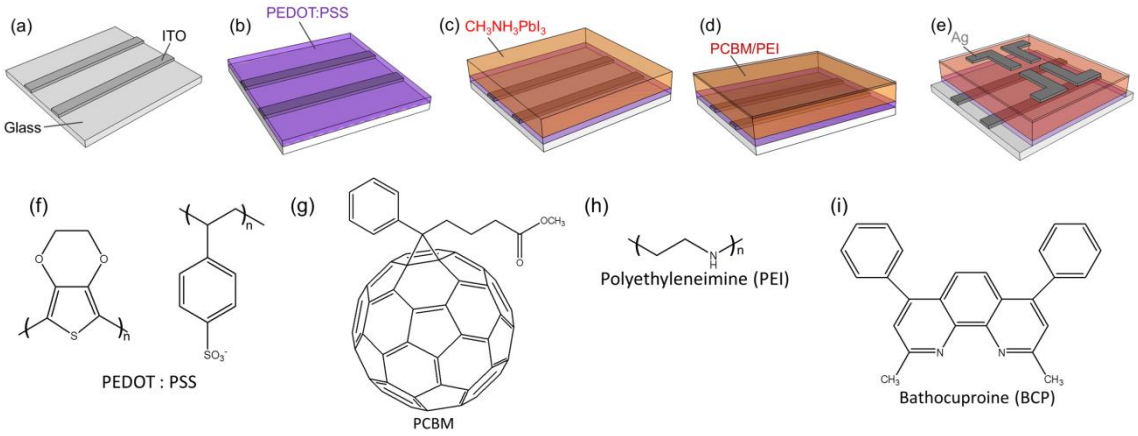

Figure 2-1. (a) ITO on glass (23 mm x 23 mm), which is etched into two lines (2 mm x 23mm). (b) PEDOT:PSS coated on the whole surface of etched ITO. (c) $CH_3NH_3PbI_3$ coated on PEDOT:PSS layer by one of the different fabrication methods; dynamic dispense or static dispense (Figure 2-2). (d) PCBM layer coated on $CH_3NH_3PbI_3$. (e) Evaporation of silver through a patterned mask; two edge sides are removed by wetted cotton buds for the measurements. The effective cell area (2 x 2 mm^2) is the overlap between the silver electrode and ITO. One substrate has 4 cells as shown above. The chemical structures of (f) PEDOT:PSS, (g) PCBM, (h) PEI and (i) BCP.

Etched ITO substrates, which have two lines pattern shown in Figure 2-1a, were pre-cleaned by pure water, acetone and iso-propanol sequentially using sonication. The pre-cleaned ITO was treated by oxygen plasma for 40 s with the setting of 30 A and 30 cc. During the oxygen plasma treatment, PEDOT:PSS (AI 4083 Heraeus) was filtered by polyvinylidene difluoride (PVDF) syringe filter (0.45 μm). (*AI 4083 Heraeus has low conductivity compared to other models of PEDOT:PSS. This prevents potential short pathway of the final solar cells because PEDOT:PSS may work as electrodes if the conductivity is high. PVDF syringe filter should be used for the PEDOT:PSS filter as the hydrophilic PEDOT:PSS is not well filtered by polytetrafluoroethylene (PTFE) syringe filter, which is well used in hydrophobic solution.*)

Perovskite precursor (3:1 ratio of CH_3NH_3I and $PbCl_2$ in *N*,*N*-dimethylformamide (DMF)), which was stirred for at least 3h on a hot plate at 60 °C, was filtered by PTFE syringe filter (0.45 μm) and promptly stirred again on the hot plate at 60 °C. (*The concentration of precursor commonly used here is 36 wt%, which leads to 240-300 nm-thick-provskite layers. Concentration may vary by fabricating conditions*)

The filtered PEDOT:PSS (100 µL) was spin-coated at 5000 rpm for 35 s on the oxygen treated ITO and annealed at 150 °C for 10 min followed by annealing at 90 °C for 5 min (Figure 2-1b). The pre-heated PEDOT:PSS substrate at 100 °C was promptly transferred to a spin-coater. The pre-heated perovskite precursor at 60 °C was spin-coated on the PEDOT:PSS substrates by one of the two methods; dynamic dispense or static dispense.

In dynamic dispense, the perovskite precursor (30 µL) was dispensed on the PEDOT:PSS film while the film was spinning. In static dispense, the perovskite precursor (60 µL) was dispensed on the PEDOT:PSS film before the substrate was spinning. In both cases, the spinning time was 35 s. Then, the films were annealed at 100 °C for 1 h in ambient air for the formation of perovskite layers (Figure 2-1c). 2 wt% of [6,6]-phenyl-C_{61}-butyric acid methyl ester (PCBM) in chlorobenzene (CB), stirred overnight at 60 °C, and followed by being filtered by PTFE syringe filter (0.45 µl) was spin-coated on the perovskite layer for 35 s at 1000 rpm (Figure 2-1d).

Polyethyleneimine-ethoxylated (PEI) (20 µL) was further diluted with methanol (MeOH) to 0.2 wt% and coated on PCBM at 4000 rpm by dynamic dispense. Then, a silver back electrode was deposited by evaporation at the rate of 0.1 nm s^{-1} with the evaporation mask that has four sections, which realize four photovoltaic cells on one substrate (Figure 2-1e). Two edge sides of the substrate were removed by cotton bud that was wet by pure water for the contact to the measurement tool.

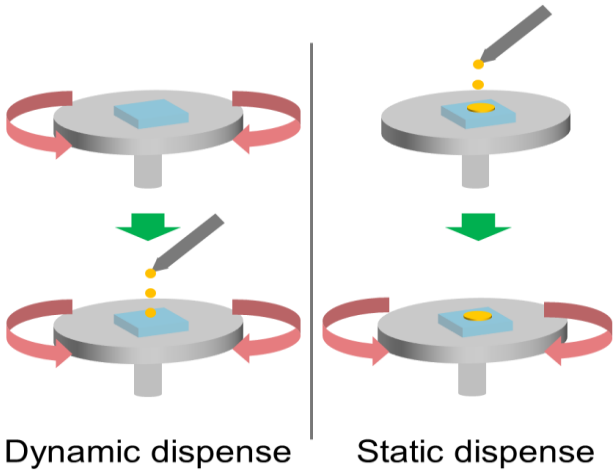

Figure 2-2. Spincoating procedure of the perovskite precursor on ITO/PEDOT:PSS substrates using (a) dynamic dispense and (b) static dispense for the fabrication of perovskite layers.

2-2-2 Preparation of PVSCs by short spinning and vacuum drying (SSVD) method

The procedure is the same as the preparation of perovskite films by dynamic or static dispense until the preparation of ITO/PEDOT:PSS. In SSVD method, the perovskite precursor that was preheated at 60 °C was dispensed (60 μL) by static dispense on the PEDOT:PSS surface. Then, the substrates were spin-coated at 4000 rpm for 5 s. The wetted substrates were promptly transferred to a vacuum oven and dried under low pressure (~0.05 kPa) for 15 min. Then, the substrates were annealed at 50-100 °C under 0.05 kPa; 60 °C is enough for the transformation of perovskites for SSVD. The substrates after annealing were taken out to ambient air and were coated with PCBM (1.6 wt% in CB) at 1500 rpm for 45 s. Bathocuproine (BCP, 0.05 wt% in MeOH, 20 μL) was coated on PCBM at 4000 rpm for 45 s, followed by evaporation of Ag (100 nm) for non-transparent PVSCs. For semi-transparent PVSCs, 10 nm of Ag and 20 nm of MoO_3 were sequentially deposited to obtain a transparent electrode.

2-2-3 Characterization

Optical properties of the samples were measured by using a spectrophotometer (Jasco V-670) equipped with an integrating sphere. We obtained photocurrent action spectra using Hamamatsu Photonics OSG (photon flux = 5×10^{15} photons cm^{-2} s^{-1}). The current density-voltage characteristics were measured by scanning the voltage at 100 mV s^{-1} with a source meter (Keithley 2612B) under AM1.5G irradiation (100 mW cm^{-2}) from a solar simulator (Bunkoukeiki, BSS-150T).

2-3 PVSCs with ETL on ITO

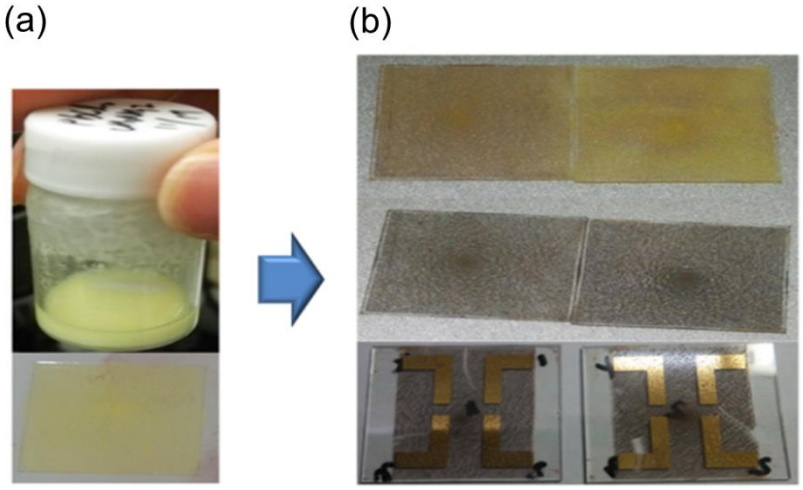

Figure 2-3. (a) Perovskite precursor of CH_3NH_3I and $PbCl_2$ (molar ratio of 1:1) in DMF. (b) Perovskite precursors that are spin-coated on ITO/PEDOT:PSS (the yellow substrates, top) and the substrates after annealing at 100 ° C (middle). The completed PVSCs (bottom).

As mentioned in Chapter 1, PVSCs are mainly categorized into two structures; mesoporous PVSCs and planar PVSCs. In the case of planar PVSCs, the PEDOT:PSS is commonly used as hole transport layer (HTL) on ITO (Figure 1-8b),[1-4] which is also called as inverted-type PVSCs because the first solid-type PVSCs have electron transport layers (ETLs) such as TiO_2 and ZnO on the transparent electrode.[5, 6]

It is expected that the planar type PVSCs are not necessarily based on HTLs on ITO as ETLs are widely used on ITO in organic solar cells (OSCs), which are structurally similar to planar PVSCs. Since OSCs in which ETLs are used on ITO have better air stability, here the planar PVSCs in which ETLs are used on ITO were fabricated. For the preparation of perovskite precursors using CH_3NH_3I and $PbCl_2$, the ratio of these two is very important. From eq. 1-6-2, the ideal molar ratio of CH_3NH_3I to $PbCl_2$ is 3:1. When this ratio deviates, the CH_3NH_3I and $PbCl_2$ are not mixed and the precursors the precipitates (Figure 2-3a). The unmixed precursors lead to many defect sites and pinholes of perovskite layer (Figure 2-3b), leading to low performances due to shorting.

Figure 2-4a shows the energy diagram of the present planar PVSCs, in which PEI and TiO_2 are used as ETLs on ITO. With 3:1 molar ratio of CH_3NH_3I and $PbCl_2$, the precursors are well mixed (Figure 2-4b) and the uniform coating of the precursors on the substrates was possible.

However, *J-V* characteristic shows poor performances compared to inverted planar

PVSCs in which HTL is used on ITO reported elsewhere (Figure 2-4c).[7-10] It is considered that planar TiO_2 cannot work efficiently as ETLs unlike meso-porous TiO_2 in perovskite layers. Therefore, PVSCs in which HTLs are coated on ITO electrodes will be examined in the following sections.

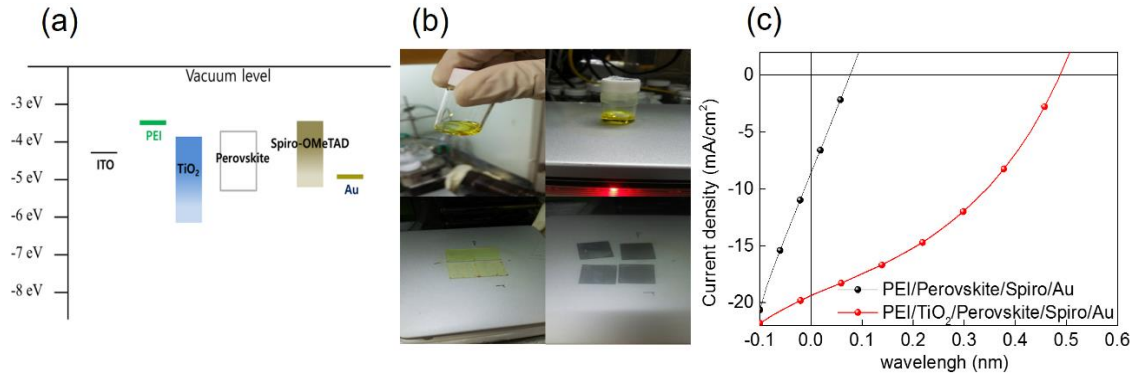

Figure 2-4. (a) Energy diagram of planar PVSCs in which ETLs are coated on ITO. (b) Perovskite precursors of CH_3NH_3I and $PbCl_2$ (molar ratio of 3:1) in DMF and the substrates after the coating of perovskite precursors (left bottom) and the substrates after the annealing (right bottom). (c) *J-V* characteristics of planar PVSCs.

2-4 PVSCs with HTL on ITO prepared by static and dynamic dispense

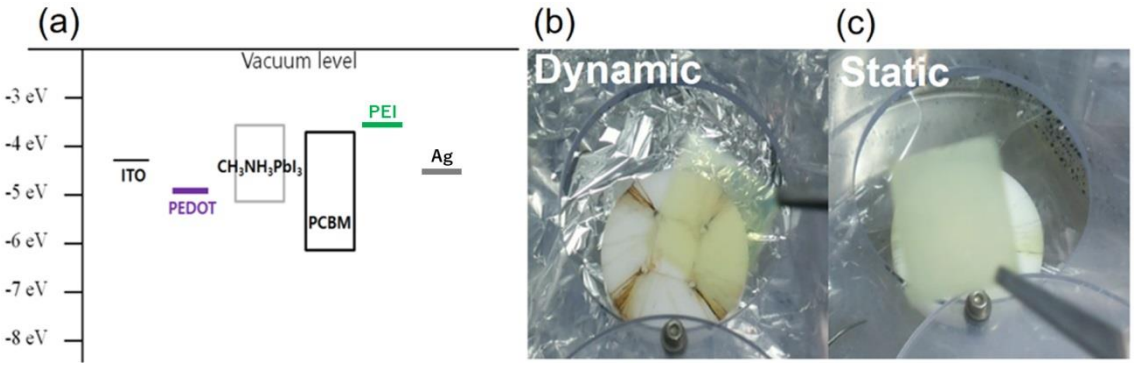

Figure 2-5. (a) Energy diagram of PVSCs. (b,c) Perovskite layers prepared on ITO/PEDOT:PSS substrates by (b) dynamic dispense and (c) static dispense.

As explained in experimental section and shown in Figure 2-2, the two different spincoating methods (dynamic and static dispense) were used for the planar PVSCs. Hereafter, "planar PVSC" indicates a planar PVSC in which HTL is coated on ITO, unless otherwise noted. Perovskites are extremely sensitive to the fabrication process. Thus, the optical and electrical properties of perovskites are also different. In PVSCs,

PEDOT:PSS and PCBM with PEI were used as an HTL and ETL respectively, which are prevalently used in OSCs.[11-15]

The energy diagram of the planar PVSCs developed herein is depicted in Figure 2-5a. As shown in Figure 2-5b, the substrates right after the spincoating by dynamic dispense are semi-transparent while the substrates are opaque after static dispense (Figure 2-5c). The opaque films obtained by static dispense stem from the rough morphology of perovskite precursors that cause strong scattering. Because of the different morphology of substrates that are coated with perovskite precursors by dynamic and static dispense, the backward scattering of the perovskite layers after annealing at 100 °C shows slightly different values; that for the dynamic dispense is lower than that for the static dispense at any spin-speed (Figure 2-6a).

In Figure 2-6b,c, the *J-V* characteristics of the PVSCs prepared at different spin-speed are shown. The overall parameters of the cell performances with each different condition are depicted in Figure 2-7.

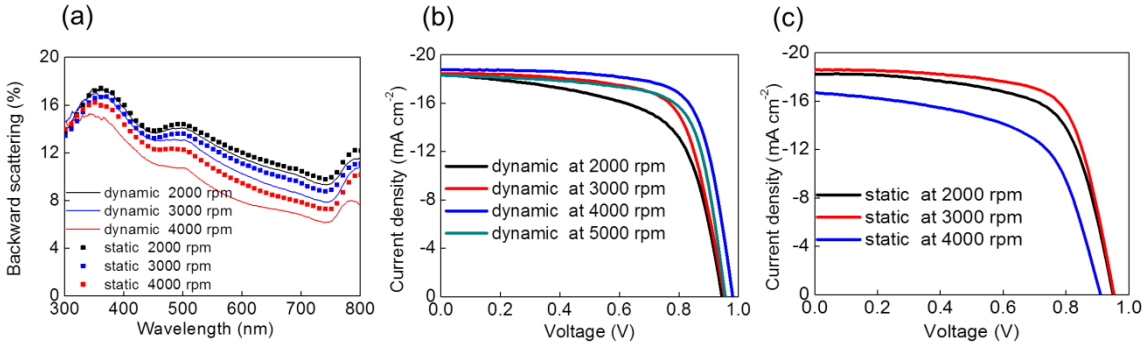

Figure 2-6. (a) Backward scattering spectra of the perovskite layers prepared at different spin-speed. *J-V* characteristics of PVSCs prepared at different spin-speed during spincoating of perovskite precursors processed by (b) dynamic dispense and (c) static dispense.

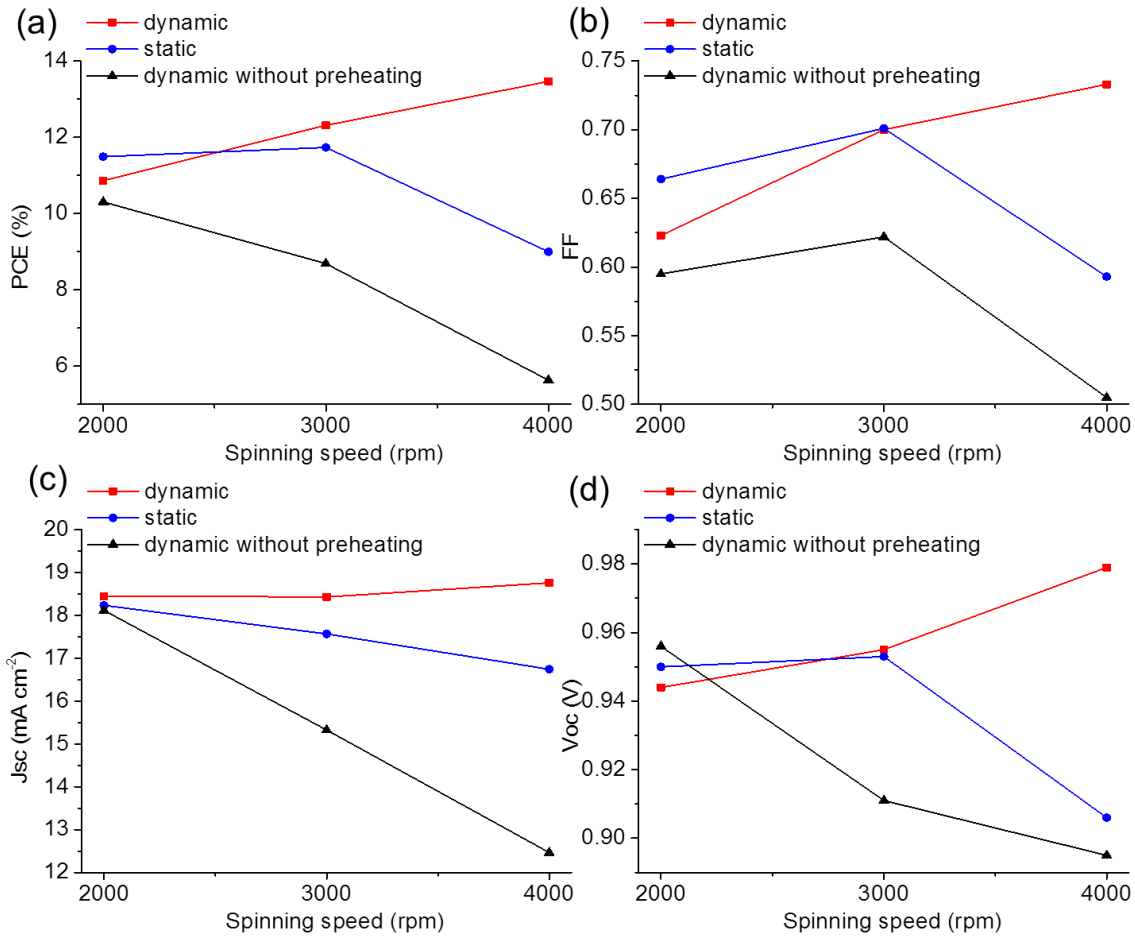

Figure 2-7. (a) PCE, (b) FF, (c) J_{sc} and (d) V_{oc} of the PVSCs prepared under different conditions.

It is noted that the perovskite precursors were heated at 90 °C when coating the precursors on the PEDOT:PSS substrates. Except 2000 rpm, PVSCs processed by dynamic dispense have higher PCE (red) than cells processed by static dispense (blue) due to the higher FF, J_{sc} and V_{oc}. The black lines in Figure 2-7 shows the performances of PVSCs prepared without pre-heating of the perovskite precursors during spin-coating. The PCEs are lower because the all parameters have small values even though they were processed by dynamic dispense.

From the results, it is figured out that the dynamic dispense with preheating perovskite precursor leads to superior performances of PVSCs compared to other conditions.

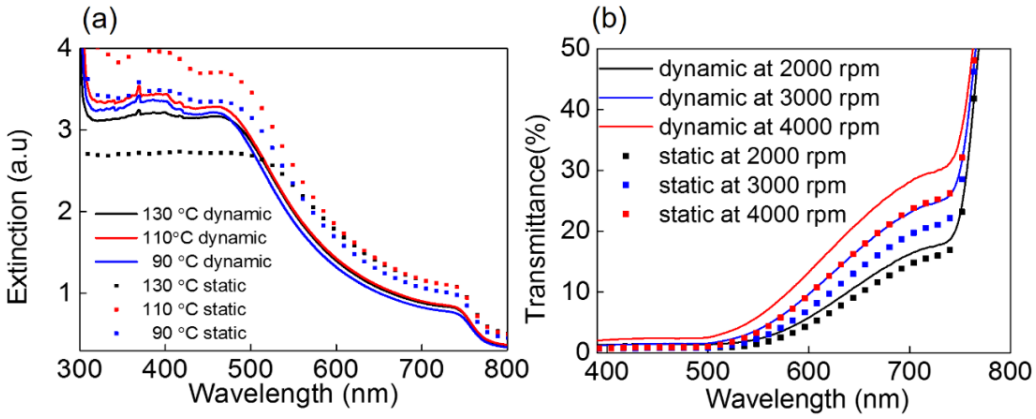

Figure 2-8. (a) Extinction spectra of the perovskite layers prepared at different pre-heating temperature of perovskite precursors and (b) transmittance spectra of the perovskite layers prepared at different spin-speed during spincoating of perovskite precursors by dynamic and static dispense.

As described above, pre-heating perovskite precursors is important for better performances. During the fabrication, keeping the same temperature of precursor is not easy because the precursor might be cooled down during the transfer of the substrates to a spin-coater and the dispensing time. This might cause reproducibility problems.

Figure 2-8a shows the extinction spectra of the perovskite layers on ITO/PEDOT:PSS substrates prepared at different pre-heating temperature of perovskite precursors by dynamic and static dispense. The shapes of extinction of the substrates prepared by dynamic dispense are rarely affected by the temperature between 90 °C and 130 °C while the value of extinction of the substrates by static dispense under 500 nm are different by the different temperature. This implies that perovskite layers processed by dynamic dispense can take advantage of reproducibility.

The reason for the superior optical and electrical properties of the perovskite layers processed by dynamic dispense is thought to be the short exposure time to moisture during spin-coating. The exposure to moisture mainly occurs during the evaporation of precursor solution. In static dispense, the time for evaporation is longer compared to dynamic dispense, thereby the vapor of the precursor around substrates stays longer. This increases the amount of moisture exposure during spin-coating, resulting in poor optical and electrical performances. Unfortunately, the PVSCs prepared by using either dynamic or static dispense cannot solve the hysteresis problems.

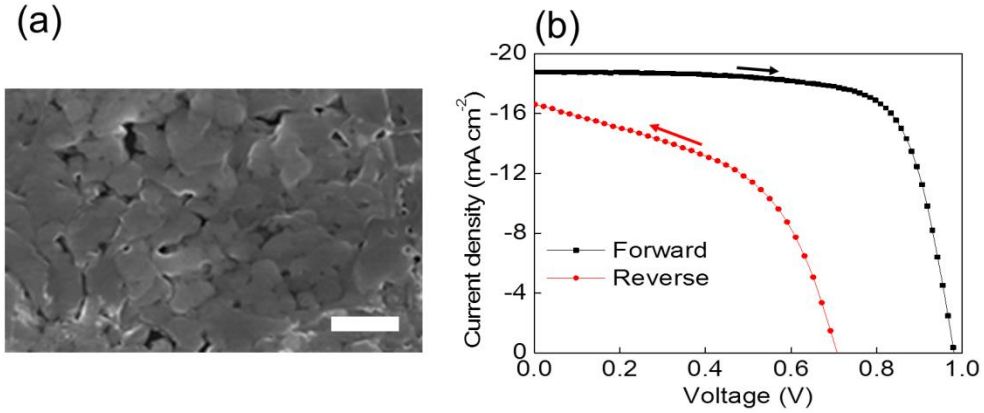

Figure 2-9. (a) SEM image of perovskite layer processed by dynamic dispense (the scale bar is 1 μm). (b) *J-V* characteristics of PVSCs with different sweep direction.

Figure 2-9a shows scanning electron microscope (SEM) image of the surface of the perovskite layers processed by dynamic dispense. The pin-holes are observed, leading to possible short path ways.[16-18] The pin-holes of perovskite layers prepared by static dispense is more severe (not shown here). The rough surface with pin-holes eventually leads to hysteresis problems shown in Figure 2-9b. Unlike typical hysteresis,[19-21] the PVSCs developed here show better performance when the bias direction is forward.

In Figure 2-8b, the transmittances of perovskite layers on ITO/PEDOT/PSS prepared by dynamic dispense are higher than that of substrates by static dispense under the same conditions of precursor concentration and spin-coating speed. Thus, it is considered that dynamic dispense might be also advantageous for semi-transparent perovskite layers, which can be applied into semi-transparent PVSCs. Perovskite layers using 36 wt% is still opaque (Figure 2-10a). Though the backward scattering of perovskite layers processed by dynamic dispense is lower than that of static dispense, the value of backward scattering is still high (Figure 2-6a) enough to make the substrates opaque. Thus, thinner perovskite layer was produced by using diluted precursor (22 wt%) and showed good visual transparency because of the thin layer (Figure 2-10a, bottom). Figure 2-10b shows the *J-V* characteristics of the PVSCs with different concentration of precursors. The thickness of the back silver electrode is 100 nm, and thereby the PVSCs are non-transparent cells. The performances of the PVSCs with thin perovskite layer are lower due to the low value of J_{sc} and V_{oc}. The low value of J_{sc} is due to low light absorption because of the thin perovskite layer. The decrease in V_{oc} might stem from the short path ways between ITO and the back silver electrode due to thin perovskite layer with many pin-holes.

By using a thin silver layer (10 nm) as a back electrode, semi-transparent PVSCs using

22 wt% of perovskite precursor were fabricated (not shown here). However, all cells were short-circuited, implying that another fabrication method of perovskite layers is needed for semi-transparent PVSCs.

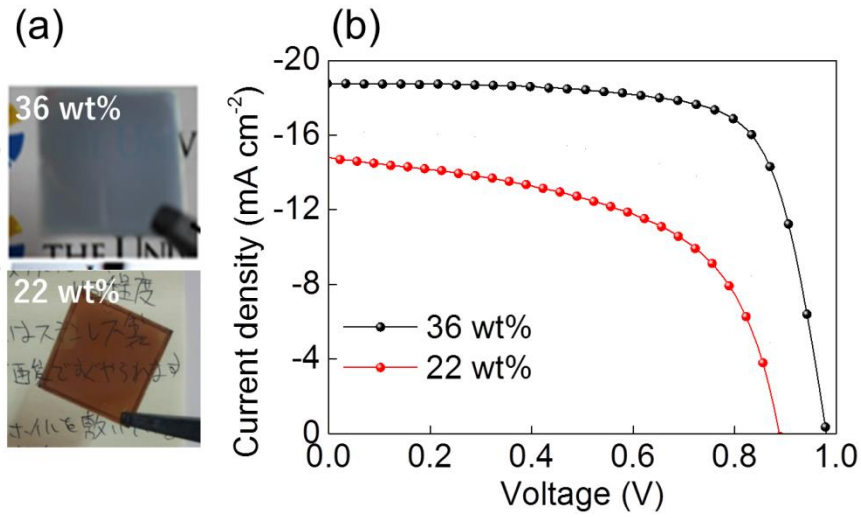

Figure 2-10. (a) Perovskite layers prepared by dynamic dispense (b) *J-V* characteristics of the PVSCs. Concentration of perovskite precursors is either 36wt% or 22wt%.

2-5 PVSCs with HTL on ITO prepared by SSVD method

2-5-1 Procedure

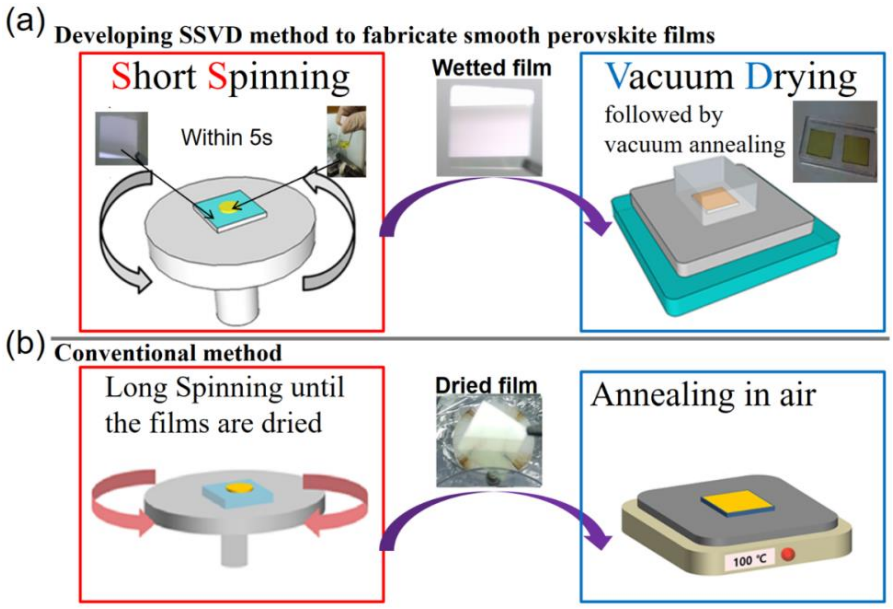

Figure 2-11. Fabrication method of perovskite layers processed by (a) SSVD and (b) conventional method.

So far, the advantages of dynamic dispense have been described. It is a superior method for fabrication of perovskite layers to static dispense because it reduces the exposure time to moisture during the evaporation of perovskite precursors. However, the intrinsic problems regarding pin-holes and hysteresis have not yet been solved. As mentioned above, the exposure to moisture during the evaporation of perovskite precursor is critical to final perovskite films. Minimization of exposure to moisture is important.

Here, a novel method to fabricate perovskite films using small vacuum chamber is presented. Figure 2-11 illustrates the comparison between the novel method, namely short-spinning and vacuum-drying (SSVD) method and a conventional method.

The detailed experimental procedures are introduced in experimental sections (2-2). In SSVD, the precursor ink is statically dispensed on the ITO/PEDOT:PSS substrates and spin-coated within 5 s. Because the spin time is extremely short compared to conventional method, in which spin time is over 35 s, the substrates are still wet and transparent with no color (Figure 2-11a, middle). Before the precursor is dried, the substrates are immediately transferred to the vacuum oven and dried without heat treatment. After the precursor ink is fully dried, the color of substrates turns to yellow (inset of vacuum drying in Figure 2-11a) just like the substrates right after the spincoating perovskite precursor by the conventional method (Figure 2-11b, middle). Then, the substrates are annealed for the formation of perovskites under the low pressure.

2-5-2 Optical properties

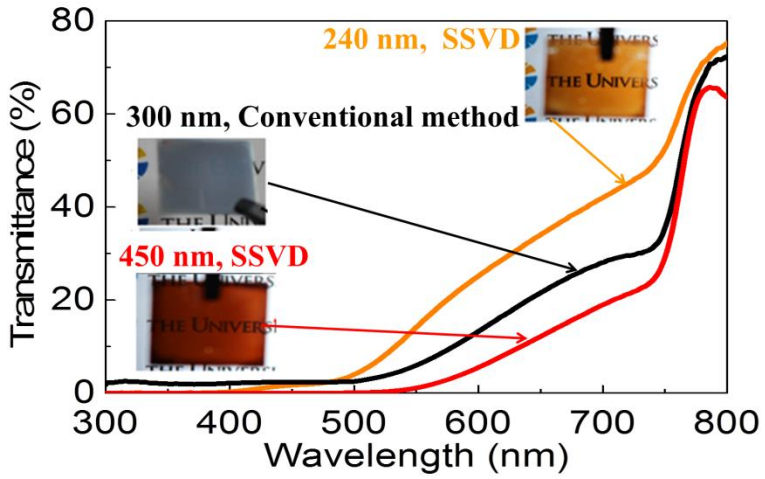

Figure 2-12. Transmittance spectra of the perovskite layers with different thickness on ITO/PEDOT:PSS substrates processed by either SSVD or conventional method.

The perovskite layers processed by SSVD have optically unique properties. For 240 nm-thick and 300 nm-thick perovskite layers shown by the yellow and black lines, respectively, (Figure 2-12) the same concentration of precursor ink (36 wt%) and spin speed (4000 rpm) were used but different processes; the SSVD and conventional methods. Apparently, the film processed by SSVD has superior visual transparency compared to the film by the conventional method. The high value of transmittance measured from the optical spectrum supports the better visual transparency for the film by SSVD. The thickness of the films by SSVD tends to be thinner compared to the films by the conventional method under the same concentration of ink and spin speed.

Interestingly, when the 450 nm-thick perovskite film by SSVD using high concentration of ink (50 wt%) has better visual transparency than the 300 nm-thick perovskite layer processed by the conventional method. Actually, the transmittance of the film by SSVD is lower than that of the film by the conventional method, mainly because of the thick films. This seems to be contradictory. The high visual transparency with low transmittance, can be explained by the degree of scattering, as mentioned below.

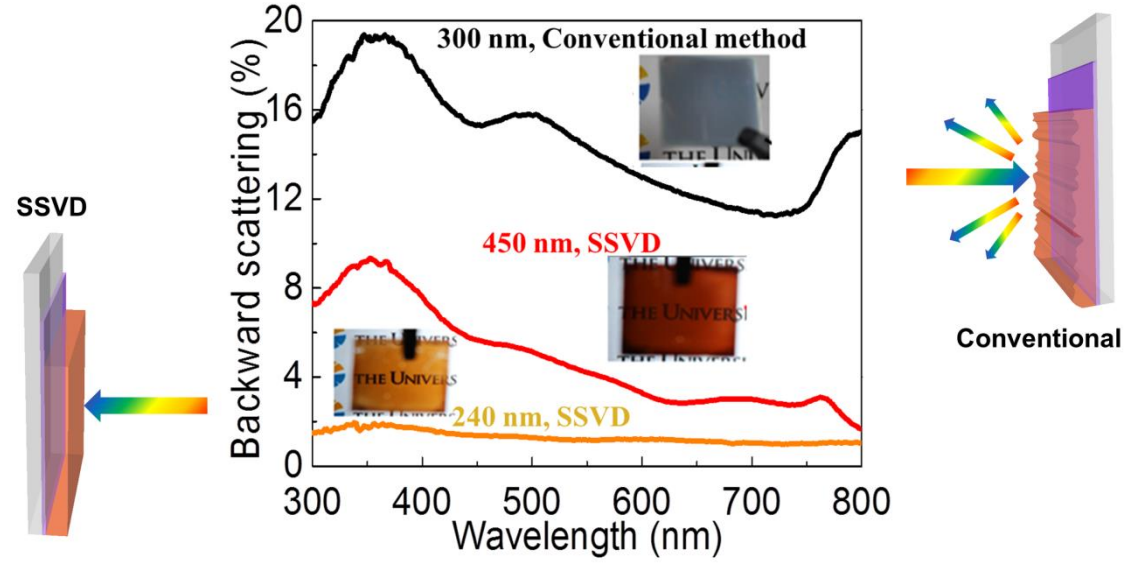

Figure 2-13. Backward scattering spectra of 300 nm-thick perovskite layer prepared by the conventional method and 240, 450 nm-thick perovskite layer by SSVD.

Figure 2-13 shows the backward scattering spectra of the perovskite films prepared under different conditions. The direction of light irradiation is from the air to the perovskite films as depicted on both left and right in Figure 2-13. The scattering of films processed by the conventional method is much higher than that of films processed by

SSVD, recording more than 12% in the entire range of wavelength. The strong scattering from the films processed by the conventional method is ascribed to the rough surface depicted in the scheme on the right in Figure 2-13. As a result, white color is seen for the 300 nm-thick perovskite layer (inset of Figure 2-13).

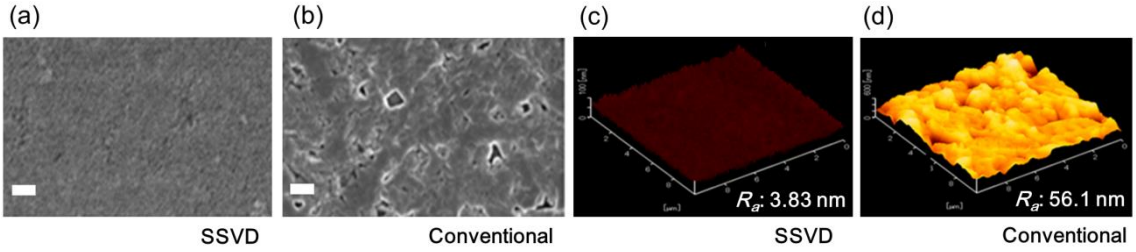

Figure 2-14. (a,b) SEM (the scale bar is 1 μm) and (c,d) AFM images of perovskite layers on ITO/PEDOT:PSS substrates processed by (a,c) SSVD and (b,d) conventional method.

In Figure 2-14, smooth and pin-hole free perovskite films were formed by SSVD confirmed by SEM and atomic force microscope (AFM) images while the perovskite films by the conventional method showed pin-holes and high surface roughness (~56.1 nm). Thus, the low backward scattering comes from the smooth and uniform surface of the perovskite layers by SSVD.

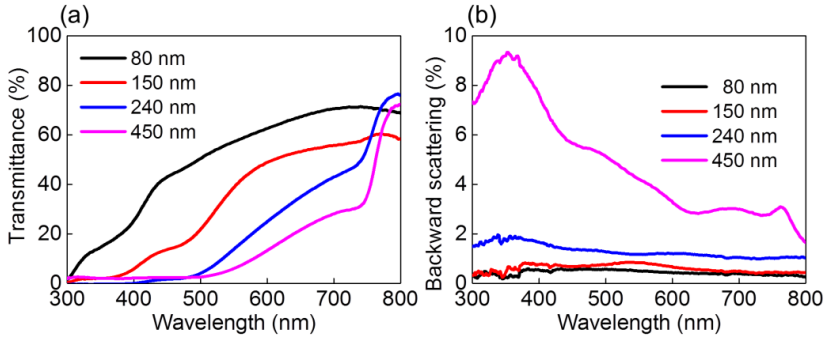

Figure 2-15. (a) Transmittance and (b) backward scattering spectra of the perovskite layers on ITO:PEDOT:PSS substrate with different thickness from 80 nm to 450 nm.

Figure 2-15a shows the transmittance and backward scattering spectra of the perovskite layers with different thicknesses from 80 nm to 450 nm processed by SSVD. The transmittance increases with decreasing the thickness because of the thin layers and low absorption of light. The backward scattering decreases as the perovskite thickness decreases (Figure 2-15b).

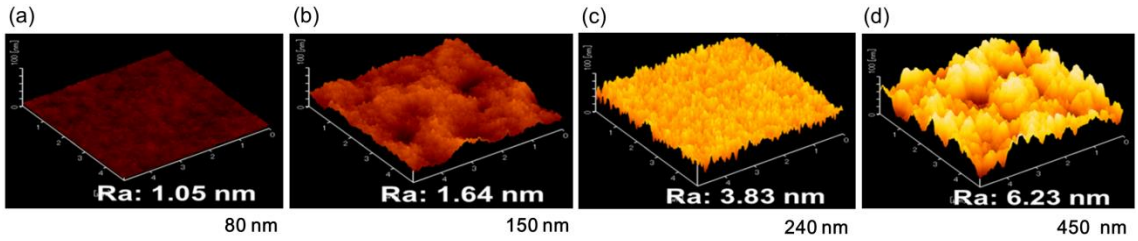

Figure 2-16. AFM images of the perovskite layer processed by the SSVD method with the thickness of (a) 80 nm (b) 150 nm (c) 240 nm and (d) 450 nm.

To find the relationship between the scattering and the thickness of perovskite layer, the surface roughness was examined by AFM images (Figure 2-16a-d). The surface roughness (R_a) of the thick perovskite layer (450 nm) has small value (~6.23 nm) and R_a tends to decrease to ~1.05 nm for thin perovskite layers. This is in accordance with the backward scattering according to the perovskite layer thickness (Figure 2-15b).

Figure 2-17a-d shows the actual pictures of the perovskite layers on ITO/PEDOT:PSS substrates with different thickness from 80 to 450 nm. Regardless of the thickness, perovskite layers from 80 to 450 nm have relatively good visual transparency as the letters behind the films can be seen. These results show that the high transmittance with low scattering of the perovskite films processed by the SSVD method is advantageous for good visual transparency.

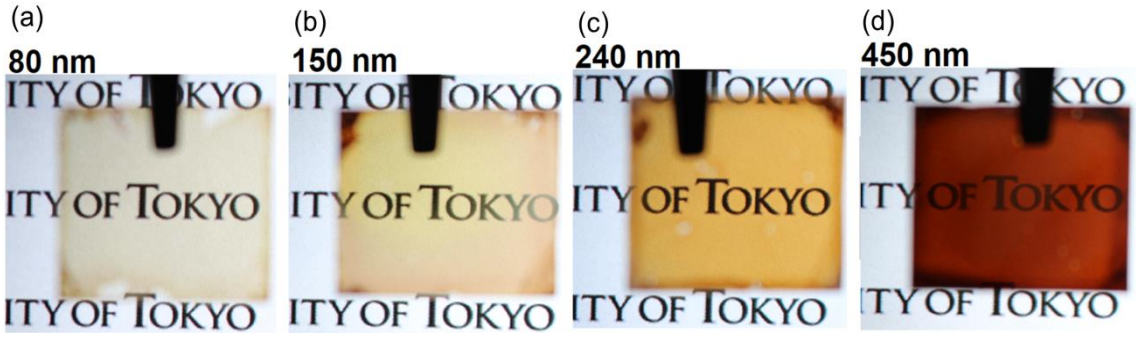

Figure 2-17. Perovskite layers processed by the SSVD method on ITO/PEDOT:PSS substrates with the thickness of (a) 80 nm (b) 150 nm (c) 240 nm and (d) 450 nm.

2-5-3 Importance of short spinning

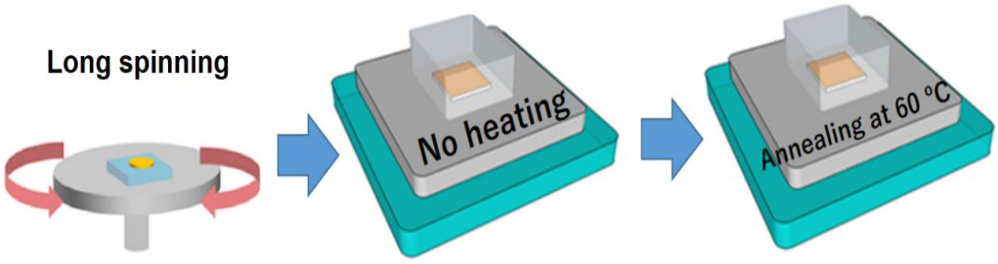

Figure 2-18. Experimental procedure for long spinning time followed by drying and annealing under low pressure.

In SSVD, the three procedures, the short spinning, vacuum drying and vacuum annealing, should be done sequentially. To check the importance of the short spinning, the perovskite precursor was spin-coated on ITO/PEDOT:PSS substrates for 35 s so that the perovskite precursor is dried during spin coating. Then, the substrates are transferred to vacuum chamber for vacuum drying and annealing under 0.05 kPa (Figure 2-18). In a similar manner to the SSVD, precursors were transformed into the perovskites under the low temperature (~60 °C). However, the optical features are similar to the perovskite films processed by the conventional method, showing the white scattering color on the surface (Figure 2-19a).

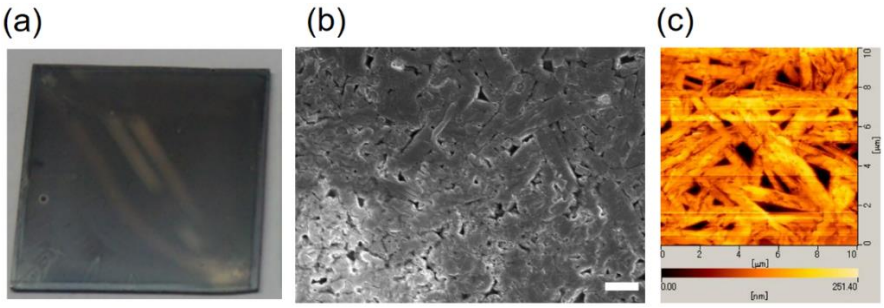

Figure 2-19. (a) Photograph, (b) SEM (the scale bar is 1 μm) and (c) AFM images of the perovskite layer prepared on ITO/PEDOT:PSS by spincoating of the perovskite precursor for 35 s followed by vacuum drying and annealing.

From the SEM image (Figure 2-19b), many pin-holes are seen similarly to the films by the conventional method (Figure 2-14b). R_a of the films by this method records 45.4 nm from the AFM image (Figure 2-19c), which is slightly smaller compared to the films by the conventional method (Figure 2-14d, R_a: 56.1 nm). However, R_a is still large

compared to the films by SSVD (Figure 2-16), resulting in strong scattering. Thus, undried perovskite precursor after spincoating is prerequisite for the vacuum drying and vacuum annealing for the smooth and semi-transparent perovskite films.

2-5-4 Importance of vacuum drying

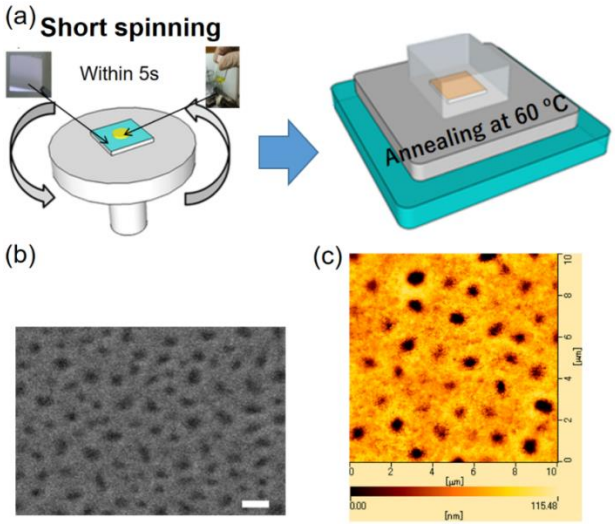

Figure 2-20. (a) Fabrication procedure of perovskite layers based on SSVD without the vacuum drying process. (b) SEM (the scale bar is 1 μm) and (c) AFM image of the perovskite layer processed by the method shown in (a).

Figure 2-20a illustrates a fabrication scheme of perovskite layers that is similar to the SSVD without the vacuum drying process to check the effectiveness of the drying process under low pressure. The perovskite films processed by this method show the pin-holes. However, the shapes of the pin-holes are rather round-shaped (Figure 2-20c,d) different from the pin-holes of perovskite layers by the conventional method. Also, grain boundary of perovskites is not observed (Figure 2-20c) similar to perovskite layers by SSVD (Figure 2-16) while the grain boundary is large for the perovskite layers by the conventional method (Figure 2-14b). Those pin-holes might cause short-circuiting that deteriorates the electrical performance of PVSCs. Thus, the fast evaporation of perovskite precursor might deteriorates the surface coverage of perovskites on ITO/PEDOT:PSS, resulting in pin-holes after the annealing process.

2-5-5 Importance of vacuum annealing

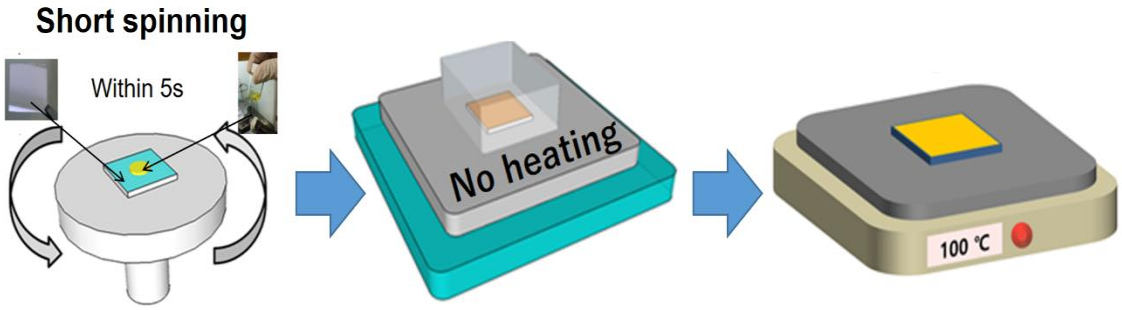

Figure 2-21. Experimental procedure for short spinning followed by drying under low pressure and annealing in ambient air.

Here, perovskite layers were processed under annealing in air after short spinning and vacuum drying to check the effectiveness of the vacuum annealing process. The schematic illustration of the experimental procedure is shown in Figure 2-21. The perovskite films processed by this method are visually transparent similarly to the films by SSVD (Figure 2-22a). This suggests that the short spinning and vacuum drying before annealing is important for the realization of semi-transparent perovskite films. The transmittance of the films processed by the method shown in Figure 2-21 are positioned in between those of the films processed by SSVD and conventional methods (Figure 2-22b). Also the scattering of these films are relatively small in comparsion with that of conventional cells, recording under 5% in entire range (Figure 2-22c). However, the scattering is still a bit larger compared to the films processed by SSVD. Despite the films are semi-transparent, slightly lower transmittance and larger scattering compared to the films by SSVD are observed. These are attributed to slight exposure time to moisture.

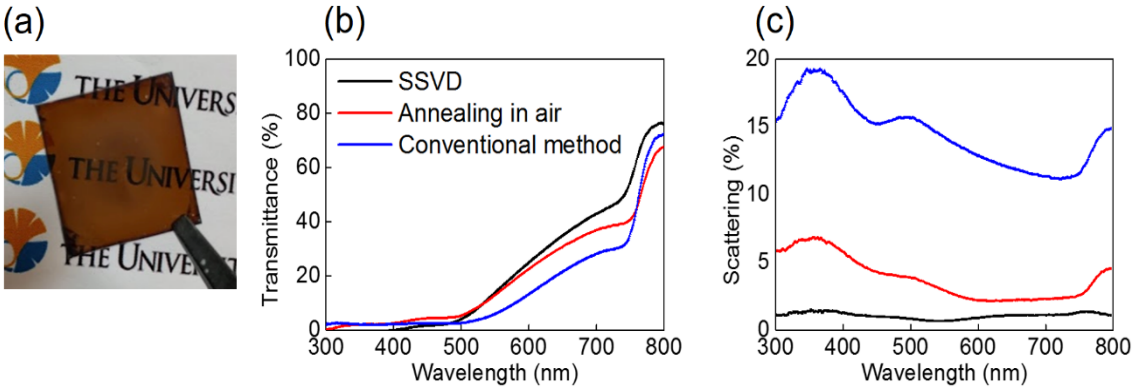

Figure 2-22. (a) Perovskite films on ITO/PEDOT:PSS substrates processed by the method shown in Figure 2-21. (b) Transmittance and (c) backward scattering spectra of perovskite films processed by different methods; SSVD (black), the method illustrated in Figure 2-21 (red), the conventional method (blue).

Generally, perovskite precursors turn to yellow after drying in vacuum chamber (Figure 2-23a) and turn to brown after the formation of perovskite layers under vacuum drying. To proceed annealing in air, the samples are inevitably exposed to moisture during the transferring to a hot plate in air, turning orange color (Figure 2-23b top). When the films are exposed to air for 2 min before annealing in air, the samples turn to grey color and become opaque. These changes indicate the morphology change of perovskite precursor before annealing, affecting the final morphology of perovskite layers after annealing as observed in SEM images (Figure 2-23c,d). When the exposure time to air before annealing in air is longer, many pinholes are formed (Figure 2-23d bottom). Though the samples are promptly transferred to a hot plate in ambient air, small pin-holes are observed (Figure 2-23d top). Thus, minimizing the exposure time to air before annealing is desirable. In this regard, annealing in vacuum after drying in vacuum can be conjectured as an ideal process.

So far, the function of each process in SSVD (short spinning, vacuum drying and vacuum annealing) has been examined in detail. Omitting at least one of three processes may lead to the failure of semi-transparent perovskite films with ultra-smoothness.

Considering the importance of each process, three factors are crucial for final perovskite films by SSVD; i) evaporation of perovskite precursor during spin-coating, ii) slow drying in vacuum and iii) minimized exposure to moisture during the time between vacuum drying and annealing. Thus, it is concluded that the SSVD method minimizes the evaporation of perovskite precursor, reduces the rate of evaporation during vacuum drying and minimizes the exposure to moisture during annealing, thereby producing semi-transparent and ultrasmooth perovskite films.

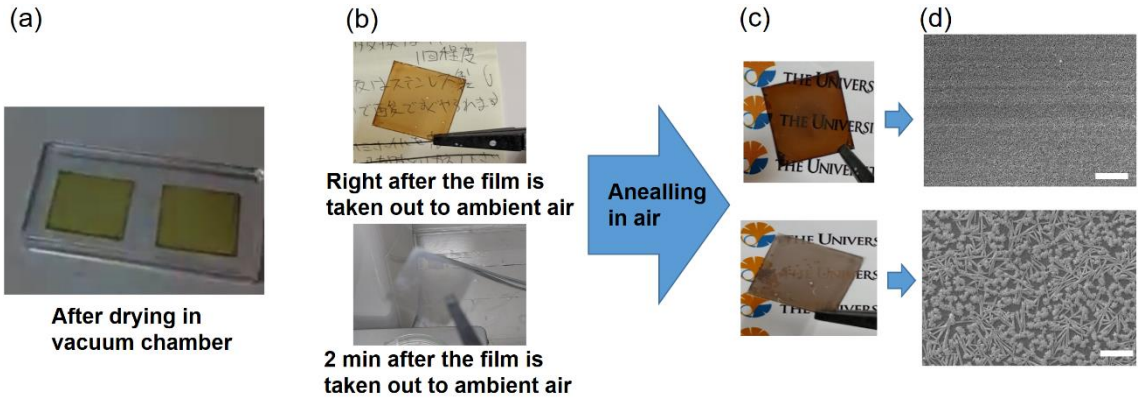

Figure 2-23. (a) The substrates of ITO/PEDOT:PSS/perovskite precursor after short spinning and vacuum drying in vacuum chamber. (b) The substrates right after (top) and 2 min after (bottom) being taken out to the air. (c) the pictures and (d) SEM images of the perovskite layers after annealing from the samples in Figure 2-20b (the scale bar is 1 μm).

2-5-6 Insensitive to annealing temperature

In general, the annealing temperature critically affects the morphology of active layers, which eventually influences the performance of various kinds of solar cells[22] including PVSCs.[23] The sensitivity to annealing temperature of perovskite films processed by SSVD was also examined.

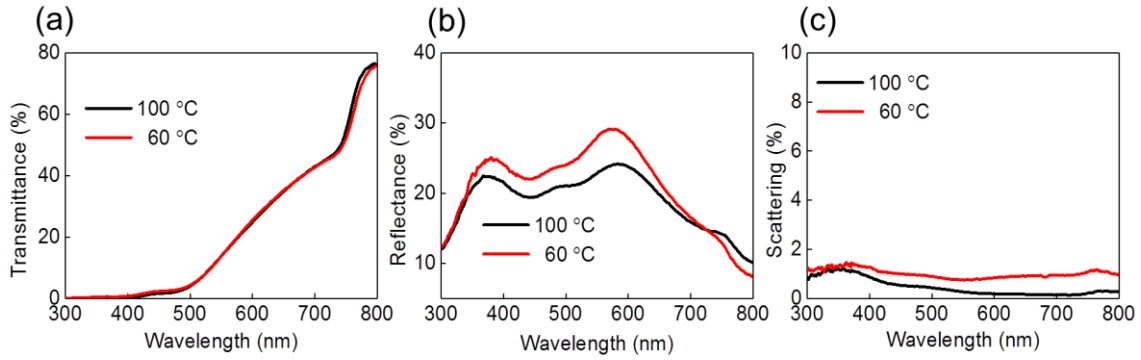

Figure 2-24. (a) Transmittance, (b) reflectance and (c) scattering spectra of the perovskite layers on ITO/PEDOT:PSS substrates processed by SSVD at different annealing temperatures (60 °C and100 °C).

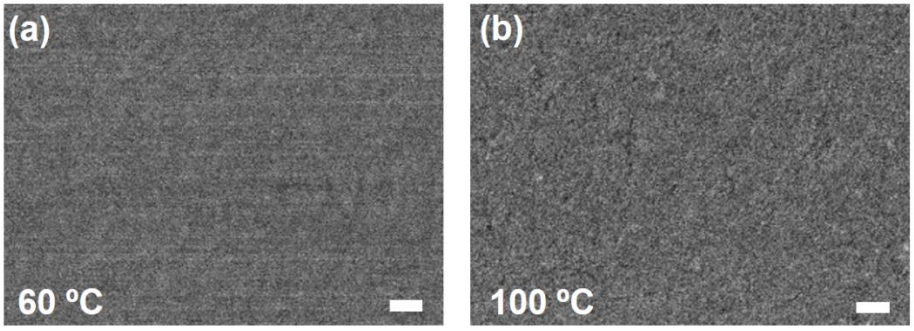

Figure 2-25. SEM images of the perovskite layers on ITO/PEDOT:PSS substrates processed by SSVD annealed at (a) 60 °C and (b) 100 °C (the scale bar is 1 μm).

The optical properties of the perovskite layers processed by SSVD are rarely affected by the annealing temperature, showing similar transmittance, reflectance and scattering when the samples are thermally annealed at 60 °C or 100 °C (Figure 2-24). SEM images in Figure 2-25 further support the insensitivity to annealing temperature. In either the perovskite layer annealed at 60 °C or 100 °C, the smooth surface without pin-holes is observed. It is conjectured that the optical properties of perovskite layers processed by SSVD are not affected by the annealing temperature between 60 °C or 100 °C.

2-5-7 Insensitive to relative humidity

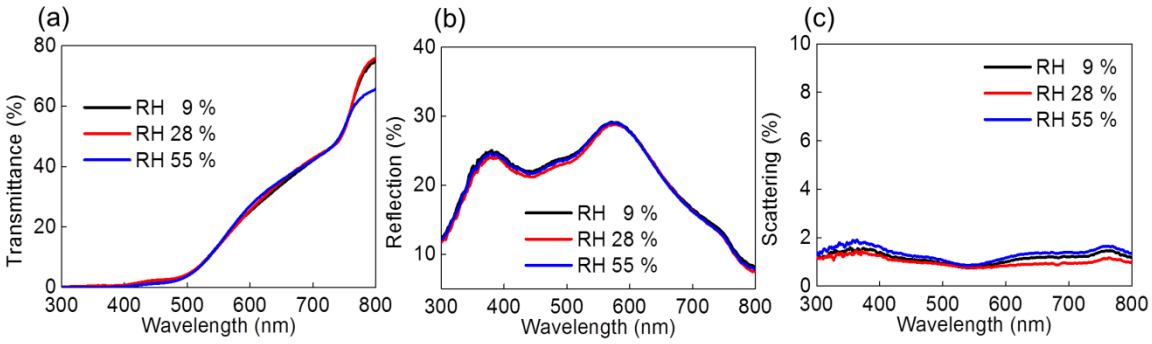

Figure 2-26. (a) Transmittance, (b) reflectance and (c) scattering spectra of the perovskite layers on ITO/PEDOT:PSS substrates processed by SSVD at different relative humidity (RH) during spin-coating.

In the conventional method, relative humidity should be less than 45% during the spincoating, otherwise the electrical properties of PVSCs are extremely poor. Perovskite precursors are easily combined with the moisture in air during the spincoating. As mentioned above, the exposure to moisture is maximized during the evaporation of

perovskite precursors. In SSVD, however, the evaporation does not occur during spin-coating because of the short spinning time (~5 s). Thus, the relative humidity during spin-coating rarely affects the optical properties of perovskite layers processed by SSVD.

As confirmed in Figure 2-26, transmittance, reflectance and scattering of perovskite layers processed at different relative humidity (9, 28 and 55%) show almost identical values, indicating that the optical performances are the same regardless of the relative humidity from 9% to 55%.

Overall, the optical properties of perovskite films processed by SSVD are rarely affected by the annealing temperature and relative humidity, resulting in improved reproducibility. By taking advantage of the reproducibility of PVSCs processed by SSVD, the electrical properties of PVSCs will be introduced in the next section.

2-5-8 Performances of non-transparent PVSCs processed by SSVD

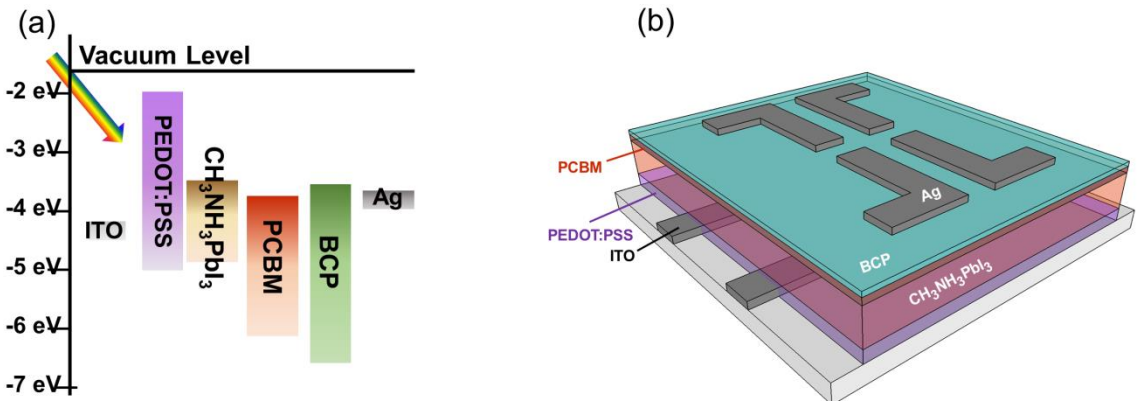

Figure 2-27. (a) Energy diagram and (b) the structure of PVSCs processed by SSVD.

Experimentally, it was found out that using BCP as ETL is more reproducible for the fabrication of PVSCs. Thus, the BCP instead of PEI was used and the energy diagram and the structure of the present PVSCs based on SSVD are depicted in Figure 2-27.

Figure 2-28a shows cross-sectional images of the PVSCs processed by SSVD in which a 240-nm-thick perovskite layer is inserted. The planar perovskite layer is clearly seen on PEDOT:PSS layer. All parameters, J_{sc}, V_{oc} and FF, of the PVSCs by SSVD are larger than those of the PVSCs by the conventional method, recording the average PCE of 12.7% (Figure 2-28b); the detailed parameters are presented in Table 2-1.

Table 2-1. Characteristics of the PVSCs prepared by the SSVD[a,b]

	perovskite thickness (nm)	light incidence	J_{sc} (mA cm^{-2})	V_{oc} (V)	FF	PCE (%)
normal cell[a]	240	front	19.22 ± 1.08	0.954 ± 0.098	0.64 ± 0.064	12.7 ± 1.60
semi-transparent cell[b]		front	11.08 ± 0.65	1.02 ± 0.014	0.61 ± 0.023	6.87 ± 0.44
	150	back	8.84 ± 0.2	0.98 ± 0.059	0.57 ± 0.031	5.13 ± 0.25
	240	front	16.6 ± 0.82	1.02 ± 0.014	0.64 ± 0.017	10.66 ± 0.35
		back	12.03 ± 1.45	1.01 ± 0.36	0.58 ± 0.059	7.18 ± 1.52

[a]Top electrode = 100 nm thick Ag; the valules were obtained from 17 samples.

[b]Top electrode = 10 nm thick Ag coated with 20 nm thick MoO_3; the values were obtained from 8 samples each.

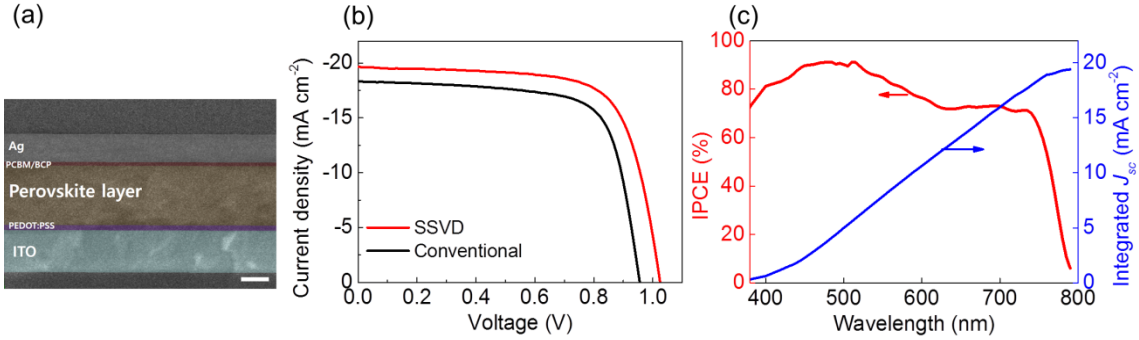

Figure 2-28. (a) Cross-sectional SEM image (the scale bar is 100 nm), (b) *J-V* characteristic (the sweep rate is 100 mV s^{-1}) and (c) IPCE spectra and integrated J_{sc} of a PVSC processed by SSVD. (*J-V* characteristic of the conventional PVSC is also shown in (b).

Integrated J_{sc} calculated from the incident photon-to-current conversion efficiency (IPCE) data of PVSCs by SSVD (Figure 2-28c) records 19.39 mA cm^{-2}, which is similar to the J_{sc} value (19.22 mA cm^{-2}) measured under AM 1.5 G light, indicating that the measured IPCE is reliable. Besides the higher performances compared to the conventional PVSCs, the PVSCs processed by SSVD are also electrically stable.

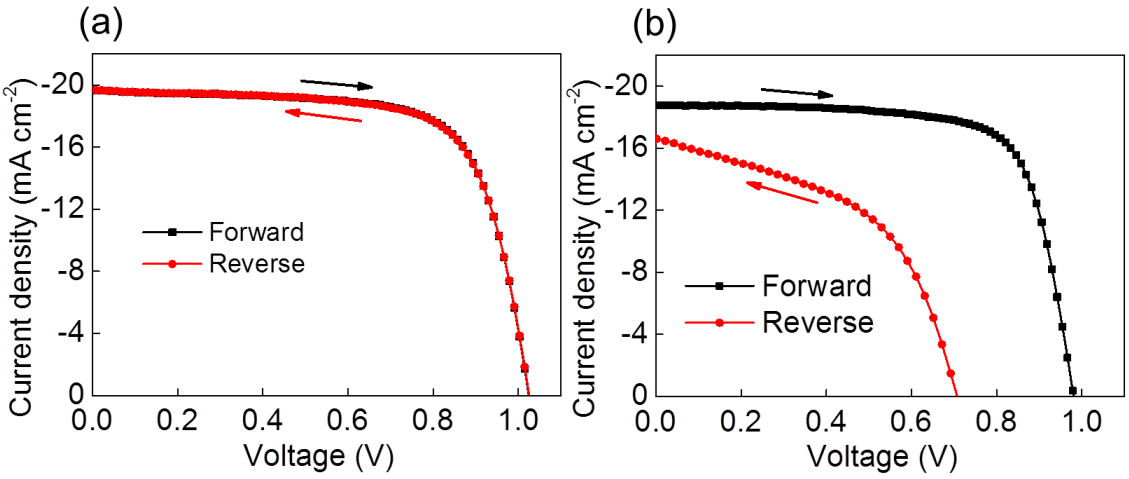

Figure 2-29. *J-V* characteristics with forward and reverse voltage sweep of the PVSCs processed by (b) SSVD and (c) conventional method. The sweep speed is 100 mV s^{-1}.

The *J-V* characteristics of PVSCs processed by SSVD were not dependent on the voltage sweeping direction (Figure 2-29a). However, severe hysteresis was observed for the PVSCs processed by conventional method, making the cells unreliable (Figure 2-29b).

Though the several explanations regarding the hysteresis of PVSCs have been reported, the actual mechanisms are still unclear. Based on the results obtained here, it is conjectured that the interface between the perovskite layers and PCBM might be the main cause for hysteresis since the other experimental procedures except the method to fabricate perovskite layers are basically the same for the SSVD and conventional methods.

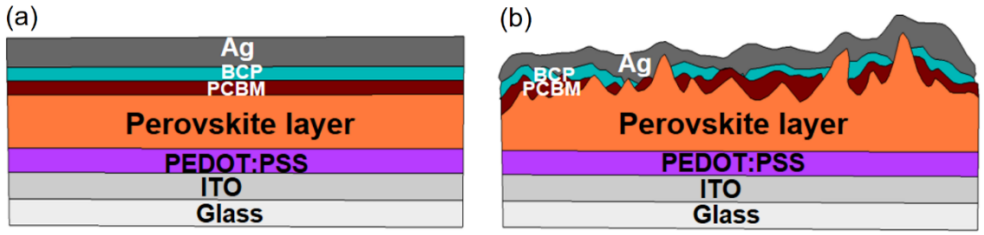

Figure 2-30. Scheme of cross sectional images of the PVSCs processed by (a) SSVD and (b) conventional method.

PCBM layers can cover the perovskite layers processed by SSVD well because of the planar and smooth surface (Figure 2-30a). This prevents the potential short pathways

through which the back silver electrodes directly contact with perovskite layers, thereby no hysteresis appears. The short pathways commonly occur when the perovskite layers are processed by the conventional method because of the rough surface because of the direct contact between the silver electrodes and the perovskite layers (Figure 2-30b). Thus, the severe hysteresis occurs and the V_{oc} drops for the PVSCs processed by the conventional method.

Previously, it was presented that the optical properties of perovskite layers processed by SSVD are not sensitive to the annealing temperature and relative humidity during spin-coating. Here, the electrical properties of PVSCs processed at different annealing temperatures and relative humidities were also examined.

In Figure 2-31a, *J-V* characteristics of PVSCs annealed at 60 °C and 100 °C are shown. Similar to the optical properties of perovskite films prepared at different annealing temperature (Figure 2-24), the electrical properties are also rarely affected by the annealing temperature.

Also, PVSCs by SSVD have similar electrical performances when the relative humidity ranges from 9% to 55% (Figure 2-31b), which is in accordance with the similar optical properties (Figure 2-26).

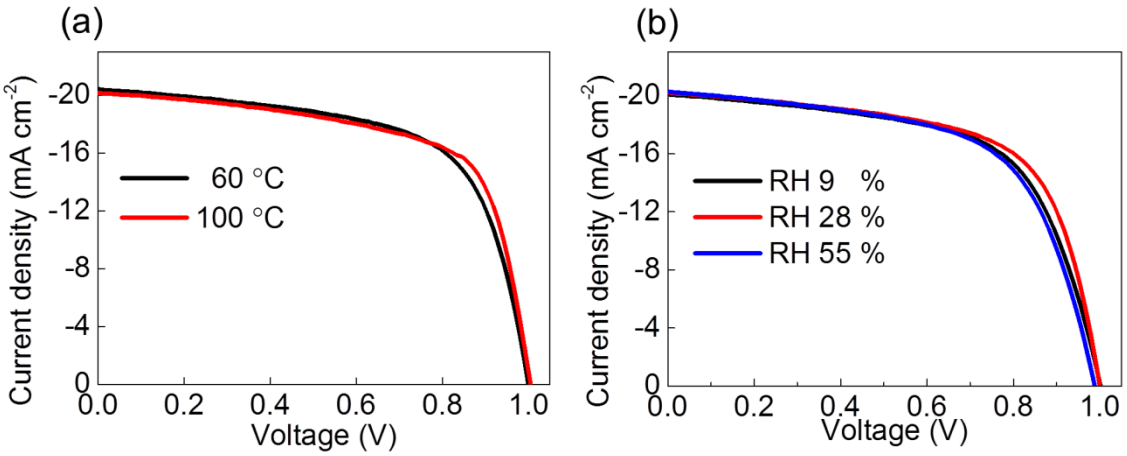

Figure 2-31. *J-V* characteristics of PVSCs with 240-nm-thick perovskite layers processed by SSVD at different (a) annealing temperatures and (b) relative humidities. The sweep rate is 100 mV s^{-1}.

2-5-9 Performances of the semi-transparent PVSCs processed by SSVD

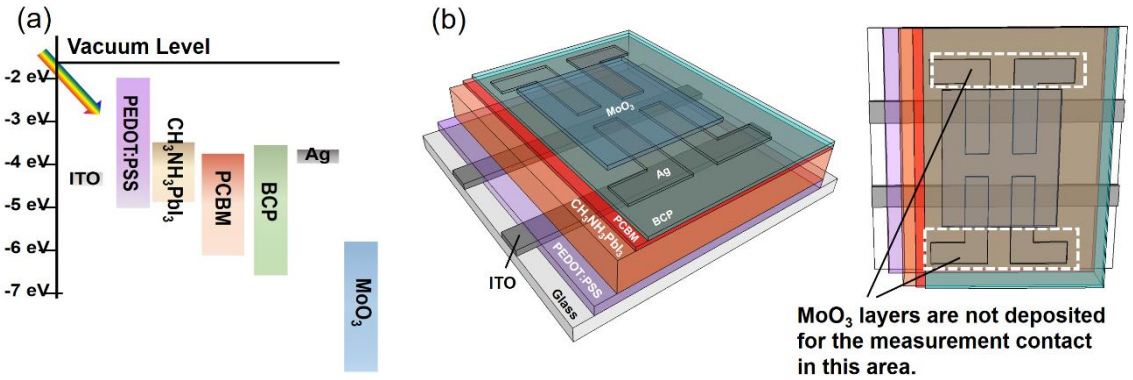

Figure 2-32. (a) Energy diagram and (b) structure of semi-transparent PVSCs processed by SSVD.

Semi-transparent electrodes are widely used with semi-transparent active layers to form transparent solar cells.[24-26] Despite the similarity to OSCs, which are applied to semi-transparent cells, reports regarding semi-transparent PVSCs are relatively few mainly because the transparency of perovskite layers is low.

The transparency of perovskite layers has been improved by the development of SSVD. Thus, the semi-transparent PVSCs were also investigated here by applying transparent electrodes. It has been known that a dielectric-metal-dielectric stacking structures can enhance optical transmittance of a metal film.[27] The multiple layers consisting of high refractive index (*n*)/ low *n*/ high *n* materials sequentially could result in the optimum zero-reflection condition, thereby enhance transmittance.[28] Recently, the combination of BCP/Ag/MoO_3 was also reported, improving transmittance by a similar manner.[29]

Thus, thin layers of Ag (10 nm) and MoO_3 (20 nm) were used as transparent electrodes on BCP layers for the semi-transparent PVSCs. The energy diagram and the structure of semi-transparent PVSCs processed by SSVD using these transparent electrodes are depicted in Figure 2-32. In the actual cells, MoO_3 layers only cover silver back electrodes at around the effective area of the cells, which is the intersection between ITO and silver back electrodes, and MoO_3 is not deposited in the white dashed boxes (Figure 2-32b) for the contact of Ag with the measurement tools.

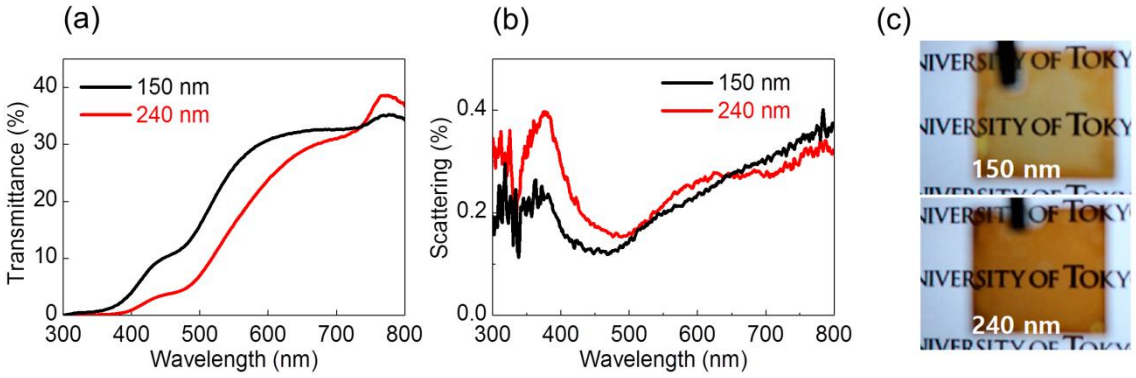

Figure 2-33. (a) Transmittance and (b) scattering spectra and (c) the photographs of the semi-transparent PVSCs with 150-nm and 240-nm-thick perovskite layers.

Here, the transparent PVSCs with two different thicknesses (240 nm and 150 nm) were presented and the transmittance and the scattering of these cells are shown in Figure 2-33. Compared to the transmittance of perovskite layers processed by SSVD, that of semi-transparent PVSCs is smaller because of the semi-transparent electrodes consisting of Ag/MoO_3 (Figure 2-32a). PVSCs with 150-nm-thick perovskite layers show better transmittance than PVSCs with 240-nm-thick perovskite layers due to the thin active layers. Scattering is another factor that determines the visual transparencies, which was dealt with previously. Thus, the scattering of the semi-transparent PVSCs was also measured and shown in Figure 2-33b. The scattering is extremely low recording ~0.5% in entire range of wavelength for both PVSCs with 150-nm and 240-nm-thick perovskite layers. It is considered that the electrode surface is smooth because the PCBM layer coated on the smooth perovskite layer processed by SSVD should also be smooth. Figure 2-33c shows the photographs of the semi-transparent PVSCs for which the transmittance and scattering were measured. The semi-transparent PVSCs with 150-nm-thick perovskite layer show visually good transparency. Also, the cells with 240-nm-thick perovskite layer have adequately good visual transparency due to the low value of scattering even though the layers are thick.

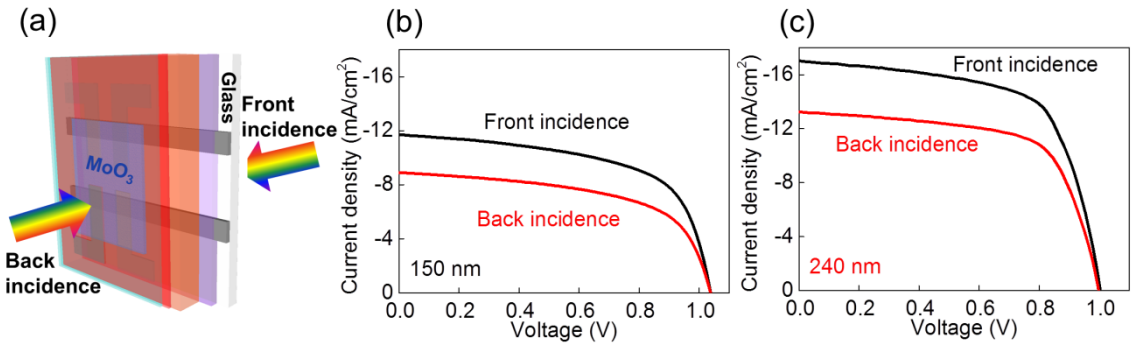

Figure 2-34. (a) Directions of light irradiation and (b,c) *J-V* characteristics of the semi-transparent PVSCs with (b) 150-nm-thick and (c) 240-nm-thick perovskite layers. The sweep rate is 100 mV s^{-1}.

J-V characteristics of the PVSCs with 150-nm and 240-nm-thick perovskite layers were also measured (Figure 2-34b,c). Because of the transparency on both sides for the semi-transparent PVSCs, light irradiation to both sides is possible. Here, the light irradiation from glass/ITO and MoO_3 are defined as front and back incidence each (Figure 2-34a). Since the transparency of Ag/MoO_3 is lower than that of ITO, the PCEs of the front incidence for both of the cells are higher than that of the back incidence. The semi-transparent PVSCs with 150 nm-thick perovskite layers exhibit the PCE values of 6.87% and 5.13% for the front and back incidence. When the perovskite layers are thicker (240 nm), the PCE values are increased, recording 10.66% and 7.18% for the front and back incidence. The detailed parameters of performances are presented in Table 2-1.

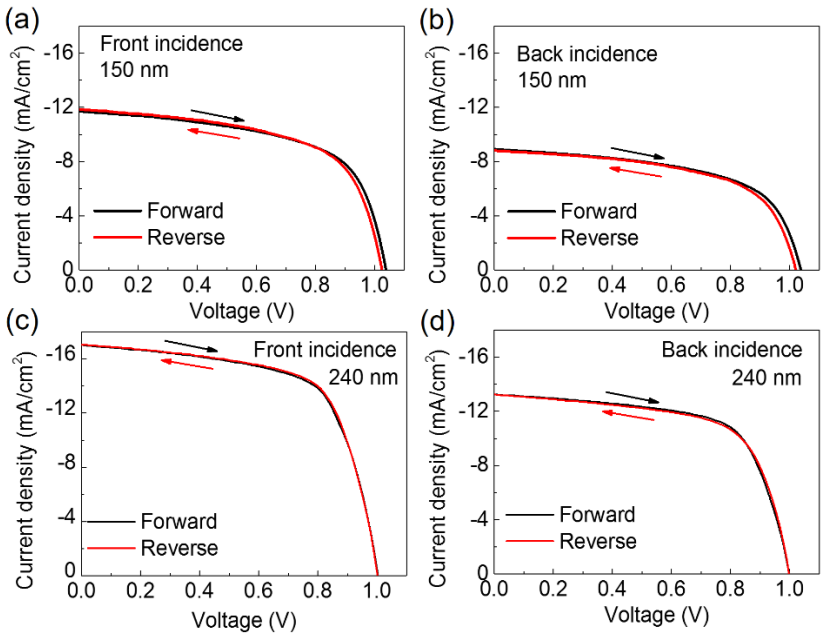

Figure 2-35. *J-V* characteristics of semitransparent PVSCs measured by forward and reverse sweep for the front and back incidences (a,b) with 150-nm-thick perovskite layers and (c,d) with 240-nm-thick-perovskite layers. The sweep rate is 100 mV s^{-1}.

Figure 2-35 shows the *J-V* characteristics of semi-transparent PVSCs developed herein measured by forward and reverse sweeping. The cells with thin layers (150 nm, Figure 2-35a,b) show slight hysteresis for both front and back incidence whereas the thick cells (240 nm, Figure 2-35c,d) exhibit the negligible hysteresis.

To further examine the hysteresis, the semi-transparent PVSCs were measured at different sweep rate of 50, 100 and 200 mV s^{-1} (Figure 2-36). It is noted that the most cells here were measured at 100 mV s^{-1}, unless specifically stated otherwise. In Figure 2-36a,b, slight hysteresis is also observed for the cells with thin perovskite layers. For both front and back incidence, cells showed the best performances at the sweep rate of 100 mV s^{-1}, and slightly decreased at 50 and 200 mV s^{-1}. In the case of the thick cells (Figure 2-36c,d), *J-V* curves are not affected by the sweep rate, in accordance with no hysteresis in Figure 2-35c,d.

Overall, hysteresis was observed for the semi-transparent PVSCs with 150-nm-thick perovskite layer, the performance of which slightly depends on the sweep direction and rate. This might be caused from the unbalanced hole and electron movements[30] from the thin perovskite layers and low conductivity of the transparent electrodes.

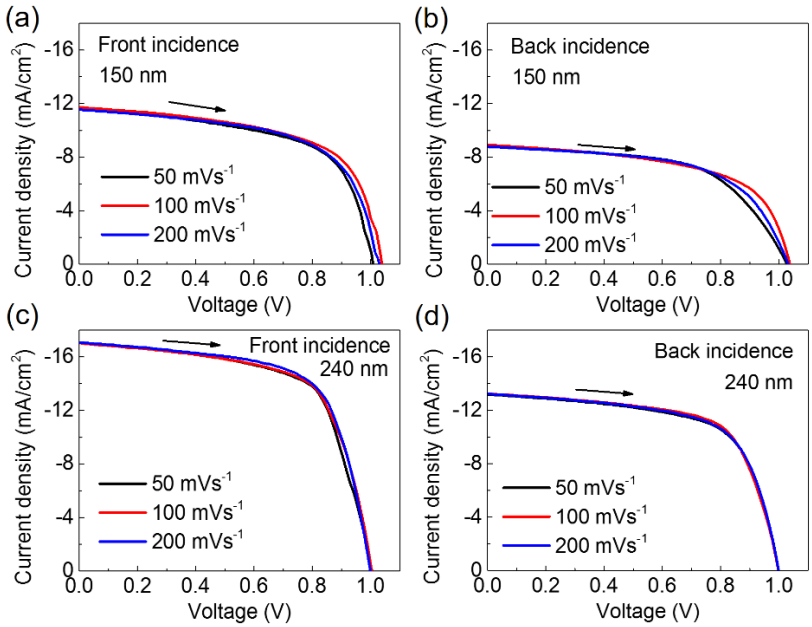

Figure 2-36. *J-V* characteristics of the semitransparent PVSCs measured at different sweep rate (50, 100, 200 mV s^{-1}) for the front and back incidence (a,b) with 150 nm-thick perovskite layers and (c,d) with 240 nm-thick perovskite layers. The sweep direction is forward bias.

2-6 Conclusions

In this chapter, simple methods to fabricate perovskite layers were introduced. By coating the perovskite precursors dynamically during spin-coating, high performance PVSCs were obtained with good reproducibility compared to the PVSCs by static dispense. However, the intrinsic problems such as hysteresis and the pinholes of perovskite layers were not solved by this method. Considering the importance of minimizing the exposure to moisture during evaporation of perovskite precursors, the SSVD method was newly devised. By preventing the evaporation of perovskite precursors by short spinning and blocking the exposure to moisture by vacuum drying, semi-transparent perovskite films were obtained. The superior visual transparency of the perovskite films stems from the pin-hole free and ultrasmooth surface which suppresses the scattering. The performances of PVSCs processed by SSVD are superior, showing high PCEs and no hysteresis. Lastly, the transparent PVSCs were developed using Ag/MoO_3 as transparent electrodes. The semi-transparent PVSCs showed good visual transparencies and high PCE values over 10% for the cells with 240-nm-thick perovskite layer when the light was irradiated from front sides, which can pave the way for the next semi-transparent photovoltaic fields.

2-7 References

1. J. Y. Jeng, Y. F. Chiang, M. H. Lee, S. R. Peng, T. F. Guo, P. Chen and T. C. Wen, *Adv. Mater.*, 2013, **25**, 3727-3732.
2. P. W. Liang, C. Y. Liao, C. C. Chueh, F. Zuo, S. T. Williams, X. K. Xin, J. Lin and A. K. Y. Jen, *Adv. Mater.*, 2014, **26**, 3748-3754.
3. C.-H. Chiang, Z.-L. Tseng and C.-G. Wu, *J. Mater. Chem. A*, 2014, **2**, 15897-15903.
4. P. Docampo, J. M. Ball, M. Darwich, G. E. Eperon and H. J. Snaith, *Nat. Commun.*, 2013, **4**.
5. T. Leijtens, G. E. Eperon, S. Pathak, A. Abate, M. M. Lee and H. J. Snaith, *Nat. Commun.*, 2013, **4**, 2885.
6. R. Lindblad, D. Bi, B.-w. Park, J. Oscarsson, M. Gorgoi, H. Siegbahn, M. Odelius, E. M. J. Johansson and H. k. Rensmo, *J. Phys. Chem. Lett.*, 2014, **5**, 648-653.
7. N. Ahn, D.-Y. Son, I.-H. Jang, S. M. Kang, M. Choi and N.-G. Park, *J. Am. Chem. Soc.*, 2015, **137**, 8696-8699.
8. H.-S. Ko, J.-W. Lee and N.-G. Park, *J. Mater. Chem. A*, 2015, **3**, 8808-8815.
9. F. Giordano, A. Abate, J. P. C. Baena, M. Saliba, T. Matsui, S. H. Im, S. M. Zakeeruddin, M. K. Nazeeruddin, A. Hagfeldt and M. Graetzel, *Nat. Commun.*, 2016, **7**, 10379.
10. J. Choi, S. Song, M. T. Hörantner, H. J. Snaith and T. Park, *ACS Nano*, 2016, **10**, 6029-6036.
11. Y. Zhou, C. Fuentes-Hernandez, J. Shim, J. Meyer, A. J. Giordano, H. Li, P. Winget, T. Papadopoulos, H. Cheun and J. Kim, *Science*, 2012, **336**, 327-332.
12. Y. Zhou, C. Fuentes-Hernandez, J. W. Shim, T. M. Khan and B. Kippelen, *Energy Environ. Sci.*, 2012, **5**, 9827-9832.
13. A. K. K. Kyaw, D. H. Wang, V. Gupta, J. Zhang, S. Chand, G. C. Bazan and A. J. Heeger, *Adv. Mater.*, 2013, **25**, 2397-2402.
14. H. Zhang, H. Azimi, Y. Hou, T. Ameri, T. Przybilla, E. Spiecker, M. Kraft, U. Scherf and C. J. Brabec, *Chem. Mater.*, 2014, **26**, 5190-5193.
15. G. E. Eperon, V. M. Burlakov, P. Docampo, A. Goriely and H. J. Snaith, *Adv. Funct. Mater.*, 2014, **24**, 151-157.
16. J. M. Ball, M. M. Lee, A. Hey and H. J. Snaith, *Energy Environ. Sci.*, 2013, **6**, 1739-1743.
17. D. Liu, M. K. Gangishetty and T. L. Kelly, *J. Mater. Chem. A*, 2014, **2**, 19873-19881.
18. S. Chavhan, O. Miguel, H.-J. Grande, V. Gonzalez-Pedro, R. S. Sánchez, E. M. Barea, I. Mora-Seró and R. Tena-Zaera, *J. Mater. Chem. A*, 2014, **2**, 12754-12760.
19. E. L. Unger, E. T. Hoke, C. D. Bailie, W. H. Nguyen, A. R. Bowring, T. Heumüller, M. G. Christoforo and M. D. McGehee, *Energy Environ. Sci.*, 2014, **7**, 3690-3698.
20. H. J. Snaith, A. Abate, J. M. Ball, G. E. Eperon, T. Leijtens, N. K. Noel, S. D. Stranks, J. T.-W. Wang, K. Wojciechowski and W. Zhang, *J. Phys. Chem. Lett.*, 2014, **5**, 1511-1515.
21. H.-S. Kim and N.-G. Park, *J. Phys. Chem. Lett.*, 2014, **5**, 2927-2934.

22. Y. Kim, S. A. Choulis, J. Nelson, D. D. C. Bradley, S. Cook and J. R. Durrant, *Appl. Phys. Lett.*, 2005, **86**, 063502.
23. A. Dualeh, N. Tétreault, T. Moehl, P. Gao, M. K. Nazeeruddin and M. Grätzel, *Adv. Funct. Mater.*, 2014, **24**, 3250-3258.
24. R. Betancur, P. Romero-Gomez, A. Martinez-Otero, X. Elias, M. Maymó and J. Martorell, *Nat. Photon.*, 2013, **7**, 995-1000.
25. X. Wang, L. Zhi, N. Tsao, Ž. Tomović, J. Li and K. Müllen, *Angew. Chem. Int. Ed.*, 2008, **47**, 2990-2992.
26. J. Wu, H. A. Becerril, Z. Bao, Z. Liu, Y. Chen and P. Peumans, *Appl. Phys. Lett.*, 2008, **92**, 237.
27. B. Tian, G. Williams, D. Ban and H. Aziz, *J. Appl. Phys.*, 2011, **110**, 104507.
28. K. Hong, K. Kim, S. Kim, I. Lee, H. Cho, S. Yoo, H. W. Choi, N.-Y. Lee, Y.-H. Tak and J.-L. Lee, *J. Phys. Chem. C*, 2011, **115**, 3453-3459.
29. G. H. Jung, K. Hong, W. J. Dong, S. Kim and J. L. Lee, *Adv. Energy Mater.*, 2011, **1**, 1023-1028.
30. M. M. Mandoc, L. J. A. Koster and P. W. M. Blom, *Appl. Phys. Lett.*, 2007, **90**, 133504.

Chapter 3

Photocurrent enhancement of perovskite solar cells by electrode-coupled plasmons

3-1 Introduction

Various methods to fabricate perovskite[1-3] films have been developed since 2009 when the first perovskite solar cells (PVSCs) were emerged.[4] With the help of advanced fabrication technologies, the power conversion efficiencies (PCEs) have progressed rapidly recording more than 20% in 2016.[5] Also, application of flexible[6, 7] and semi-transparent cells has become possible by controlling the morphologies of perovskite layers presented in Chapter 2.

However, the development of PVSCs has started to show signs of stagnation because the PCEs have nearly reached the theoretical limits.[8, 9] Thus, new approach should be presented to further improve the PCEs of PVSCs. Metal nanoparcticles (MNPs), which have unique properties that are not observed in bulk metals such as localized surface plasmon resonances (LSPRs) (the detail explanation in Chapter 1), have been widely used in organic solar cells (OSCs) to increase photocurrents as they enhance the amount of light into the active layers by near field and far field scattering.[10-12] The use of MNPs in PVSCs has been seldom reported despite a tremendous potential of MNPs. Actually, the enhancement of photocurrents by MNPs in PVSCs is not greatly expected due to two factors; i) high internal quantum efficiency (IQE) of PVSCs due to high absorption coefficient of perovskite layers[13, 14] and ii) plasmonic region of typical MNPs located in the visible light range.[12, 15, 16]

Here, PVSCs in which MNPs are incorporated were presented to enhance the photocurrents of PVSCs. First, silver nanocubes (AgNCs) was chosen and synthesized because AgNCs show both intense near field and strong far-field scattering.[17-19] To overcome the above-mentioned problems regarding the difficulties of the application of MNPs, AgNCs were implemented into PVSCs on the basis of film-coupled plasmons, in which MNPs and metal films are coupled.[20, 21] The efficacy of film-coupled plasmons-like structures were at first analyzed by the finite-difference time-domain (FDTD) simulation. Then, PVSCs based on the film-coupled-like structures were optically and electrically measured. Finally, the factors to enhance photocurrents of PVSCs were analyzed by comparing the experimental data to simulation results based on FDTD.

3-2 Experimental

3-2-1 Synthesis of AgNCs from CF_3COOAg

The synthetic procedures of AgNCs were based on a method reported elsewhere.[22] A 5.1-mL of ethylene glycol (EG) in a 20-mL glass vial was stirred with the cap opened for 5 min at 145 °C. NaSH (1.5 mM in EG, 60 μL), HCl (3 mM in EG, 0.5 mL), and poly(vinylpyrrolidone) (PVP) (20 mg mL^{-1} in EG, 1.25 mL) were injected into the solution successively. CF_3COOAg (62.3 mg mL^{-1} in EG, 0.4 mL) was injected after a 2-min interval. The sizes of AgNCs were controlled by the reaction time. The stirring time was 180 min to reach 70 nm of AgNCs. Then, the solutions were quenched immediately in cold water to prevent further reaction for 15 min followed by washing with acetone and water twice. Finally, obtained AgNCs were dispersed in 5 mL of either methanol or ethanol. The precursors of AgNCs were stored in the refrigerator as stock solutions.

3-2-2 Synthesis of AgNCs from $AgNO_3$

5 mL of ethylene glycol (EG) was injected in a 20 mL size of vial and heated with stirring in an hot oil bath at 140 °C for 2h. HCl (1 mL, 3 mM in EG) was quickly added. After 10 min, $AgNO_3$ (3 mL, 94 mM in EG) and PVP (3mL, 147 mM in EG) were added accordingly. The solutions were kept stirring for 1.5 h to form AgNCs. The precursors were washed with acetone and diluted in ethanol (EtOH) (5 mL).

3-2-3 Preparation of substrates on the basis of film-coupled plasmons

The glasses were pre-cleaned by water, acetone and 2-propanol for 15 min each by sonication followed by oxygen plasma treatment for 40 s with the setting of 30 A and 30 cc of oxygen flow. phenyl-C_{61}-butyric acid methyl ester (PCBM) (1.8 wt% in CB, 30 μL) was coated on the glass at 3000 rpm for 45 s. The precursors of AgNCs (15 μL) were coated dynamically on PCBM at 3000 rpm. The substrates were transferred to an evaporation chamber. 10 nm of bathocuproine (BCP) is evaporated at a rate of 0.01 nm s^{-1} followed by deposition of 100 nm of Ag at a rate of 0.2 nm s^{-1}.

3-2-4 Preparation of PVSCs

The fabrication methods of the substrates consisting of ITO/ poly(3,4-ethylenedioxythiophene):poly(styrene sulfonate) (PEDOT:PSS) were the same as the procedures based on short spinning and vacuum drying (SSVD), which were introduced in Chapter 2. 240 nm-thick perovskite layers were formed by SSVD using 36 wt% perovskite precursors (3:1 molar ratio of CH_3NH_3I and $PbCl_2$). It is noted that

180 nm-thick-perovskite layers were fabricated from SSVD using 28 wt% of pre-heated perovskite precursors at 60 °C; thicker perovskite layers were formed by pre-heating perovskite precursors (the average thickness of perovskite layers is 150 nm when 28 wt% of precursors are used without preheating).

Here, PCBM (1.8 wt% in CB) was coated on the perovskite layers at higher speed of 3000 rpm for 35s to form thin PCBM layers. Then, precursors of AgNCs were spin-coated on PCBM at 4000 rpm. The substrates were transferred to an evaporation chamber where 10 nm of BCP and 100 nm of Ag were coated sequentially.

3-2-5 Characterization

The same methods as those described in Chapter 2 were used.

3-2-6 Simulation

Optical spectra of AgNCs and electric field distributions were simulated by FDTD method using FDTD Solutions (Lumerical Solutions). The simulation domain (1 × 1 × 1 μm) consisted of 4 nm cubic cells and the central region (190 × 190 × 190 nm) around a AgNC was further meshed with a three-dimensional grid of 1 nm spacing. Backward scattering from the nanocube was monitored by a 340 × 340 nm square screen set 120 nm apart from the AgNC-PCBM interface. The dielectric functions of Ag and glass were extracted from the literature data.[23] Refractive index values of PCBM and BCP were 2 and 1.7, respectively.

3-3 Synthesis of AgNCs

3-3-1 Synthesis using $AgNO_3$ as precursor

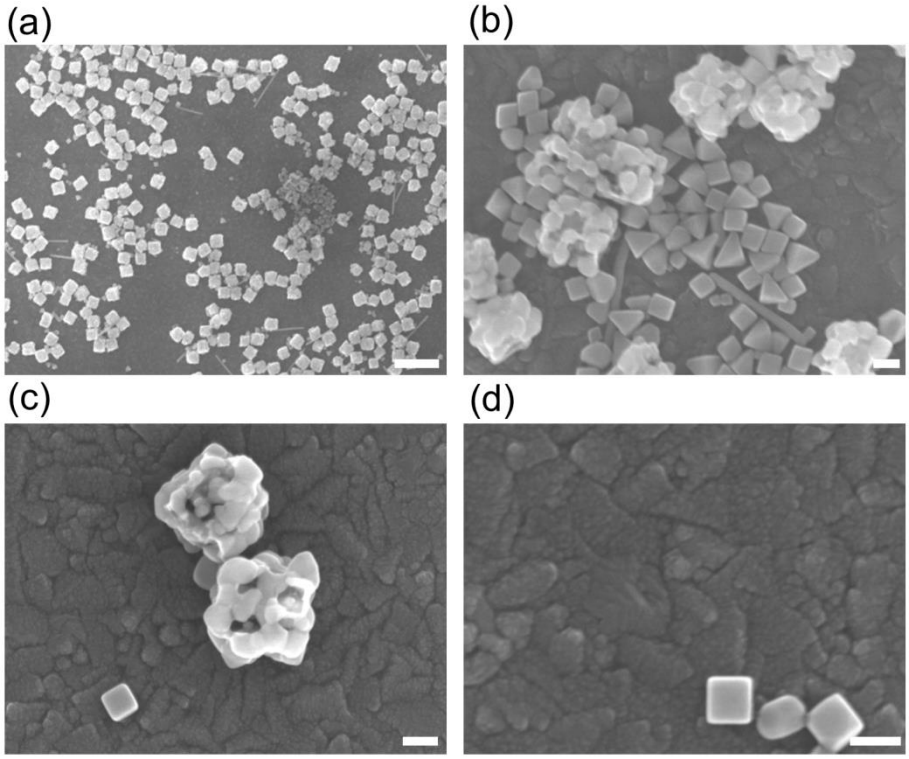

Figure 3-1. SEM images of AgNCs synthesized from $AgNO_3$. The scale bar is (a) 1 μm and (b,c,d) 100 nm.

Figure 3-1 shows the SEM images of AgNCs using $AgNO_3$ as the ingredients of Ag. Different from the expectations and the other reports[16, 24] in which uniform AgNCs were successfully synthesized, silver nanoparticles synthesized herein somewhat deviates from the cube shapes. The use of HCl has been reported to stabilize the reaction and realize the easy control of the shapes.[24] However, the results obtained herein (Figure 3-1) indicate that the synthetic reactions are still unstable and lead to bad reproducibility of AgNCs on the basis of $AgNO_3$. Seemingly, the nanoparticles look like cube shapes in Figure 3-1a. However, the magnified images (Figure 3-1b) show that the cube-like nanoparticles are rather pop-corn shapes in which several particles are aggregated (Figure 3-1c). In some parts, the AgNCs are also observed and keep cube shapes (Figure 3-1d). Overall, the portion of AgNCs is small.

Taguchi group reported that the shapes and the sizes of silver nanoparticles were controlled by the amount of oxygen flow during synthetic procedures.[25] Thus, it is implied that the synthetic procedures of silver nanoparticles based on $AgNO_3$ are

sensitive to the amount of oxygen during synthesis. Equations shown below are the expected reactions related to oxygen and moisture during reaction using HCl and $AgNO_3$ for the synthesis of AgNCs (eq. 3-1).[26]

$$HCl + AgNO_3 \rightarrow HNO_3 + AgCl \quad \text{(eq. 3-1-1)}$$

$$4HNO_3 + 3Ag \rightarrow 3AgNO_3 + NO + 2\,H_2O \quad \text{(eq. 3-1-2)}$$

$$2NO + O_2 \rightarrow 2NO_2 \quad \text{(eq. 3-1-3)}$$

$$3NO_2 + H_2O \rightarrow 2HNO_3 + NO \quad \text{(eq. 3-1-4)}$$

As shown, the oxygen and moisture are directly related to overall reaction.

Figure 3-2. The color of precursors during the synthetic procedure stirring at 140 °C by different time.

To confirm the sensitivity to atmosphere conditions, the experiment was done in which the vial cap was opened for 180 min after the whole injection of precursors (HCl, $AgNO_3$, PVP) (Figure 3-2). Color did not change during the cap opened even after 180 min, meaning that the exposure to O_2 impede the formation of AgNCs. After 180 min, the cap was closed and the color started to change as shown in Figure 3-3.

According to the recent report, with the existence of oxygen during reaction, the twinned seeds formed are reversibly removed again, which prevents the fast reaction of the AgNC formation. However, too fast reaction does not lead to formation of uniform AgNCs. From the results,[26] it is conjectured that the adequate amounts of oxygen and moistures are essential to precise control of AgNCs. However, precise control of moisture and oxygen is not easy. Thus, another method that is not sensitive to moisture and oxygen during reaction is favorable.

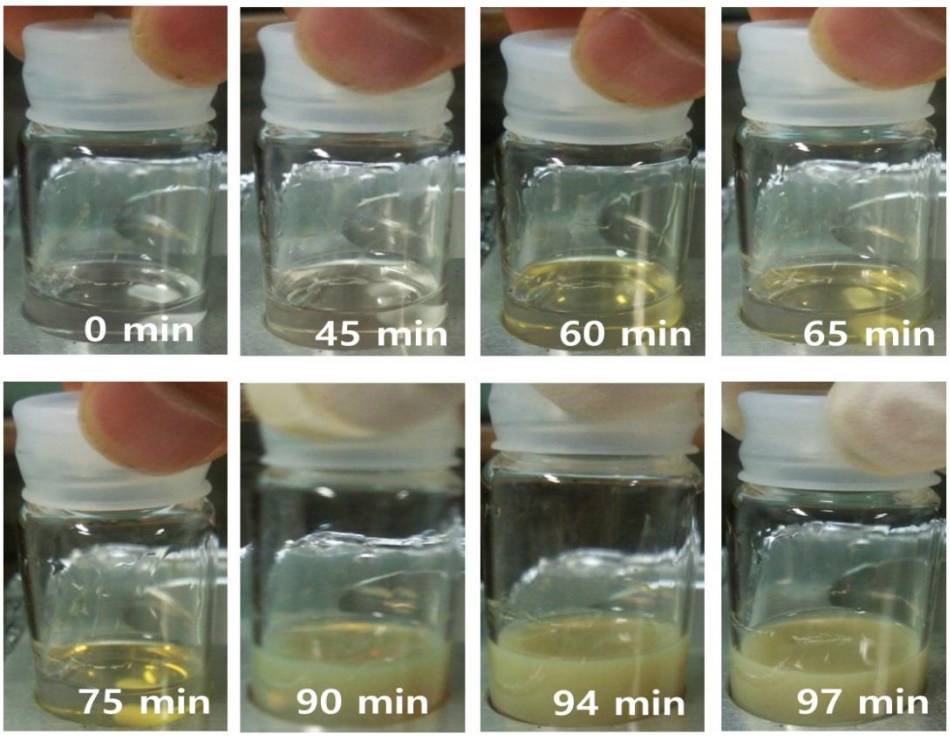

Figure 3-3. The color change of precursors after the cap was closed.

3-3-2 Synthesis using CF_3COOAg as precursor

Recently, a new synthetic method, which is relatively reproducible, was reported. By using CF_3COOAg instead of $AgNO_3$, decomposition of nitrate group in $AgNO_3$ could be avoided, leading to stable reaction because trifluoroacetate group is not reactive.[22]

The procedures were explained in experimental section in detail. The results of AgNCs are quite reproducible regardless of the existence of the cap, meaning that the oxygen does not seriously affect the reaction. However, the concentration of HCl and the amount of NaSH critically affect the final morphology of AgNCs.

Different from the experimental conditions reported elsewhere in which 3 mM of HCl and NaSH were used,[22] in the experiment herein, lower concentration of HCl and NaSH were used; either 3 mM of HCl and 1.5 mM of NaSH or 2mM of HCl and 3 mM of NaSH. Both of the conditions lead to uniform AgNCs while the slight different concentrations of HCl and NaSH beyond those ranges result in non-uniform and wire-like metal nanoparticles. The most difficult factor to control in this experiment is the amount of NaSH because extremely small amount of NaSH is used. Also, NaSH in EG is volatile so that the amount of NaSH gradually decreases by the time. For this reason, in the synthetic procedure, different amounts of 1.5 mM NaSH were used in different vials from 40 μL to 70μL.

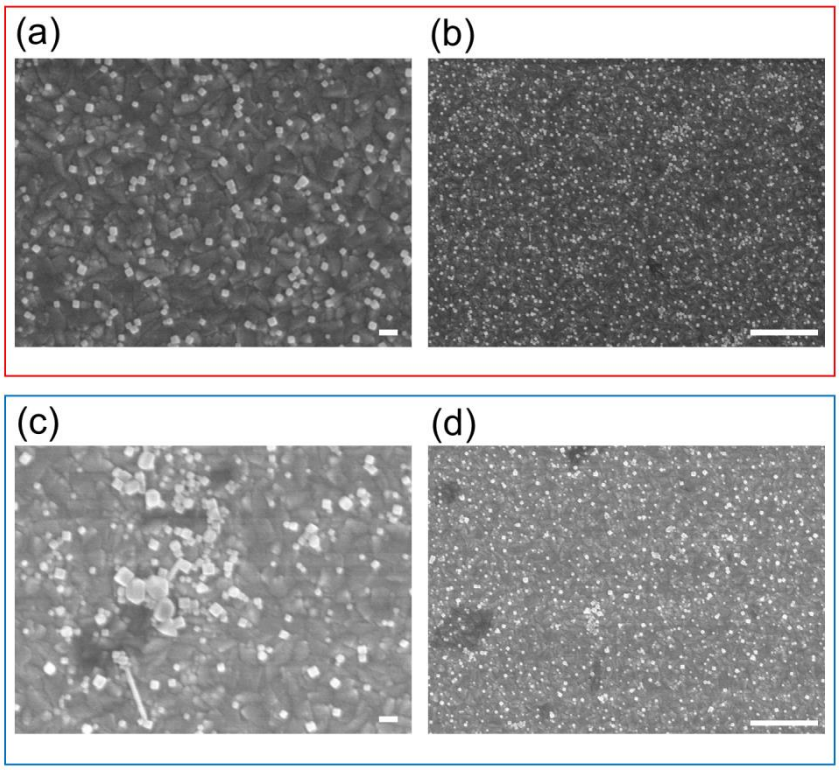

Figure 3-4. SEM images of AgNCs obtained by using (a,b) 50 μL and (c,d) 70μL of NaSH (1.5 mM). The scale bars are (a,c) 100 nm and (c,d) 1 μm.

Figure 3-4 shows the SEM images of AgNCs obtained by using 50 μL (Figure 3-4a,b) and 70μL (Figure 3-4c,d). Here, by using 50μL of NaSH, uniform and shape-controlled AgNCs were successfully synthesized (Figure 3-4 a,b). However, when 70μL of NaSH was used, the resultants are not uniform and not well-controlled as shown in Figure 3-4 c,d. It is noted that the optimum amounts of NaSH are different by the time and day due to the difficulty in controlling the concentration of NaSH precisely.

By changing the reaction time, the size of AgNCs is controlled. The relationship between the LSPR peak wavelength and the size of AgNCs is shown in Figure 3-5. The peak is red-shifted linearly with the sizes of AgNCs along with the increase in the half width.

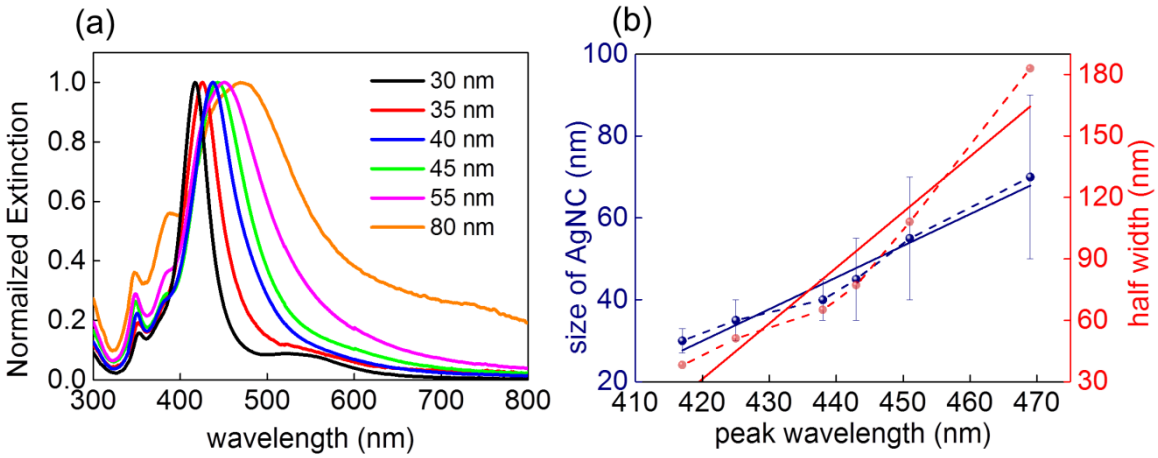

Figure 3-5. (a) Normalized extinction spectra of AgNCs of different sizes dispersed in EtOH. (b) Peak wavelength versus size of AgNC and half width.

3-4 Plasmonic properties

3-4-1 Film-coupled plasmons

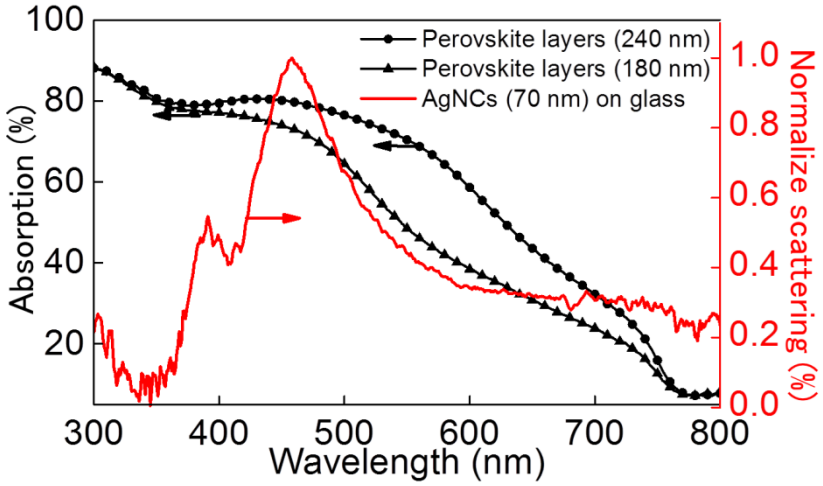

Figure 3-6. Absorption of 180 nm and 240 nm-thick perovskite layers on ITO/PEDOT:PSS substrates and the normalized scattering of 70 nm of AgNCs on glass.

It was reported that direct application of MNPs to PVSCs is hard to enhance the photocurrent despite MNPs have been widely used in OSCs.[10-12, 18] To enhance the photocurrents by plasmonic MNPs in PVSCs, the plasmonic peaks need to be located near the low absorption region of perovskite layers. As shown in Figure 3-6, the typical MNPs including AgNCs have plasmonic peaks at around 400-500 nm. The perovskite layers absorb light strongly under 500 nm even though the thickness is thin (~180 nm) (the black lines in Figure 3-6. Thus, the typical MNPs cannot significantly enhance

photocurrents in PVSCs because IQEs of PVSCs in those regions are already saturated. To largely shift the plasmonic peaks to the absorption edge of perovskite layers, the use of metal nanorods[27] or decreasing interparticle spacing[28] could be alternative as the plasmonic tunings are relatively viable in those cases.

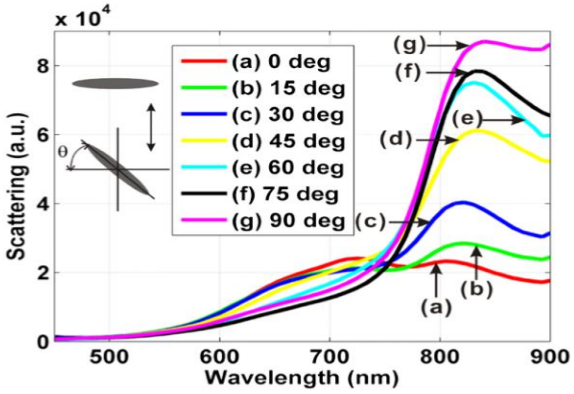

Figure 3-7. Scattering spectra of gold nanorod with various orientations. Reprinted with permission from Ref. 28. Copyright 2013 SPIE.

However, those approaches have a critical problem, which is polarization-dependence. The experimental data of the dependence on the polarization angle for gold nanorod are depicted in Figure 3-7. As the polarization angle of incident light is random in usual applications, the devices should be polarization-independent. The film coupled plasmons, in which the metal nanoparticles are coupled with a metal film with the existence of a thin insulator between them, can take advantage of large shifting of plasmonic peaks with independence of polarization angle.[20, 21, 29]

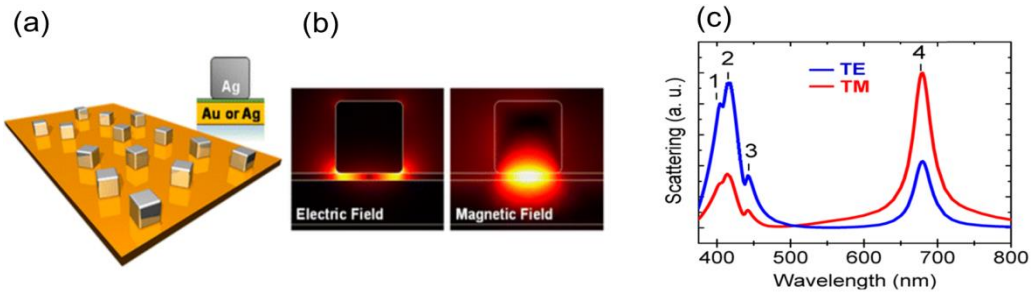

Figure 3-8 (a) Structure, (b) electric and magnetic fields and (c) plasmonic scattering spectra of film-coupled plasmons. Reprinted with permission from Ref. 30. Copyright 2013 American Chemical Society.

3-4-2 Electrode-coupled plasmons: simulation

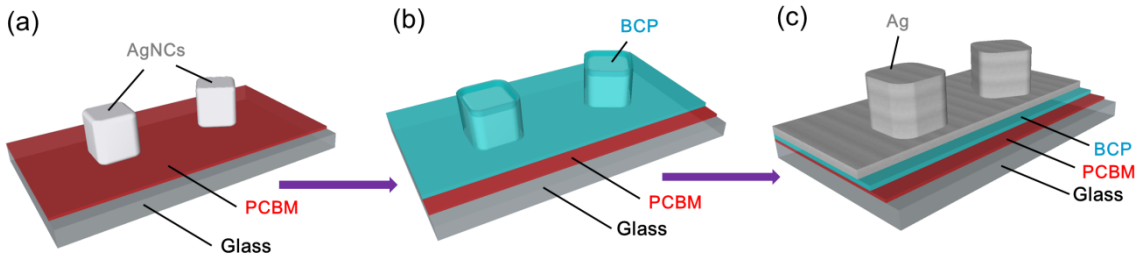

Figure 3-9. Procedure to realize the structure for electrode-coupled plasmons. (a) AgNCs deposited on a glass/PCBM substrate. (b) A BCP layer deposited on the substrate as shown in (a). (c) A silver electrode deposited on the substrates as shown in (b).

Typical structures that exhibit film-coupled plasmons consist of metal nanoparticles deposited on metal and thin insulator films as depicted in Figure 3-8a. The plasmon strongly occurs at the interface shown in Figure 3-8b. The plasmonic peaks from these couplings have broadly separated features as shown in Figure 3-8c.[29]

In a similar manner to the film-coupled plasmons, electrode-coupled plasmons are proposed here, which are eventually applied into PVSCs. A structure that exhibits electrode-coupled plasmons is depicted in Figure 3-9. Considering the compatibility with PVSCs, the PCBM and BCP layers were used, which have the similar function to the insulating layers in the structures for film-coupled plasmons. First, AgNCs are deposited on a glass/PCBM substrate (Figure 3-9a). Then a thin BCP layer is deposited (Figure 3-9b) followed by coating a silver electrode (Figure 3-9c). Since the metal film here is used as an electrode, the plasmons generated at the structure in Figure 3-9c is named electrode-coupled plasmons (ECPs).

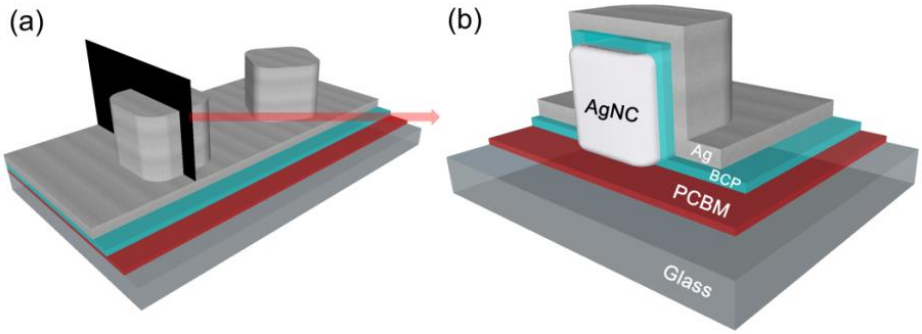

Figure 3-10. (a) Structure for ECPs. (b) Cross-section image for (a).

In Figure 3-10, a cross-section image of the structure for ECPs is shown. Similarly to the film-coupled plasmons (Figure 3-8a), AgNC can be coupled with Ag electrode through the thin BCP between them. However, for the ECPs, five faces of AgNCs are coupled with the metal electrode while only one face (the bottom of AgNC) is coupled in film-coupled plasmons.

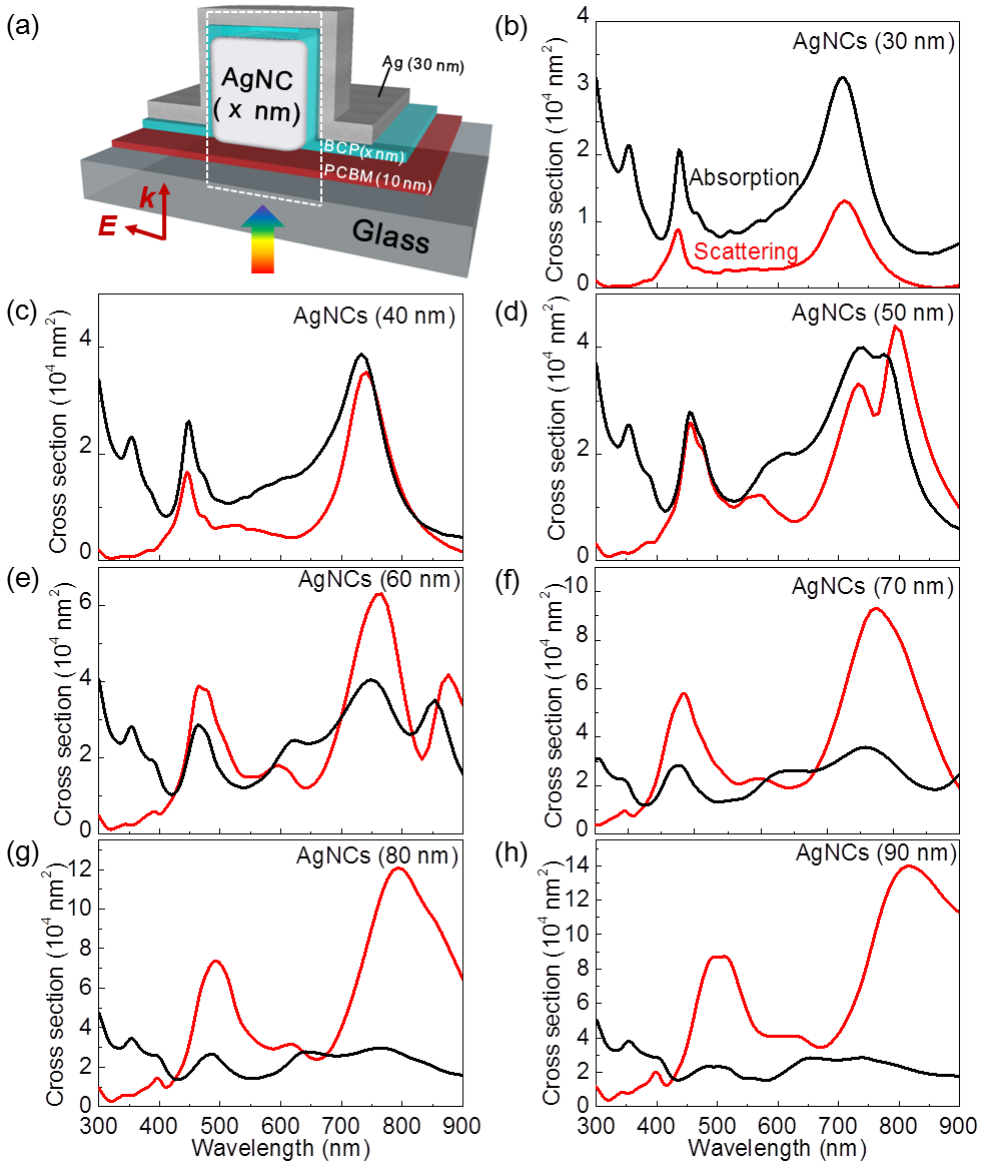

Figure 3-11 (a) The structural model used for the FDTD simulation. (b-h) Plasmonic absorption and scattering spectra of the model in (a) with (b) 30 nm, (c) 40 nm, (d) 50 nm, (e) 60 nm, (f) 70 nm, (g) 80 nm and (h) 90 nm AgNC on glass/PCBM (10 nm). The structure is coated with a silver electrode (30 nm).

Figure 3-11 shows the plasmonic absorption and scattering spectra of ECPs calculated from FDTD simulation by changing the sizes of AgNCs from 30 nm to 90 nm. It is noted that the thicknesses of PCBM, BCP and Ag are 10 nm, 10 nm and 30 nm, respectively (Figure 3-11a). Regardless of the sizes of AgNCs, the plasmonic scattering of ECPs calculated from FDTD simulation shows at least broadly separated peaks, which are accordance with the peaks observed in film-coupled plasmons. Thus, it is considered that the basic mechanism of ECPs is similar to the film-coupled plasmons. When the size of AgNC is 30 nm (Figure 3-11b), the plasmonic absorption tends to be higher than scattering in entire range. The scattering becomes higher when the size of AgNC is larger (Figure 3-11c). The scattering starts to be higher when the size of AgNC is over 50 nm (Figure 3-11d,e) and the scattering is dominant compared to absorption for AgNC $\geqq$ 70 nm (Figure 3-11f,g,h). The peaks in a long wavelength range are red-shifted slightly with larger sizes of AgNCs. The overall amount of plasmonic absorption does not increase largely depending on the sizes of AgNCs unlike plasmonic scattering.

To quantify the amount of scattering and absorption, integrated value was calculated based on eq. 3-2 and the results are shown in Figure 3-12.

$$total\ scattering = \int_{350\ nm}^{800\ nm} scattering\ (\lambda) d\,\lambda \quad \text{(eq. 3-2-1)}$$

$$total\ absorption = \int_{350\ nm}^{800\ nm} absorption\ (\lambda) d\,\lambda \quad \text{(eq. 3-2-1)}$$

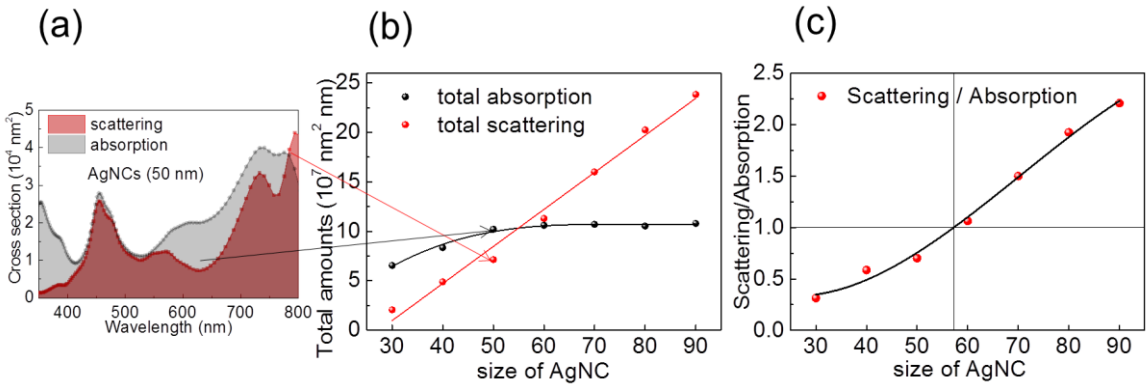

Figure 3-12. (a) Integration of scattering and absorption for AgNC (50 nm) for ECPs. (b) Total scattering and absorption and (c) total scattering divided by total absorption with different sizes of AgNCs.

It is noted that the wavelengths range from 350 nm to 800 nm was chosen for the integration because it is the typical range of perovskite absorption based on $CH_3NH_3PbI_3$. Figure 3-12a shows an example of the integration of scattering and absorption for the ECPs with 50 nm of AgNC. The values obtained by the integration for different sizes of AgNCs from 30 nm to 90 nm are shown in Figure 3-12b. The total absorption tends to increase from 30 nm to 50 nm of AgNCs and becomes saturated beyond AgNC > 50 nm. However, the total scattering linearly increases with the size of AgNCs. The plasmonic absorption can cause light loss in PVSCs because the light supposed to be absorbed in the active layer may be absorbed by MNPs. Actually, the larger scattering compared to absorption is advantageous for the enhancement of photocurrents in PVSCs by taking advantages of near field and far field scattering.[17-19] In this regard, the values of scattering divided by absorptions (S/A) are calculated based on Figure 3-12b and shown in Figure 3-12c. In the range of AgNC < 60 nm, S/A is less than 1, implying that the absorption is larger than scattering. The scatterings become larger than absorptions when AgNC is larger than 60 nm, recording S/A > 1. Thus, the ECPs with AgNCs which are larger than 60 nm are considered to be advantageous for the application to PVSCs.

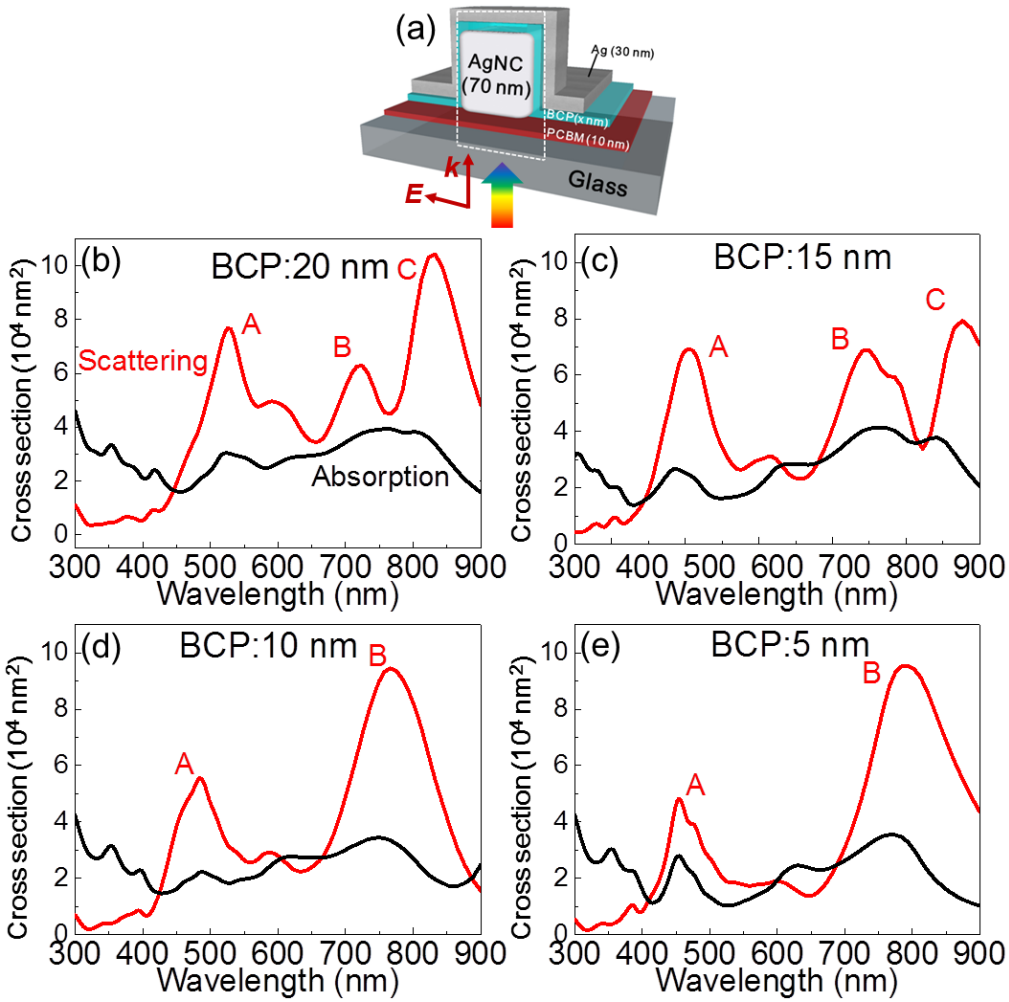

Figure 3-13. (a) The structural model used for the FDTD simulation. (b-e) Plasmonic absorption and scattering spectra of the model in (a) with (b) 20 nm, (c) 15 nm, (d) 10 nm and (e) 5 nm of BCP on glass/PCBM (10 nm)/AgNC (70 nm). The structure is coated with Ag electrode (30 nm).

The thickness dependence of BCP is also examined (Figure 3-13). Here, 70 nm of AgNC was used for the simulation as 70 nm is considered to be ideal for the application due to the results from Figure 3-12c and experimental accessibility because too large sizes of AgNC are difficult to be synthesized.

Unlike typical fim-coupled plasmons in which the two main peaks are absorbed, the spectra of ECPs are composed of three main peaks (A,B,C) when the BCP is thicker (15-20 nm) (Figure 3-13 b,c). The thin layers of BCP broaden the peak splitting as observed and peak C is no longer observed in the wavelength range examined (300 nm to 900 nm) because the peak C is more red-shifted (Figure 3-13d,e). The dependence of peak splitting on the thickness of BCP resembles to the typical film-coupled plasmons, implying that the splitting herein stems from ECPs.

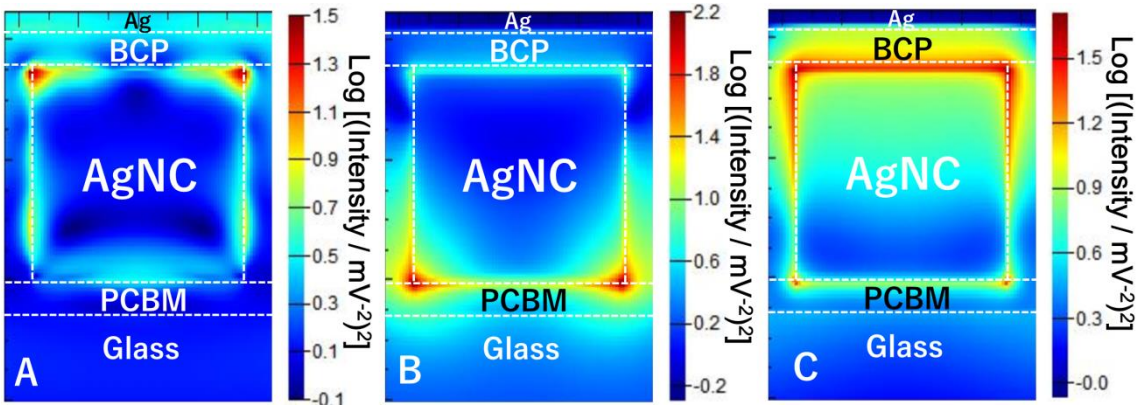

Figure 3-14. The electric field distributions at peak A, B and C of ECPs when the 70 nm of AgNC is placed on glass/PCBM (10 nm) and coated with 15 nm of BCP and 30 nm of Ag in the position of white dotted line in Figure 3-13a.

To scrutinize the impact of plasmonic peaks, electric field distributions were examined for each peak of A, B and C in Figure 3-14. In Figure 3-14, electric fields of peaks A, B and C of ECPs with 15 nm of BCP calculated by FDTD are presented. The intensity and the position of peaks A, B and C shown in Figure 3-14 have similar trends regardless of the thickness of BCP. Thus the only 15 nm of BCP case is shown. In the peak A and C, the electric fields are confined at the distal face of AgNC, which is far from the PCBM layers. On the other hand, the electric fields are densely distributed on the proximal face of AgNC for the peak B. Considering the near field optical antenna effect, electric fields on the proximal face of AgNC are advantageous because it is near the PCBM-glass interface, which is the PCBM-perovskite interface in actual PVSCs. Also, positioning peak B near 800 nm might be effective for the application to PVSCs because the absorption edge of perovskite layers is at 800 nm. Thus, 10 nm of BCP and 70 nm of AgNC are considered to be ideal. The penetration of near field through the PCBM layer is important for the enhancement of PVSCs. In this respect, the electric field distributions of ECPs with 10 nm of BCP and 70 nm of AgNC at the PCBM-glass interface are also calculated (Figure 3-15).

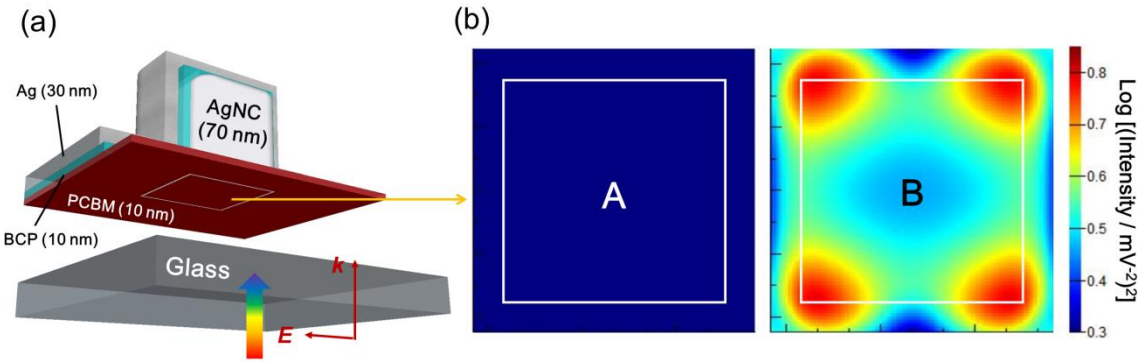

Figure 3-15. (a) The position at which electric field distribution of ECPs is calculated. (b) Electric field distributions at peak A and B in Figure 3-13d at the position marked as white square box in (a) (10 nm below the contact area of AgNC on PCBM).

The strong electric fields at the glass-PCBM interface are observed for peak B, implying that the electric fields can penetrate 10 nm-thick PCBM layer, affecting the glass. This implies that the near-field antenna is effective for the perovskite layers in an actual cell. For peak A, electric fields are weak at the interface. The weak intensity observed for peak A is attributed to the electric fields which are confined at distal face of AgNC, which is far from the glass-PCBM interface. Overall, peak B of ECPs would enhance the photocurrents of PVSCs, especially at the absorption edge of perovskite layers.

So far, the plasmonic characteristics of ECPs have been presented. As mentioned above, the AgNCs for ECPs herein are coupled with 5 faces different from typical film-coupled plasmons in which only one face of AgNC is coupled.

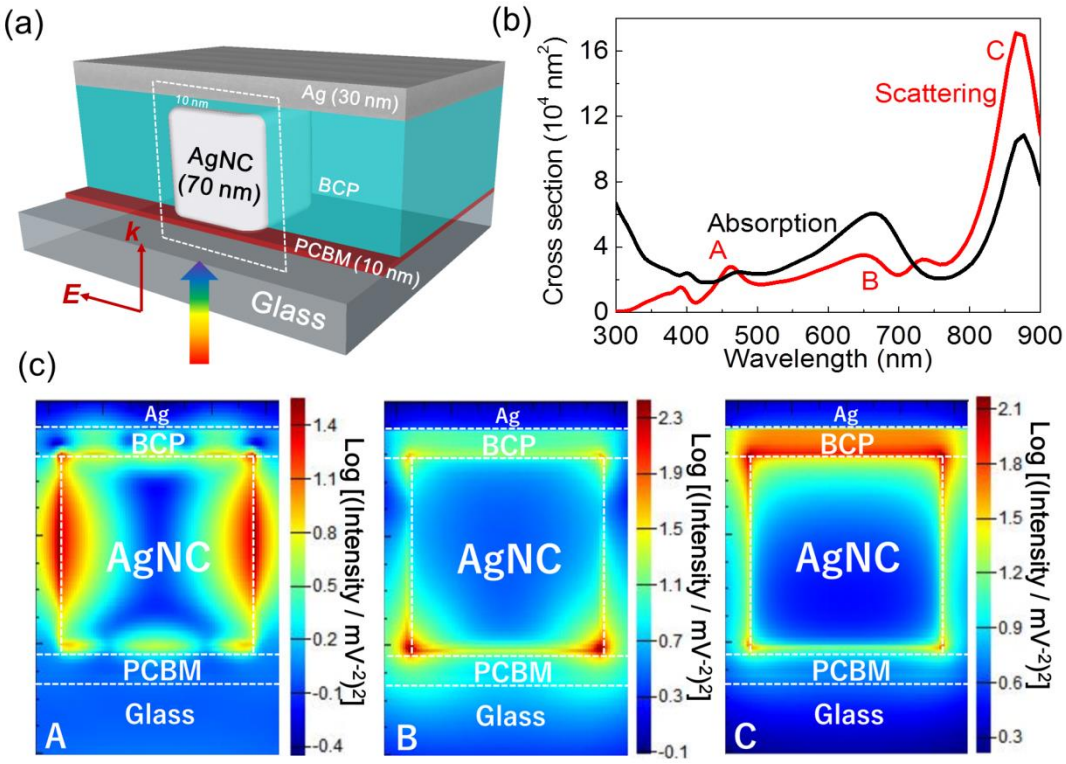

Figure 3-16. (a) The structure of ECPs in which only one face of AgNC is coupled with Ag (the gap between AgNC and Ag is 10 nm). (b) The plasmonic absorption and scattering spectra and (c) electric field distribution of ECPs based on the structure in (a).; The position of electric field distribution is the white dotted square in (a).

For comparison, the ECPs in which only one face of AgNC is coupled with the Ag electrode were also studied. The Figure 3-16a shows the ECPs model structure in which only one face of AgNC is encountered with Ag electrode. From FDTD calculation based on the model in Figure 3-16a, the plasmonic absorption and scattering spectra were obtained and shown in Figure 3-16b. Similarly to the ECPs in which five faces of AgNC are coupled with the Ag electrode, the three plasmonic scattering peaks A, B and C were observed (Figure 3-16b). The intensity of peak B is low compared to peak A. The electric field distributions at the position marked as the white dotted square were calculated and shown in Figure 3-16c. The location of electric fields of peak B and C are similar to the ECPs based on the structure in Figure 3-13a, showing that the electric fields are distributed at the proximal face and distal face for the peak B and C, respectively. The electric fields at peak A are distributed on the lateral sides of AgNC. Conclusively, the ECPs in which only one face of AgNC is coupled with Ag have lower scattering intensity at peak B, which is not advantageous for the enhancement of PVSCs due to low far field scattering.

3-4-3 Electrode-coupled plasmons: experimental results

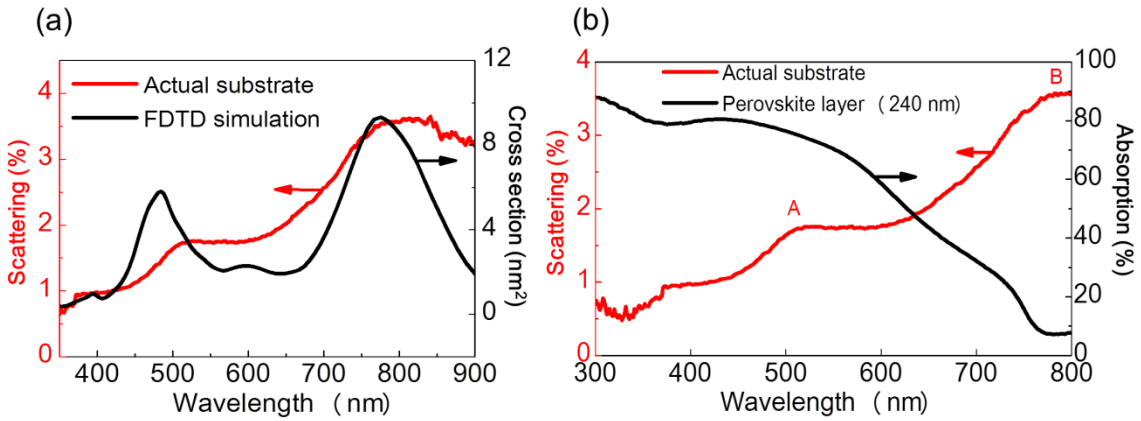

Figure 3-17. (a) Scattering spectrum of actual substrates consisting of glass/PCBM (10 nm)/AgNCs (70 nm)/BCP (10 nm)/Ag (100 nm) and that obtained by FDTD in Figure 3-13d. (b) The scattering spectrum of the actual substrate in (a) and the absorption of a 240 nm-thick perovskite layer on a ITO/PEDOT:PSS substrate.

Based on the results from FDTD, the actual substrates exhibiting ECPs were fabricated. It is noted that 100 nm Ag electrode was used for the actual substrates. The actual substrate (the detail structure is described in the caption of Figure 3-17a) has broadly separated two peaks (red line in Figure 3-17a), which are in the similar positions of peaks obtained by FDTD simulation of the structure for ECPs (black line in Figure 3-17a). Thus, it is speculated that those scattering peaks of actual substrates are ECPs. The peak B is positioned at the absorption edge of perovskite layers (Figure 3-17b) which is in accordance with the FDTD simulation. This suggests that the actual substrates for ECPs would be effective for the application to PVSCs.

3-5 PVSCs with ECPs

3-5-1 Deposition of AgNCs on PCBM layers

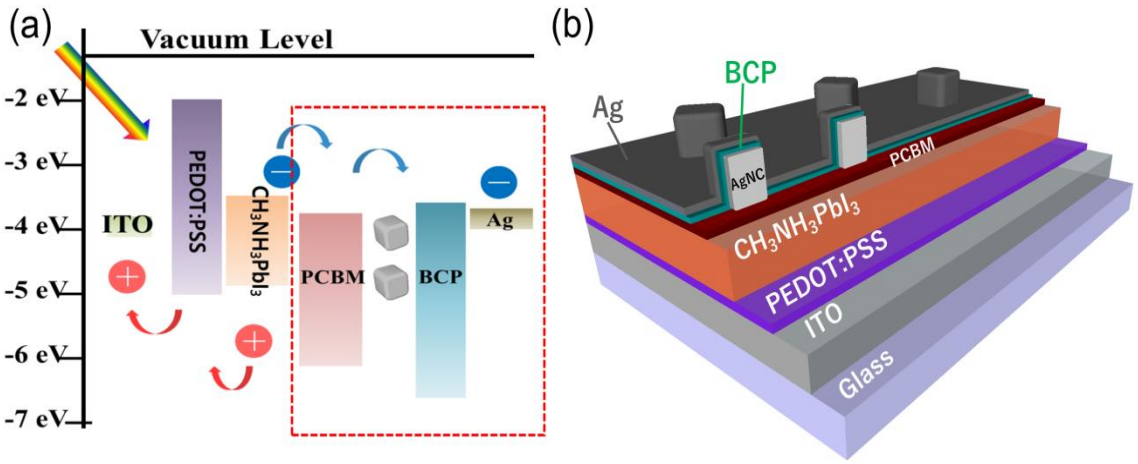

Figure 3-18. (a) Energy diagram and (b) the structure of PVSCs based on ECPs.

Here, the structure for ECPs was actually applied to PVSCs. The energy diagram and the structure of PVSCs based on ECPs are shown in Figure 3-18. As shown in Figure 3-18b, AgNCs are deposited on the PCBM layer followed by evaporation of BCP and silver. The red square in Figure 3-18a resembles the model of ECPs used for FDTD simulation depicted in Figure 3-11a.

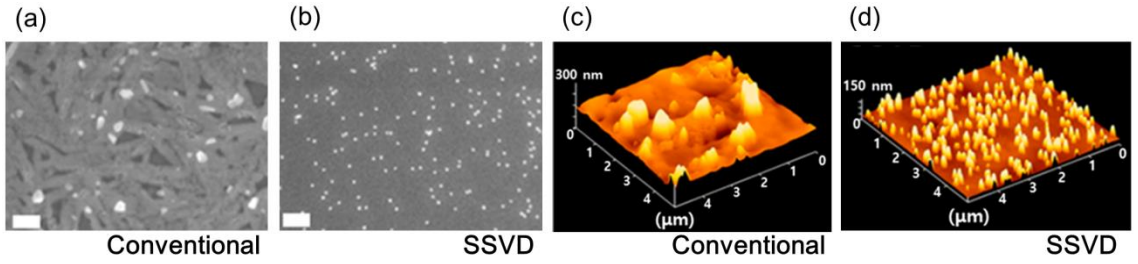

Figure 3-19. (a, b) SEM and (c, d) AFM images of AgNCs deposited on an ITO/PEDOT:PSS/perovskite/PCBM substrate with the perovskite layer processed by (a, c) the conventional and (b, d) the SSVD methods. (a, b) Scale bar is 1 μm.

Unlike deposition of AgNCs by spincoating onto glass/PCBM layers, attaching AgNCs onto ITO/PEDOT:PSS/$CH_3NH_3PbI_3$/PCBM is difficult to control by spincoating. Figure 3-19 shows AgNCs on ITO/PEDOT:PSS/$CH_3NH_3PbI_3$/PCBM in which perovskite layers were processed either by the short spinning and vacuum drying (SSVD) and conventional methods. The nanoparticles on the PCBM layers seem to be aggregated as

the sizes are large over 200 nm when the perovskite layers are processed by the conventional method (Figure 3-19a,c), implying that AgNCs are not uniformly deposited on the surface. When the perovskite layers are processed by SSVD, AgNCs on the PCBM layer are uniformly distributed as confirmed in Figure 3-19b,d. In Chapter 2, ultrasmooth perovskite films were obtained by SSVD. The ultrasmooth and flat perovskite films by SSVD lead to the smooth PCBM layers. Thus the AgNCs are well distributed during spincoating on the smooth PCBM layers. However, the PCBM layers become rough on the rough perovskite films processed by the conventional method, showing the pin-holes of PCBM in Figure 3-19a,c. The AgNCs are easily trapped in the rough PCBM and aggregated, suggesting that SSVD is appropriate for application of ECPs to PVSCs. Thus, the all PVSCs with ECPs dealt with here are based on the perovskite layers processed by SSVD.

3-5-2 PVSCs with 240-nm-thick perovskite layers

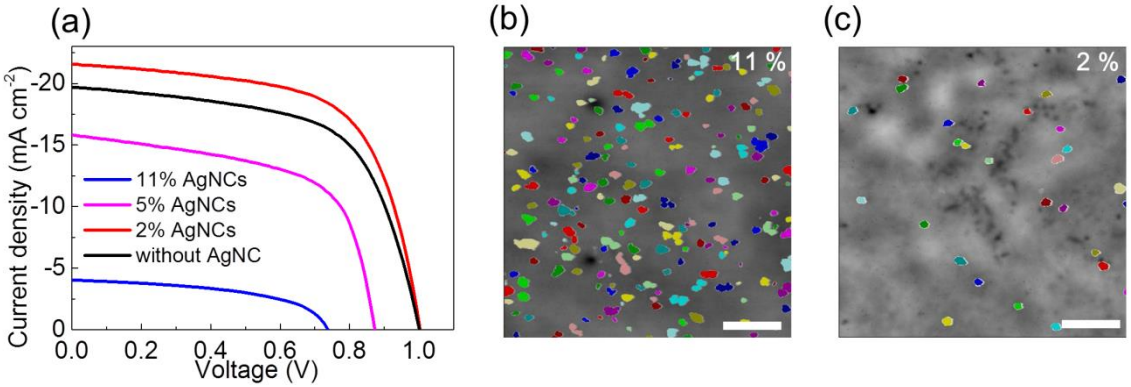

Figure 3-20. (a) *J-V* characteristics of PVSCs with ECPs in which different amounts of AgNCs were loaded on PCBM. AFM images of AgNCs which cover (b) 11% and (c) 2% of PCBM surface on ITO/PEDOT:PSS/$CH_3NH_3PbI_3$. In all cells, a 240 nm-thick peovskite layer was used. Scale bar is 1 μm.

PVSCs with ECPs were fabricated with different loading amounts of AgNCs on PCBM, *J-V* performances of which are shown in Figure 3-20. It is noted that the 240 nm-thick perovskite layers were used for the PVSCs here. The percentage values in the legend of Figure 3-20a indicate the surface coverage of AgNCs on the PCBM layer. Too much loading of AgNCs degrades the overall performances of PVSCs, recording the PCEs of 7.89 ± 1.47% and 1.58 ± 0.19% for 5% and 11% coverages of AgNCs (pink and blue lines). It is considered that a large amount of AgNCs may work as trap sites. Thus, core-shell structures in which insulators such as SiO_2 is coated on the surface of

the nanoparticles are used in some cases.[30, 31] Also, large amounts of AgNCs lead to aggregation of particles during spincoating as shown in AFM images in Figure 3-20b, thereby ECPs do not properly work. The above-mentioned problems regarding trap sites and aggregation for large amounts of AgNC result in short pathway or preventing light absorption into active layer, thereby low J_{sc} and V_{oc}.

Loading 2% of AgNCs onto PCBM leads to the improved performances compared to the PVSCs without AgNC. In Figure 3-19c, AgNCs are uniformly coated without aggregation, suggesting that the structure for ECPs are well constructed. The PCE of PVSCs with 2% AgNCs records 13.3 ± 1.12%, while that of the PVSCs without AgNCs records 11.86 ± 0.88%. The enhanced performances are mainly caused by the 10% increase in J_{sc} from 19.5 ± 0.46 mA cm^{-2} to 21.4 ± 0.45 mA cm^{-2}. Other parameters such as FF and V_{oc} remain almost unchanged, implying that small amount of AgNCs (~2%) rarely affect the charge transfer efficiency. The parameters of the performances of PVSCs are shown in Table 3-1 in detail.

Table 3-1. Performances of the PVSCs with and without AgNCs under AM 1.5G light irradiation[a]

perovskite layer thickness (nm)	coverage of AgNCs (%)	J_{sc} (mA cm^{-2})	V_{oc} (V)	FF	PCE (%)
240	11	4.14 ± 0.35	0.73 ± 0.03	0.51 ± 0.02	1.58 ± 0.19
	5	15.51 ± 0.31	0.87 ± 0.02	0.58 ± 0.04	7.89 ± 1.47
	2	21.4 ± 0.45	1.0 ± 0.02	0.62 ± 0.04	13.3 ± 1.12
	0	19.5 ± 0.46	1.0 ± 0.01	0.61 ± 0.05	11.86 ± 0.88
180	2	17.1 ± 0.09	1.02 ± 0.02	0.62 ± 0.03	11.08 ± 0.43
	0	15.2 ± 0.05	1.03 ± 0.01	0.61 ± 0.02	9.67 ± 0.36

[a]All the values (means ± standard deviation) were evaluated for at least six cells. The light intensity was 100 mW cm^{-2}. The voltage sweep is forward direction from -0.05V to 1.1V with the sweeping rate of 100 mV s^{-1}.

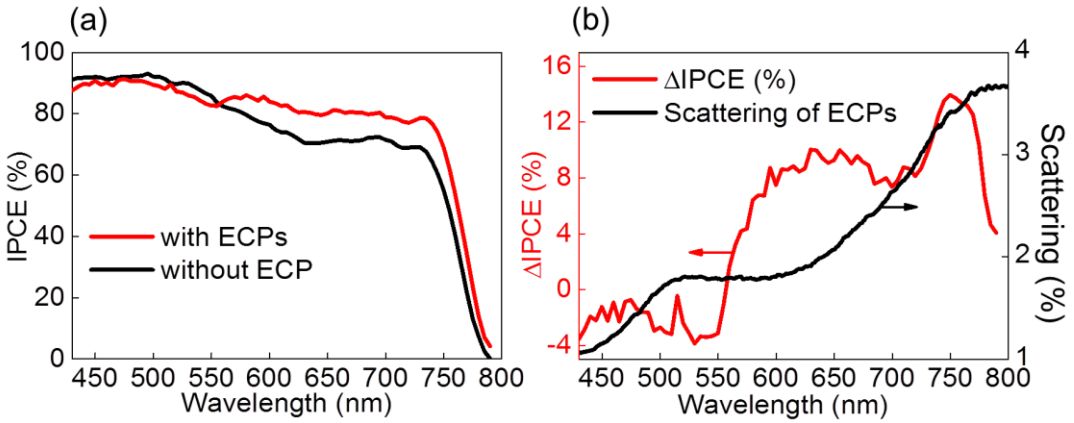

Figure 3-21. (a) IPCE spectra of the PVSCs with ECPs in which 2% AgNCs are loaded on PCBM and without ECP. (b) △IPCE spectrum of the PVSCs and scattering spectrum of a glass/PCBM (10 nm)/AgNCs (70 nm)/ BCP (10 nm)/Ag substrate.

For further insights regarding the improved photocurrents by ECPs, incident photon-to-current conversion efficiencies (IPCEs) were also measured and compared (Figure 3-21). Slight decrease in photocurrents for the PVSCs with ECPs in short wavelength range (< 550 nm) was observed compared to the PVSCs without ECPs (Figure 3-21a). In the wavelength range > 550 nm, the overall IPCE is larger for the PVSCs with ECPs, causing the increase in J_{sc}. ΔIPCE is also calculated based on eq. 3-3.

$$\Delta\text{IPCE} = \textit{IPCE of PVSCs with ECPs} - \textit{IPCE of PVSCs without ECPs} \qquad \text{(eq. 3-3)}$$

In Figure 3-21b, the value of ΔIPCE turns from negative to positive at 550 nm, meaning that the IPCE of PVSCs with ECPs starts to be larger than the cells without ECP. ΔIPCE reaches the maximum value at 750 nm, which is near the absorption edge of perovskite layers. The black line indicates the plasmonic scattering spectrum of an actual substrate with ECPs, which was previously presented in Figure 3-17b. The overall shapes of plasmonic scattering spectrum of ECPs resemble ΔIPCE spectrum near the absorption edge of perovskite layers. This implies that the improved photocurrents may stem from the ECPs. As mentioned above, the slight decrease in IPCE in the short wavelength range (< 550 nm) is observed despite the plasmonic scattering peak at 510 nm. This would be explained by extremely low intensity of near field at the PCBM-perovskite interface, assessed from the FDTD simulation in Figure 3-15 because the electric fields are mostly confined at the distal face of AgNC in the short wavelength range.

3-5-3 PVSCs with 180-nm-thick perovskite layers

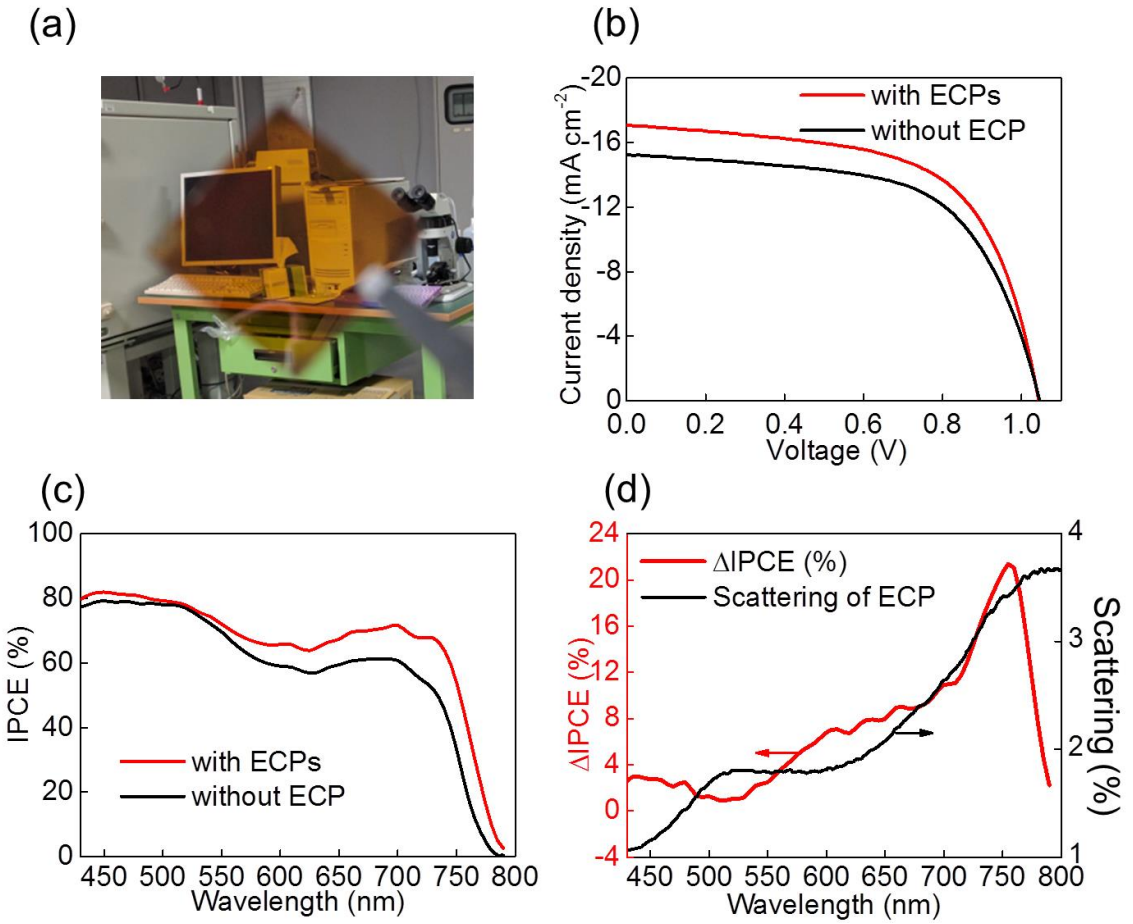

Figure 3-22. (a) Substrate consisting of ITO/PEDOT:PSS/$CH_3NH_3PbI_3$ (180 nm)/PCBM (10 nm)/AgNCs (2% coverage). (b) *J-V* characteristics and (c) IPCE spectra of PVSCs with ECPs and without ECP in which 180 nm-thick perovskite layers were used. (d) △IPCE spectrum of the PVSCs and scattering spectrum of a glass/PCBM (10 nm)/AgNCs (70 nm)/ BCP (10 nm)/Ag substrate.

Previously, it was mentioned that the improvement of photocurrents from PVSCs by LSPR is difficult because perovskite layers have high absorption coefficient.[13, 14] The improvement of PVSCs by LSPR might be more effective if the perovskite layers are thin due to the low light absorption. In this respect, the PVSCs with ECPs in which 180 nm-thick perovskite layers were used were also fabricated and examined. Because of thinner perovskite layers (180 nm), the substrates still have good visual transparency after coating AgNCs on ITO/PEDOT:PSS/perovskite/PCBM substrates (Figure3-22a). Figure 3-22b depicts *J-V* characteristics of PVSCs (180 nm-thick perovskite layers)

with ECPs. The PCE of PVSCs with ECPs is higher, recording 11.08 ± 0.43% compared to that of PVSCs without ECPs recording the PCE of 9.67 ± 0.36%. In a similar manner to PVSCs with thick perovskite layers, the enhanced PCEs are mainly caused by the increase in photocurrents. The J_{sc} value of PVSCs with ECPs is 17.1 ± 0.09 mA cm^{-2} and that of PVSCs without ECPs is 15.2 ± 0.05 mA cm^{-2}, keeping similar V_{oc} and FF values regardless of ECPs (parameters are shown in Table 3-1 in detail). In IPCE data (Figure 3-22c), the increase in photocurrents in a long wavelength range (>550 nm) is obvious, which is accordance with PVSCs with ECPs in which thick perovskite layers were used. Further, there is a slight increase in photocurrents even in a short wavelength range (> 550 nm) while the IPCE decreases for the thick cells with ECPs. The shape of ΔIPCE spectrum is similar to the scattering curve of ECPs (Figure 3-22d), showing high value near the absorption edge of perovskite layers. Therefore, the increase in photocurrents stem from ECPs and the increment is more obvious for the thin perovskite layers.

3-5-4 Hysteresis effects

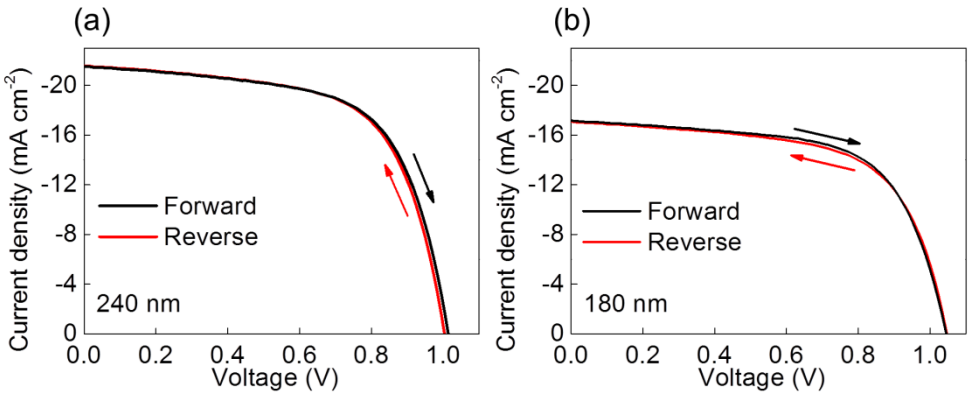

Figure 3-23. *J-V* characteristics of PVSCs containing ECPs with (a) 240 nm and (b) 180 nm-thick perovskite layers with forward and reverse sweep. The sweeping rate is 100 mV s^{-1}.

Hysteresis is one of the main problems for PVSCs because it may lead to overestimation or underestimation of the performances.[32] In chapter 2, it was proved that SSVD leads to hysteresis-free PVSCs by smoothing the surface of perovskite layers. Although PVSCs with ECPs developed here are based on the perovskite layers processed by SSVD, the addition of AgNCs may result in hysteresis because nanoparticles may work as impurities that affect the carrier migration negatively.[33]

Thus, the *J-V* curves for both forward and reverse sweep were measured for the both

PVSCs containing the structure for ECPs with 180 nm and 240 nm-thick perovskite layers and shown in Figure 3-23. Both PVSCs with 240 nm and 180 nm-thick perovskite layers do not have hysteresis, showing similar curves regardless of sweeping direction even when 2% of AgNCs are coated on PCBM. Thus, the improved performances of PVSCs using ECPs are reliable.

3-5-5 Thick perovskite layers using 50 wt% of precursor

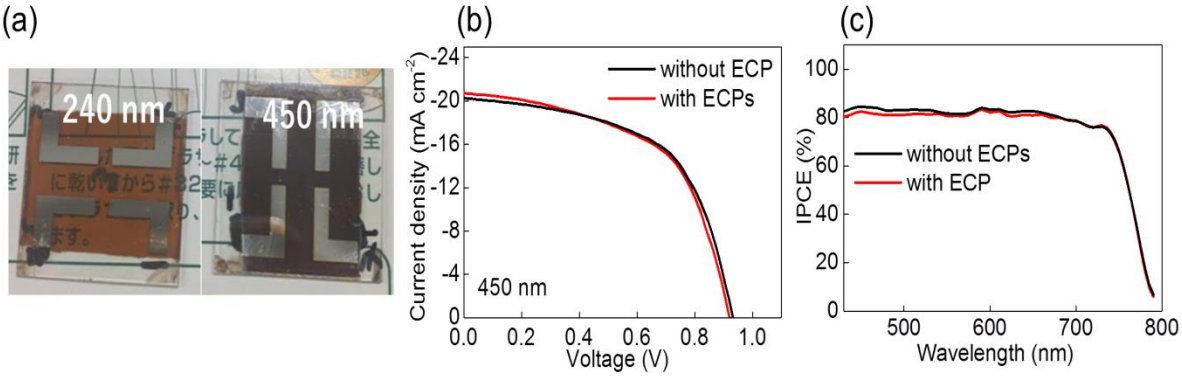

Figure 3-24. (a) PVSCs with ECPs in which 240-nm and 450-nm-thick perovskite layers were used. (b) *J-V* characteristics and (c) IPCEs of PVSCs with 2% AgNCs and without AgNC in which 450 nm-thick perovskite layers were used.

Enhancement of photocurrents by ECPs is more effective for PVSCs with thin perovskite layers. In this regard, it is expected that the plasmonic enhancement would not be obvious for PVSCs with extremely thick perovskite layers. Thus the PVSCs with ECPs were fabricated by using 450-nm-thick perovskite layers. PVSCs based on ECPs with 450-nm-thick perovskite layers have dense color compared to the PVSCs with 240-nm-thick perovskite layers (Figure 3-24a) because of the strong light absorption. In *J-V* characteristics, the overall performances of PVSCs with 450-nm-thick perovskite layers do not show enhancements by AgNCs, recording similar performances regardless of AgNCs (Figure 3-24b). No obvious photocurrent enhancements are observed from IPCE (Figure 3-24c).

It is considered that the AgNCs in PVSCs with extremely thick perovskite layers would not function as light enhancers because the majority of light was already absorbed in active layers before reaching AgNCs. Also, there is possibility that the AgNCs were not properly coated. The thick perovskite layers tend to have rough surfaces compared to the thin perovskite layers, thereby rough PCBM. As described in 3-5-1, the loading condition of AgNCs on PCBM is largely affected by the roughness of

PCBM. The rough PCBM surface caused by the thick perovskite layers would lead to non-uniform AgNCs. Thus, the ECPs were not properly realized. Further examination regarding the surface condition and optical properties needs to be done to enhance the performances of PVSCs with thick perovskite layers.

3-6 Conclusions

By using plasmon coupling between AgNCs and a Ag electrode on the basis of ECPs, performances of PVSCs were improved. The photocurrents were enhanced at around the absorption edge of the perovskite layers by the plasmonic near-field effect and far-field scattering effect of ECPs. PVSCs with thin perovskite layers are more efficient to increase their photocurrents as a large amount of light is introduced into the cell for being utilized by ECPs. It is expected that ECPs are not only used for PVSCs but also for many other photovoltaic systems, suggesting that the present technique based on ECPs can be a promising approach to solar cells.

3-7 References

1. Q. Chen, H. Zhou, Z. Hong, S. Luo, H.-S. Duan, H.-H. Wang, Y. Liu, G. Li and Y. Yang, *J. Am. Chem. Soc.*, 2013, **136**, 622-625.
2. J. You, Y. Yang, Z. Hong, T.-B. Song, L. Meng, Y. Liu, C. Jiang, H. Zhou, W.-H. Chang and G. Li, *Appl. Phys. Lett.*, 2014, **105**, 183902.
3. X. Li, D. Bi, C. Yi, J.-D. Décoppet, J. Luo, S. M. Zakeeruddin, A. Hagfeldt and M. Grätzel, *Science*, 2016, **353**, 58-62.
4. A. Kojima, K. Teshima, Y. Shirai and T. Miyasaka, *J. Am. Chem. Soc.*, 2009, **131**, 6050-6051.
5. M. Saliba, T. Matsui, K. Domanski, J.-Y. Seo, A. Ummadisingu, S. M. Zakeeruddin, J.-P. Correa-Baena, W. R. Tress, A. Abate and A. Hagfeldt, *Science*, 2016, **354**, 206-209.
6. X. Yin, P. Chen, M. Que, Y. Xing, W. Que, C. Niu and J. Shao, *ACS Nano*, 2016, **10**, 3630-3636.
7. C. Roldán-Carmona, O. Malinkiewicz, A. Soriano, G. M. Espallargas, A. Garcia, P. Reinecke, T. Kroyer, M. I. Dar, M. K. Nazeeruddin and H. J. Bolink, *Energy Environ. Sci.*, 2014, **7**, 994-997.
8. K. Seki, A. Furube and Y. Yoshida, *Jpn. J. Appl. Phys.*, 2015, **54**, 08KF04.
9. W.-J. Yin, J.-H. Yang, J. Kang, Y. Yan and S.-H. Wei, *J. Mater. Chem. A*, 2015, **3**, 8926-8942.
10. S.-S. Kim, S.-I. Na, J. Jo, D.-Y. Kim and Y.-C. Nah, *Appl. Phys. Lett.*, 2008, **93**, 305.
11. L. Qiao, D. Wang, L. Zuo, Y. Ye, J. Qian, H. Chen and S. He, *Appl. Energy*, 2011, **88**, 848-852.
12. S.-W. Baek, J. Noh, C.-H. Lee, B. Kim, M.-K. Seo and J.-Y. Lee, *Sci. Rep.*, 2013, **3**.
13. J.-H. Im, C.-R. Lee, J.-W. Lee, S.-W. Park and N.-G. Park, *Nanoscale*, 2011, **3**, 4088-4093.
14. W. J. Yin, T. Shi and Y. Yan, *Adv. Mater.*, 2014, **26**, 4653-4658.
15. P. Christopher, H. Xin and S. Linic, *Nat. Chem.*, 2011, **3**, 467-472.
16. Y. Sun and Y. Xia, *Science*, 2002, **298**, 2176-2179.
17. T. Kawawaki, H. Wang, T. Kubo, K. Saito, J. Nakazaki, H. Segawa and T. Tatsuma, *ACS Nano*, 2015, **9**, 4165-4172.
18. S.-W. Baek, G. Park, J. Noh, C. Cho, C.-H. Lee, M.-K. Seo, H. Song and J.-Y. Lee, *ACS Nano*, 2014, **8**, 3302-3312.
19. K. Leonard, J. You, Y. Takahashi, H. Yonemura, J. Kurawaki and S. Yamada, *J. Phys. Chem. C*, 2015, **119**, 8829-8837.
20. J. J. Mock, R. T. Hill, A. Degiron, S. Zauscher, A. Chilkoti and D. R. Smith, *Nano Lett.*, 2008, **8**, 2245-2252.
21. C. Ciracì, R. T. Hill, J. J. Mock, Y. Urzhumov, A. I. Fernández-Domínguez, S. A. Maier, J. B. Pendry, A. Chilkoti and D. R. Smith, *Science*, 2012, **337**, 1072-1074.
22. Q. Zhang, W. Li, L. P. Wen, J. Chen and Y. Xia, *Chem. Eur. J.*, 2010, **16**, 10234-10239.
23. E. D. Palik, *Handbook of optical constants of solids*, Academic press, 1998.
24. S. H. Im, Y. T. Lee, B. Wiley and Y. Xia, *Angew. Chem.*, 2005, **117**, 2192-2195.
25. A. Taguchi, S. Fujii, T. Ichimura, P. Verma, Y. Inouye and S. Kawata, *Chem. Phys. Lett.*, 2008,

462, 92-95.

26. S.-J. Jeon, J.-H. Lee and E. L. Thomas, *J. Colloid Interface Sci.*, 2014, **435**, 105-111.
27. Y. Huang, W. Zhang, J.-M. He, Z.-M. Chen, D.-Y. Tang, L.-J. Liu and S.-X. He, *Opt. Eng.*, 2013, **52**, 023602-023602.
28. T. Kawawaki, Y. Takahashi and T. Tatsuma, *J. Phys. Chem. C*, 2013, **117**, 5901-5907.
29. J. B. Lassiter, F. McGuire, J. J. Mock, C. Ciracì, R. T. Hill, B. J. Wiley, A. Chilkoti and D. R. Smith, *Nano Lett.*, 2013, **13**, 5866-5872.
30. J. Qi, X. Dang, P. T. Hammond and A. M. Belcher, *ACS Nano*, 2011, **5**, 7108-7116.
31. W. E. I. Zhang, M. Saliba, S. D. Stranks, Y. Sun, X. Shi, U. Wiesner and H. J. Snaith, *Nano Lett.*, 2013, **13**, 4505-4510.
32. J. A. Christians, J. S. Manser and P. V. Kamat, *J. Phys. Chem. Lett.*, 2015, **6**, 2086-2095.
33. B. Chen, M. Yang, S. Priya and K. Zhu, *J. Phys. Chem. Lett.*, 2016, **7**, 905-917.

Chapter 4

Simultaneous improvements of transparency and photocurrents of semi-transparent perovskite solar cells

4-1 Introduction

In Chapter 2, efficient way to improve visual transparency of perovskite solar cells (PVSCs) was presented, controlling the surface smoothness of perovskite layers by short spinning and vacuum drying (SSVD). Further, semi-transparent PVSCs were fabricated with smooth and semi-transparent perovskite layers by using thin transparent silver back electrodes.

With using smooth perovskite layers, electrode-coupled plasmons (ECPs) were also applied to PVSCs for photocurrent enhancement at the absorption edge of perovskite layers, as described in Chapter 3.

In this chapter, semi-transparent PVSCs with plasmons are developed. Though the transparency of semi-transparent PVSCs was greatly increased in Chapter 2, the improvement in the cell performances was not conspicuous because the thicknesses of perovskite layers were limited. Considering the ECPs, which have potential to improve photocurrents at the absorption edge of perovskite layers in PVSCs, it is conjectured that the enhancement of photocurrents in semi-transparent PVSCs near absorption edge of perovskite layers might not considerably affect a decrease in visual transparency because the enhanced region is beyond the visible range. In this regard, incorporation of the plasmon coupling between a semi-transparent electrode and silver nanocubes (AgNCs) was attempted on the semi-transparent PVSCs to realize photocurrent enhancements on the basis of ECPs.

At first, ideal conditions for the semi-transparent PVSCs with ECPs were examined by a finite-difference time-domain (FDTD) method. Then, the actual semi-transparent PVSCs with ECPs were fabricated for the optical and electrical analyses. Finally, the advantages of application of ECPs to semi-transparent PVSCs were discussed on the basis of the results.

4-2 Experimental

4-2-1 Synthesis of AgNCs

The experimental procedures are the same, as that described in Chapter 3.

4-2-2 Preparation of semi-transparent PVSCs

A patterned indium−tin oxide (ITO) electrode was pre-cleaned by deionized water, acetone and 2-propanol, followed by an oxygen plasma treatment (40 s). Poly(3,4-ethylenedioxythiophene):poly(styrene sulfonate) (PEDOT:PSS, Clevios AI 4083, 50 μL) was spin-coated at 5000 rpm for 30 s, then, heated at 150 °C for 10 min. The following fabrication procedure of perovskite layers are based on the short spinning and vacuum drying (SSVD) method introduced in chapter 2. The perovskite precursor of 3:1 ratio of CH_3NH_3I and $PbCl_2$ in dimethylformamide (28 wt% for 180 nm-thick and 32 wt% for 210 nm-thick perovskite layer) was spin-coated at 4000 rpm for 5 s on PEDOT:PSS under 50% of relative humidity. Then, the substrate was promptly transferred to a vacuum oven, in which the wetted film was dried at 0.05 kPa for 15 min, followed by annealing at the temperature range between 60 °C to 100 °C. The substrate was taken out to the ambient air and coated with phenyl-C_{61}-butyric acid methyl ester (PCBM, 1.8 wt % in chlorobenzene, 30 μL) at 3000 rpm for 45 s. A 15-μL aliquot of the AgNC suspension was dynamically dispensed onto the PCBM layer while the substrate was spinning at 4000 rpm to reach 2% coverage of AgNCs on PCBM. As transparent electrodes, 10 nm of bathocuproine (BCP), 10 nm of Ag and 10 nm of MoO_3 were deposited sequentially by vapor deposition.

4-2-3 Characterization

The same methods as those described in Chapter 2 were used.

4-2-4 Spectral simulation

Optical spectra and electric field distributions were simulated by FDTD method using FDTD Solutions (Lumerical Solutions). The simulation domain (400 × 400 × 400 μm) consisted of 4 nm cubic cells, and the central region (130 × 130 × 130 nm) around a AgNC was further meshed with a three-dimensional grid of 1 nm spacing. Backward scattering from the AgNC was monitored by a 340 × 340 nm square screen set 120 nm apart from the AgNC−PCBM interface. The dielectric functions of Ag, glass and MoO_3 were extracted from literature data.[1] Refractive index values of PCBM and BCP were 2 and 1.7 respectively.

4-3 A concept of increasing the photocurrents and transparency simultaneously

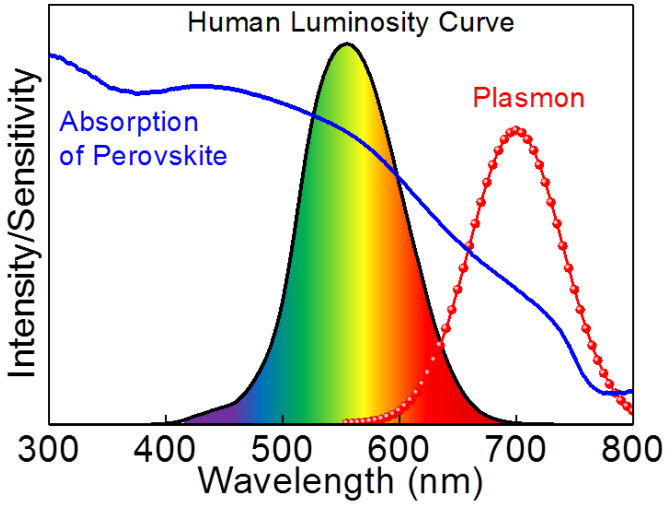

Figure 4-1. Concept of the visual transparency improvement of the semi-transparent solar cells based on the human luminosity curve. Data for the luminosity curve are obtained from Ref. 5.

Transmittance measured by a spectrophotometer is the most popular index of how the substrates are transparent. Thus, the most reports regarding semi-transparent solar cells show transmittance data as evidences for transparency of the cell.[2-4] However, transmittance itself would not fully stand for the actual visual transparency of the substrates having high scattering as described in Chapter 2, thereby the scattering factors should be taken into account for accurate evaluation of transparency. Furthermore, consideration of other factors such as luminosity is advisable to improve actual transparency to human's eyes.

Figure 4-1 illustrates the concept of the visual transparency improvement by considering luminosity,[5] absorption of perovskite layer and plasmons at the same time. Luminosity curve is the indicative of human visual perception of brightness. As confirmed from the curves, human eyes percept the wavelength near 580 nm as the brightest light and rarely sense the brightness of light in short (< 450 nm) and long wavelength ranges (> 650 nm). Also, the absorption of perovsite layers becomes weak near the absorption edge (< 650 nm). Thus, it is considered that the enhancement of photocurrents near the absorption edge of perovskite layers by plasmons would not interfere with the overall visual transparency as the enhanced region is beyond the sensitive range of human eyes.

On the basis of ECPs, which can enhance the photocurrents near the absorption edge of perovsikte layers as mentioned in Chapter 3, a similar concept was introduced to PVSCs

and semi-transparent PVSCs with ECPs were fabricated. The energy diagrams and the structures of the semi-transparent PVSCs with ECPs are illustrated in Figure 4-2. Semi-transparent PVSCs with ECPs developed here are basically similar to non-transparent PVSCs with ECPs introduced in chapter 3. As transparent electrodes, thin silver (10 nm) and MoO_3 (10 nm) were sequentially deposited on BCP layers. The function of MoO_3 is to enhance the transmittance on the basis of zero-reflection conditions as described in Chapter 2.[6-8] The green box in Figure 4-2a shows the structure of ECPs in which AgNCs face the semi-transparent electrode of silver and MoO_3 via the thin BCP layer.

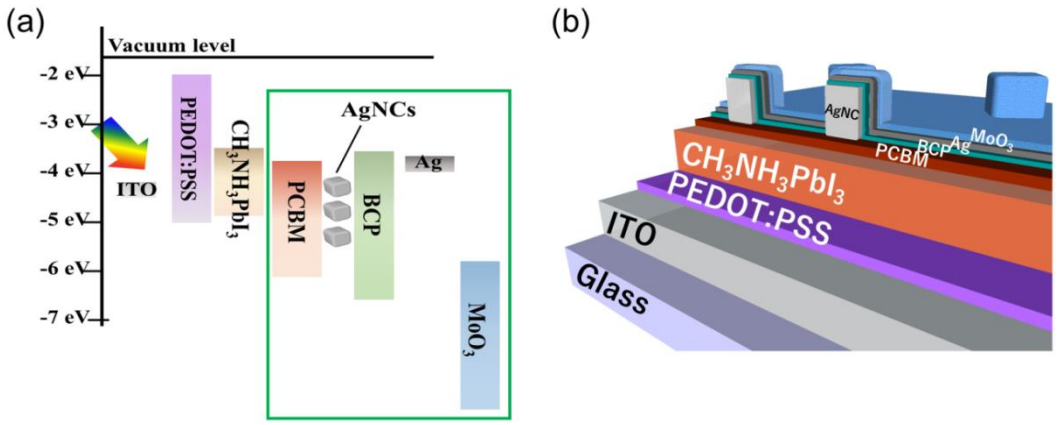

Figure 4-2. (a) Energy diagram and (b) the structure of semi-transparent PVSCs based on ECPs.

4-4 FDTD Simulation of ECPs

4-4-1 Dependence on the thickness of BCP

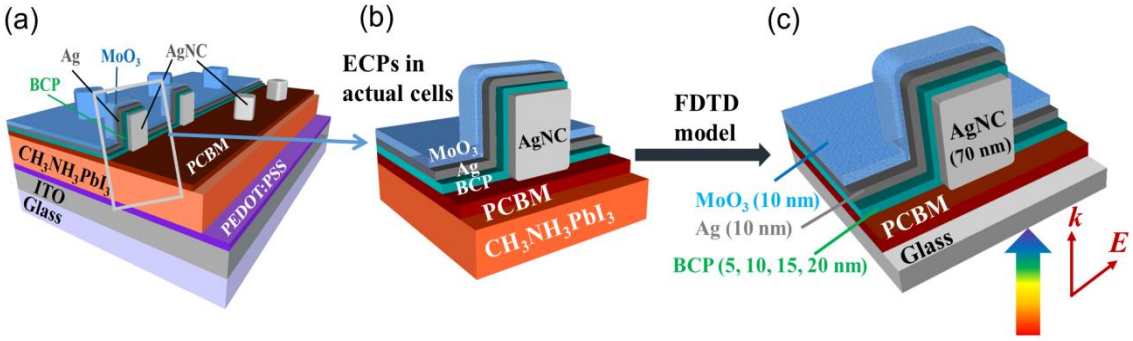

Figure 4-3. (a,b) The structures for ECPs in actual semi-transparent PVSCs. (c) The corresponding model for FDTD calculation.

Different from the typical ECPs in which thick metal films are used, the plasmonic structure for ECPs in semi-transparent PVSCs here consists of AgNCs, a thin silver electrode and thin semiconductor layer. To examine the plasmonic scattering and absorption of ECPs in semi-transparent cells, FDTD simulations were executed. The models for the calculation of FDTD consist of glass/PCBM/AgNC/BCP/thin Ag/MoO_3 (Figure 4-3c). The models used for the simulations are similar to the actual structure for ECPs (Figure 4-3a,b), in which the perovskite layer is substituted with a glass substrate.

In typical film-coupled plasmons, the thickness of insulators between nanoparticles and metal films affects the plasmonic peak wavelengths largely. Thus, the thickness of BCP was also examined. As shown in Figure 4-3c, 5, 10, 15, 20 nm of BCP layers were calculated. It is noted that the thickness of PCBM, Ag and MoO_3 is 10 nm each with 70 nm of AgNC.

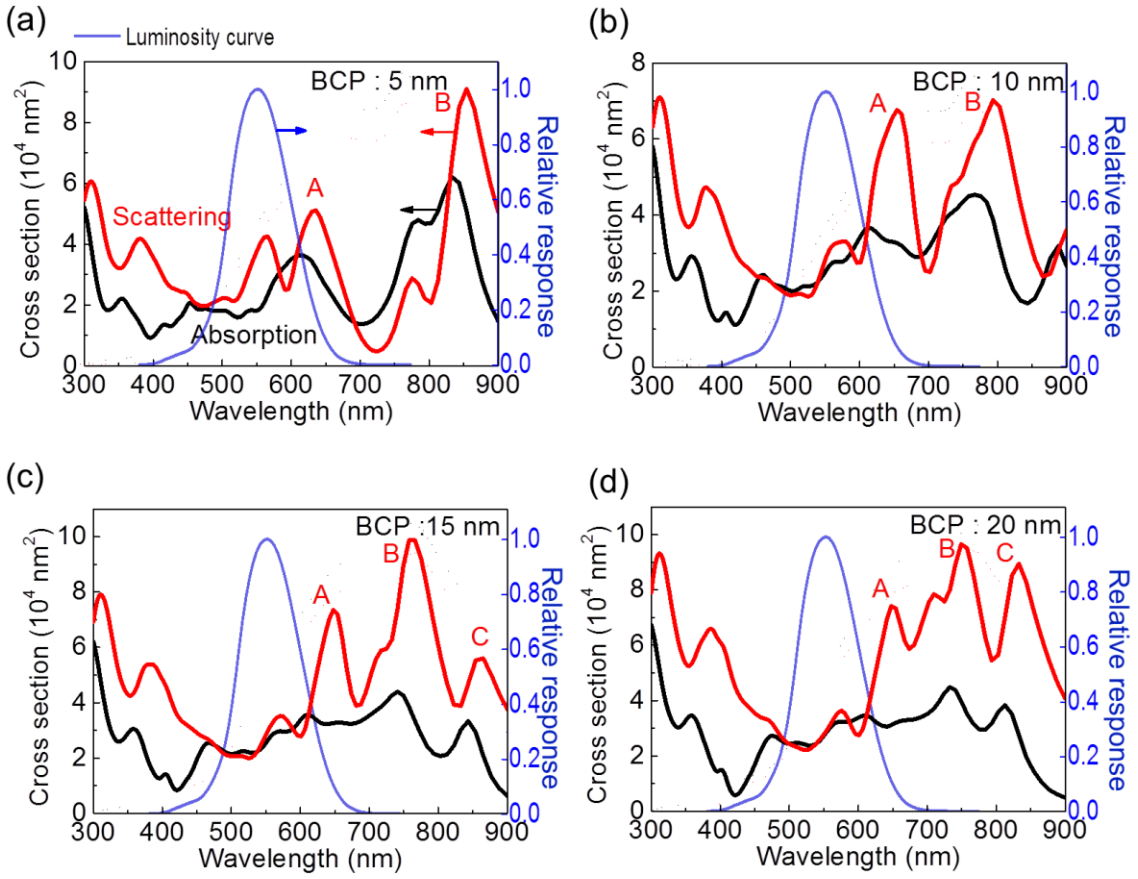

Figure 4-4. Plasmonic scattering and absorption spectra of ECPs applied to semi-transparent PVSCs consisting of glass/PCBM (10 nm)/AgNC (70 nm)/BCP/Ag (10 nm)/MoO_3 (10 nm) in which the thickness of BCP is (a) 5 nm, (b) 10 nm, (c) 15 nm or (d) 20 nm. The blue lines indicate luminosity curves.

The Figure 4-4 shows the simulation results regarding plasmonic scattering and absorptions. In a similar manner to ECPs in the non-transparent PVSCs, the broadly separated scattering peaks were observed for ECPs with thin Ag metals. When the BCP is thin (5 nm), main two peaks A and B are observed at 640 nm and 850 nm, respectively (Figure 4-4a). The intensity of scattering compared to that of absorption increases when the BCP layers are thicker and the peaks become narrower and peak B is blue-shifted, which are in accordance with ECPs in the non-transparent PVSCs and other film-coupled plasmons.[9] Thus, when BCP is 10 nm, the locations of peak A and peak B are 655 nm and 810 nm, respectively (Figure 4-4b). Another peak C at 860 nm (Figure 4-4c) starts to be seen because the interval of the peaks is narrower when the BCP is thicker (15 nm). The peak C is more blue-shifted to 830 nm when the BCP is 20 nm. Peak A tends to stay at around 650 nm while peak B and peak C are blue-shifted when the BCP layers are thicker. Thus, it is expected that peak B and peak C are assigned to ECPs while peak A is not ascribed to ECP, which might stem from the existence of MoO_3.

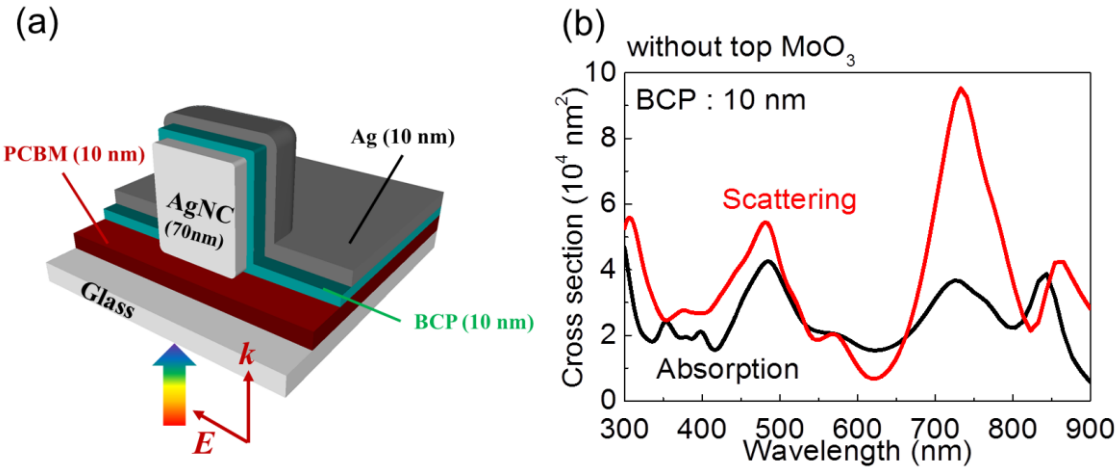

Figure 4-5. (a) The model for ECPs without MoO_3 for the FDTD simulation. (b) Plasmonic scattering and absorption spectra of ECPs based on the model in (a).

ECPs without MoO_3 layers were also checked for comparison on the basis of the models shown in Figure 4-5. The thickness of PCBM, BCP and Ag was 10 nm, respectively in the model shown in Figure 4-5a. In the case without MoO_3, broadly separated peaks are also observed in a similar manner to other ECPs. However, the peak near 650 nm is not seen, supporting the assumption that peak A in Figure 4-4 is caused by MoO_3.

Considering the luminosity curves (blue lines in Figure 4-4), BCP layer thickness of >

10 nm is adequate as the enhanced plasmonic scattering regions are positioned above the sensitive region of luminosity curves. As the scattering intensity increases with the thickness of BCP, using 20 nm BCP (Figure 4-4d) seems to be advantageous for improving photocurrents with keeping visual transparency of the semi-transparent PVSCs. However, the BCP layers in actual PVSCs function as electron transport layers (ETLs). The thick ETLs might seriously affect the serial resistance of the cells. In this respect, 10 nm of BCP is expected to be ideal for the application of ECPs to the semi-transparent PVSCs.

4-4-2 Near-field antenna effect

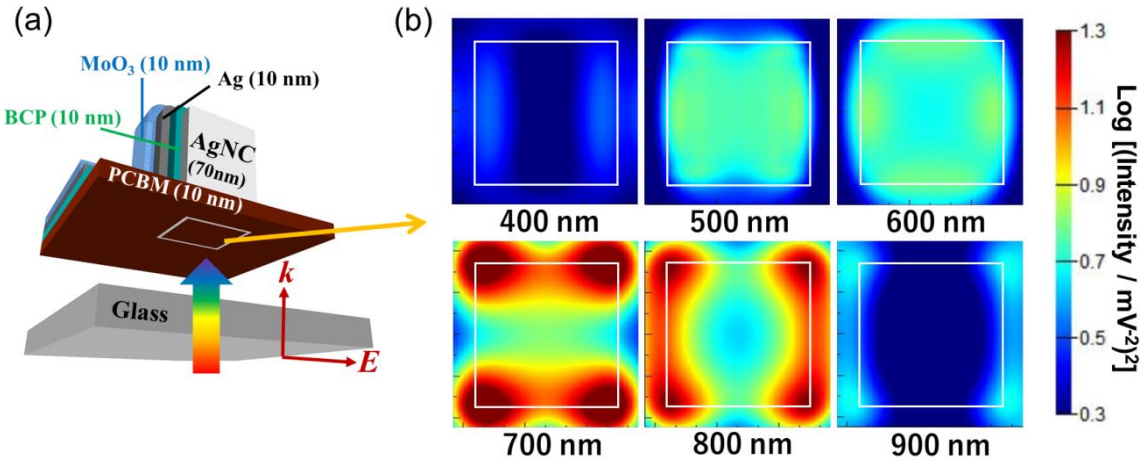

Figure 4-6. (a) The interface between PCBM and glass. (b) Electric field distributions at the interface depicted in (a). The white square is 10 nm below AgNC-PCBM interface. The intensity scale is logarithm of E^2.

Based on the results in the previous section, it is conjectured that 10 nm thicknesses of PCBM, BCP, Ag and MoO_3 with 70 nm of AgNCs are considered to be advantageous for the application to semi-transparent PVSCs. For further analysis, the near-field antenna effect was also considered for the models with above-mentioned conditions. Because the effective distance of near field from a metal nanoparticle (MNP) is extremely small, it is necessary to examine whether the near field caused from ECPs can reach perovsite layers. Thus, the electric fields at the PCBM-glass interface were calculated and shown in Figure 4-6. The electric fields are weak at 400 nm and start to be seen inside the white box (10 nm below AgNC-PCBM interface) at > 500 nm. The strong electric fields are observed at 700-800 nm, especially near the edge of white box due to strong electric fields typically generated at the corner of AgNCs.[10, 11] The strong

intensity should be related to the strong scattering peaks because both of the near field and far-field scattering stem from plasmonic resonance (Figure 4-4b). The intensity at the interface is weakened at long wavelengths because the resonant intensity becomes weak.

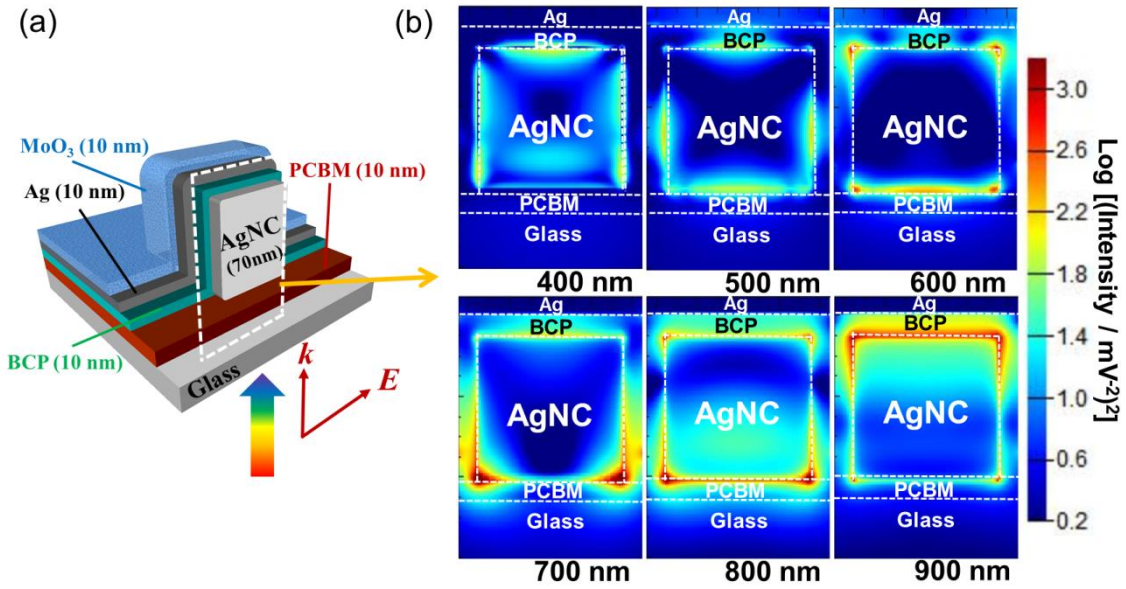

Figure 4-7. (a) Schematic illustration of the vertical plane at which (b) the electric field distributions are monitored at different wavelengths.

The electric fields at the vertical plane shown in Figure 4-7a of ECPs were also observed (Figure 4-7b). At short wavelengths (<500 nm), the electric fields are delocalized near AgNC. At 600 nm, electric fields are localized at the corners of both top and bottom of AgNC, thereby intensity of electric field at the PCBM-glass interface starts to increase (Figure 4-7b). The electric fields are strongly localized at the proximal face of AgNC at 700 nm. This strongly affects the electric fields at the PCBM-glass interface as the strongly localized electric fields can penetrate the PCBM layers. Localization of electric fields at the proximal face is still observed at 800 nm. At 900 nm the direction of localization becomes upside down, showing strong electric fields at the distal face of AgNC. Since the perovskite layers have weak light absorption near the absorption edge, the strong electric fields at the proximal face of AgNC based on ECPs here are expected to be advantageous for the enhancement of photocurrents in semi-transparent PVSCs.

4-4-3 Quantification of near field

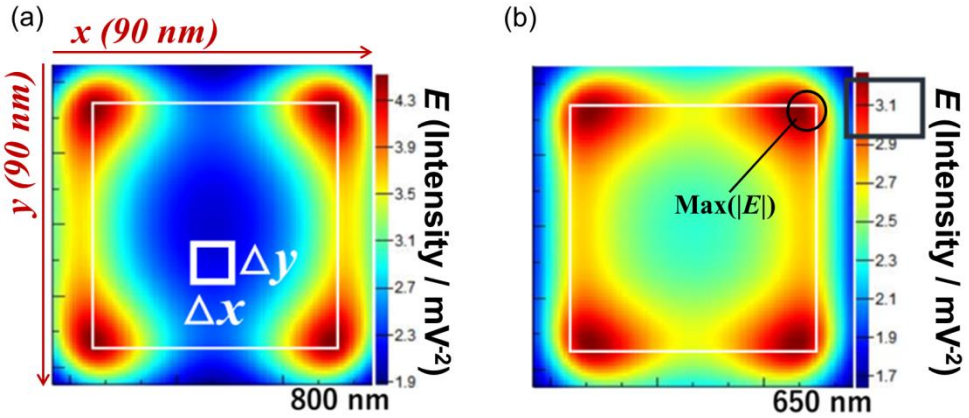

Figure 4-8. Schematic illustrations for (a) average value and (b) the maximum value of the electric fields by ECPs at the PCBM-glass interface.

As shown in Figure 4-6, intensities of electric fields are higher near the corner of AgNC. To accurately calculate how the electric fields affect the perovskite layers, the whole electric fields which include weak intensity regions should also be considered. Thus, the electric field at the PCBM-glass interface was integrated (Figure 4-8a) and the average value was calculated on the basis of eqs. 4-1,2,3.

$$\text{Average } |E| = \frac{1}{area} * \int_S |E(x,y)|\, dxdy \qquad \text{(eq. 4-1-1)}$$

$$\text{Average } |E| = \frac{1}{area} * \sum_y \sum_x |E(x,y)| \,\Delta x \,\Delta y \qquad \text{(eq. 4-1-2)}$$

$$\text{Average } |E|^2 = \frac{1}{area} * \sum_y \sum_x |E(x,y)|^2 \,\Delta x \,\Delta y \qquad \text{(eq. 4-1-3)}$$

A typical description for average value of electric field (average $|E|$) is given by eq. 4-1-1. Here, numerical integration was used for the calculation based on eq. 4-1-2 in which $\Delta x, \Delta y$ and area are 1 nm, 1 nm and 8100 nm^2, respectively. Since the light intensity is proportional to $|E|^2$, its average was also calculated on the basis of eq. 4-1-3. It is noted that the unit of typical electric fields are $|E|^2$ (intensity / mV^{-2}). The average $|E|$ and $|E|^2$ at each wavelength (interval = 20 nm) are shown in Figure 4-9a. The shapes of curves are similar to each other. Generally, the electric field intensities at PCBM-glass interface are high in the entire range of wavelength and tend to increase with wavelength. These high electric fields in wide range of wavelength are expected to

increase the photocurrents in semi-transparent PVSCs due to the near-field antenna effect. Figure 4-9b also shows the maximum values of electric fields. The highest value of $|E|$ and $|E|^2$ are seen mostly at around the corners of AgNC as shown in Figure 4-8b. Overall shapes of the curves based on the maximum values of $|E|$ and $|E|^2$ are similar to those of the curves based on average $|E|$ and $|E|^2$ for the semi-transparent PVSCs with ECPs.

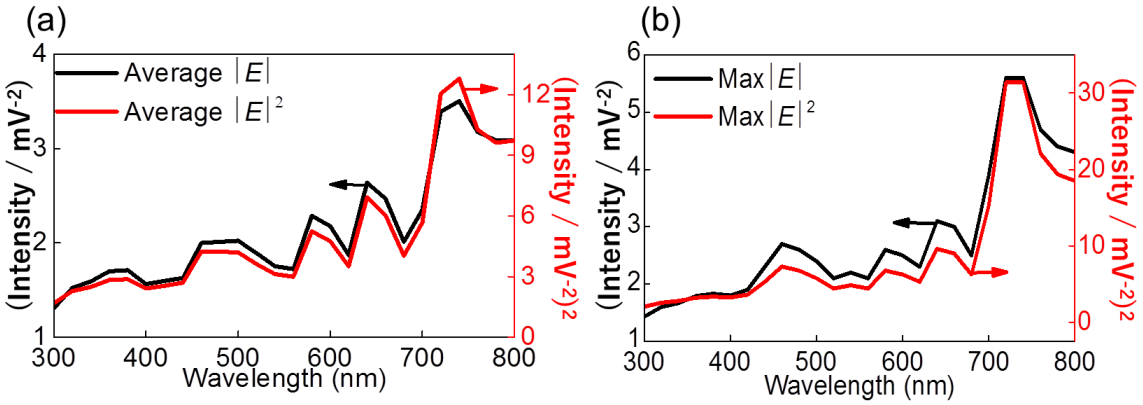

Figure 4-9. (a) Average $|E|$ and $|E|^2$ based on eq.4-1-2,3 and (b) the maximum values of $|E|$ and $|E|^2$ at the PCBM-glass interface of the glass/PCBM (10 nm)/AgNC (70 nm)/BCP (10 nm)/Ag (10 nm)/MoO_3 (10 nm) structure.

4-5 Semi-transparent PVSCs with ECPs

4-5-1 Optical and electrical characteristics

So far, the efficacy of ECPs in semi-transparent PVSCs has been introduced based on the FDTD simulation. Here, the actual semi-transparent PVSCs with ECPs were fabricated, the energy diagram and the structure of which were previously illustrated in Figure 4-2. In a similar manner to the non-transparent plasmonic PVSCs studied in Chapter 3, 2% coverage of AgNCs were loaded into ITO/PEDOT:PSS/$CH_3NH_3PbI_3$/PCBM substrates in which perovskite layers were processed by the SSVD method, which was studied in Chapter 2, due to the advantages of uniform loading of AgNCs and high performances.

Figure 4-10 shows semi-transparent PVSCs with and without ECPs in which 180 nm thick perovskite layers were used. For comparison, the actual semi-transparent PVSCs with and without ECPs were fabricated on the basis of the structures shown in Figure 4-10a,d. As depicted in Figure 4-10b,c, both of the cells have good transmittance regardless of ECPs, keeping similar visual transparency. In the cross-section images of the semi-transparent PVSCs with ECPs (Figure 4-10e), square shape of the electrode

(BCP/Ag/MoO_3) is observed, suggesting that AgNCs are well embedded in between PCBM and the electrode. Two positions of the electrode of the semi-transparent PVSC in which AgNCs are embedded are shown in Figure 4-10f as height profiles based on AFM measurements. These height profiles indicate that the height difference between the highest and lowest positions is 70 nm, which is in accordance with the size of AgNCs (70 nm). This suggests that the shape of electrodes tends to keep the overall geometries of AgNCs on PCBM.

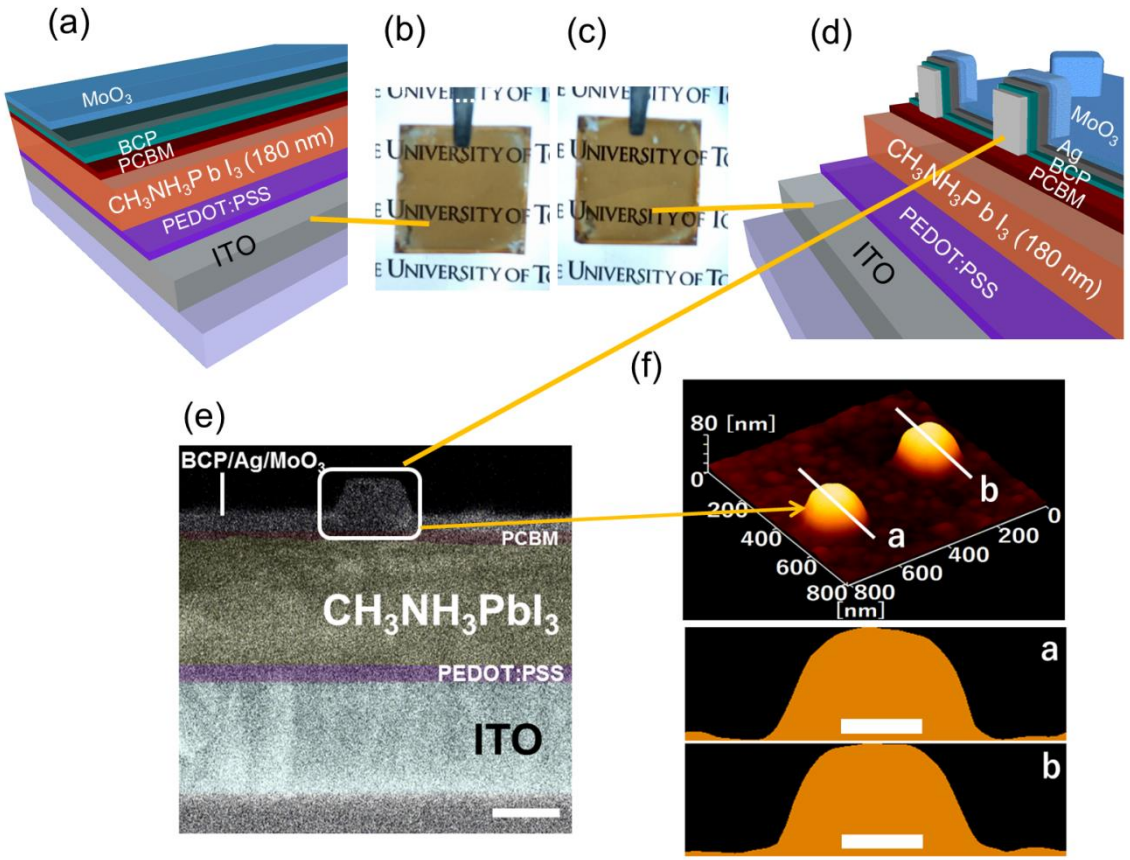

Figure 4-10. The structures and the photographs of semi-transparent PVSCs (a,b) without ECP and (c,d) with ECPs in which 180 nm-thick perovskite layers were used. (e) Cross-sectional SEM image and (f) height profiles based on AFM measurements of the semi-transparent PVSCs with ECPs. The scale bars for SEM and AFM are 100 nm and 50 nm, respectively.

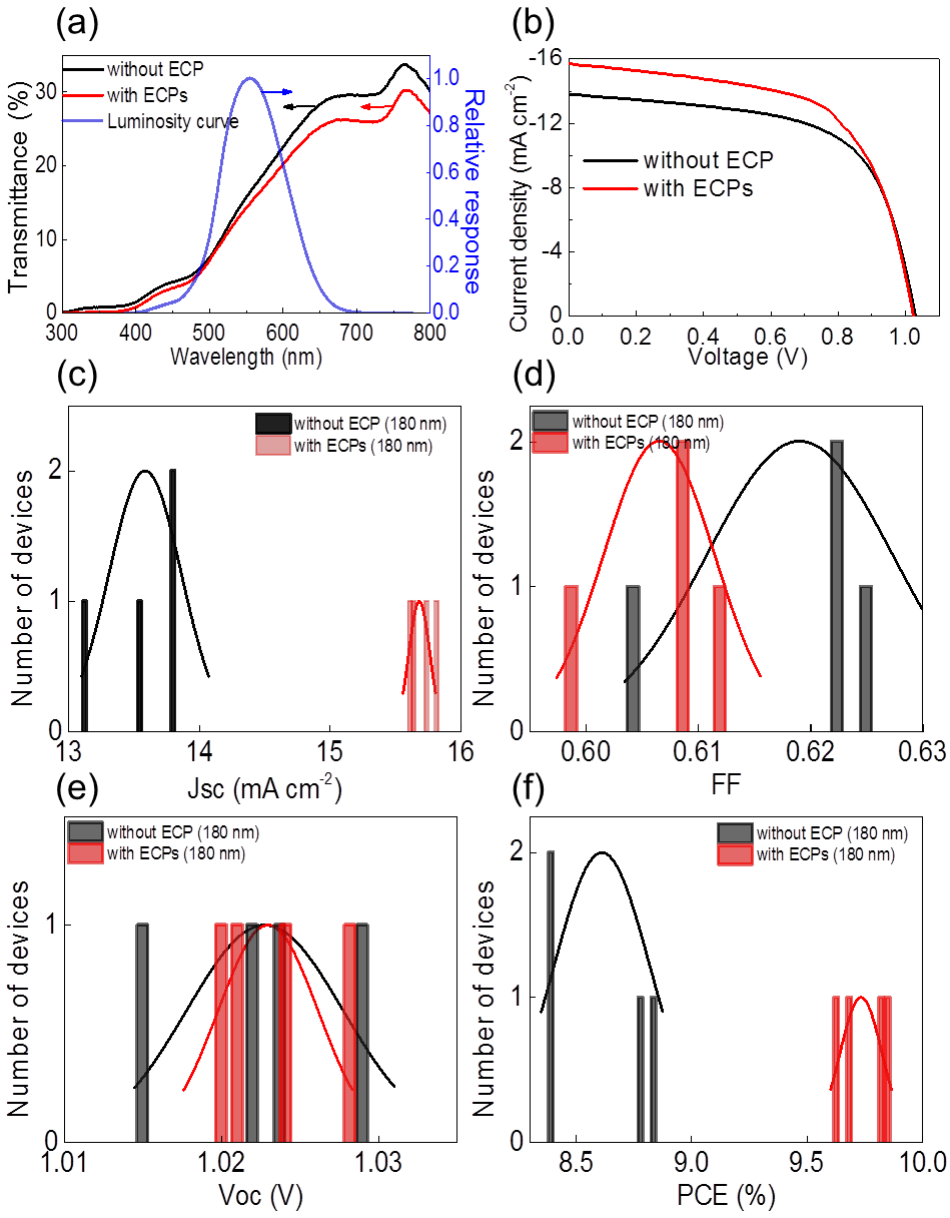

Figure 4-11. (a) Transmittance spectra and (b) *J-V* characteristics of the semi-transparent PVSCs with and without ECP in which 180 nm-thick perovskite layers were used. The blue line in (a) indicates luminosity curve. Distribution of (c) J_{sc}, (d) FF, (e) V_{oc} and (f) PCE of 4 different cells with and without ECP.

To concisely study the transparency and the performances of the cells, the transmittance spectra and *J-V* curves were measured and shown in Figure 4-11. A slight decrease in the transmittance is observed for the cells with ECPs because of the light loss by plasmonic scattering and absorption (Figure 4-11a). As confirmed by the FDTD simulation (Figure 4-4b), strong plasmonic resonance of ECPs occurs at > 600 nm and

the transmittance diminishes mostly at > 600 nm. The decrease in transmittance in the wavelength region where the human eyes are sensitive to light (500-600 nm) is relatively small. Thus, the visual transparency of the actual semi-transparent PVSCs is not largely affected by ECPs (Figure 4-10b,c). Despite the similar visual transparency, PCEs of the cells with ECPs are higher (Figure 4-11b). Figure 4-11c-f show distribution of the parameters of 4 cells with and without ECP. It is obvious that FF and V_{oc} are remained similar regardless of ECPs. The ECPs lead to the large increase in the photocurrents from 13.48 ± 0.38 mA cm^{-2} to 15.69 ± 0.11 mA cm^{-2}, and thereby the increase in the PCEs from 8.62 ± 0.24% to 9.73 ± 0.12%. Parameters are shown in Table 4-1 in detail.

Table 4-1. Performances of the semi-transparent PVSCs with and without ECPs under AM 1.5G light irradiation[a,b]

ECP	Thickness (nm)	J_{sc} (mA cm^{-2})	V_{oc} (V)	FF	PCE (%)	AVT (%)	VTI (%)
ECP	~180	15.69 ± 0.11	1.02 ± 0.0046	0.60 ± 0.0074	9.73 ± 0.12	17.8	15.6
–	~180	13.48 ± 0.38	1.02 ± 0.0079	0.61 ± 0.012	8.62 ± 0.24	19.8	16.3
–	~210	15.34 ± 0.35	1.00 ± 0.0043	0.60 ± 0.0098	9.18 ± 0.19	15.2	12.2

[a]All the values (mean ± standard deviation) were evaluated for at least four cells. The light intensity was 100 mW cm^{-2}.

[b]AVT and VTI were calculated from the average of 3 different cells.

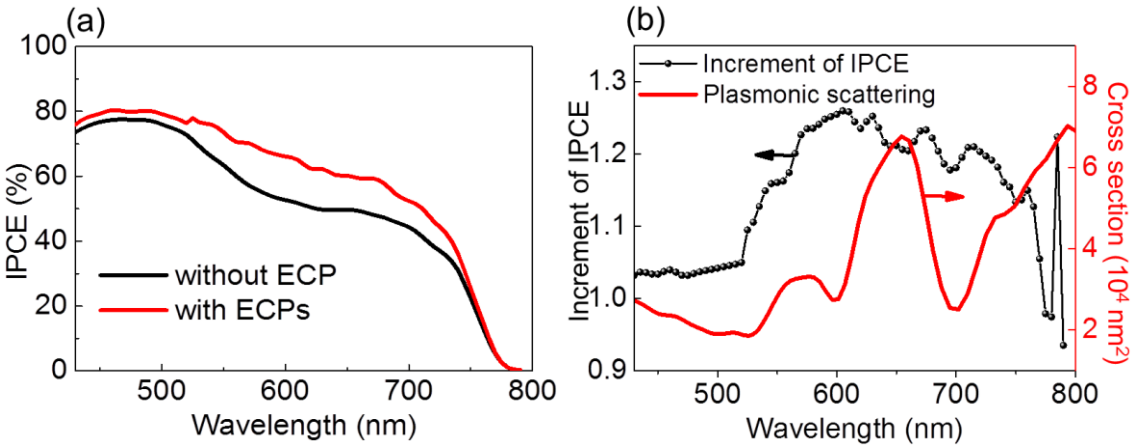

Figure 4-12. (a) IPCE spectra of the semi-transparent PVSCs with and without ECP. (b) Increment of IPCE and plasmonic scattering spectra obtained by the FDTD simulation in Figure 4-4b.

The incident photon-to-current conversion efficiencies (IPCEs) were also measured and shown in Figure 4-12. IPCE data indicate that the photocurrents of cells with ECPs are larger in the entire range of wavelength compared to the cells without ECP (Figure 4-12a). Figure 4-12b shows the increment of IPCE (based on eq. 4-2) and plasmonic scattering of ECPs calculated by FDTD in which glass/PCBM (10 nm)/AgNC (70 nm)/BCP (10 nm)/Ag (10 nm)/MoO_3 (10 nm) as used as a model.

$$\text{Increment of IPCE} = \frac{\text{IPCE of cells with ECPs}}{\text{IPCE of cells without ECP}} \qquad \text{(eq. 4-2)}$$

The increment ratio of IPCE starts to increase at 530 nm at which the plasmonic scattering and the electric field intensity at the PCBM-glass interface (Figure 4-9a) have high values. Thus it is conjectured that the enhancement of photocurrents of semi-transparent PVSCs are caused by the far-field scattering and near-field antenna effect based on ECPs. The increase in electronic conductivity of the devices might also enhance the cell's performances because of the electron injection from AgNCs to the ETL under light irradiation by plasmon-induced charge separation (PICS).[12] Further investigation regarding PICS might be necessary for precise analyses.

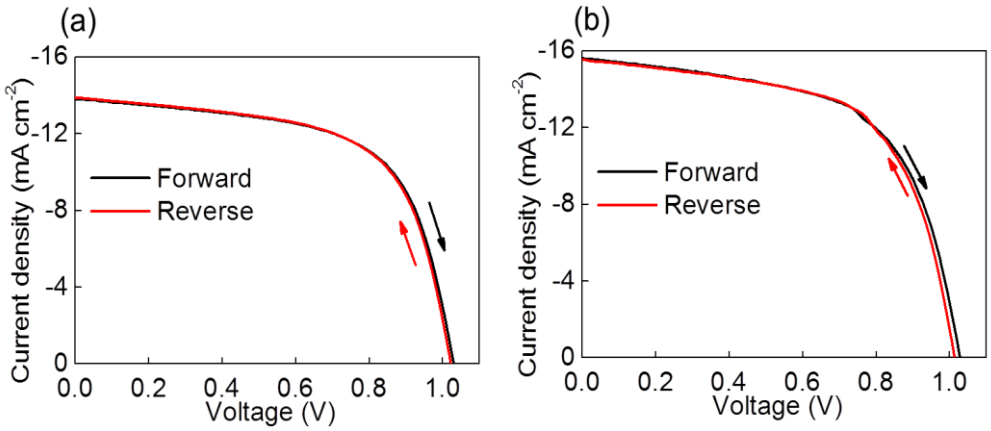

Figure 4-13. *J-V* characteristics by forward and reverse sweep of the semi-transparent PVSCs (180 nm-thick perovskite layers) (a) without ECP and (b) with ECPs. The sweep rate is 100 mV s^{-1}.

Lastly, the hysteresis is also examined for the semi-transparent PVSCs with and without ECPs as it may lead to the overestimation of the actual performances of the cells.[13, 14] As described in Chapter 2, PVSCs in which perovskite layers are processed by SSVD do not usually show severe hysteresis. The semi-transparent PVSCs developed

here also show similar performances regardless of sweeping direction (Figure 4-13a). Though V_{oc} of the cells with ECPs is slightly decreased for reverse sweep (Figure 4-13b), the values of the PCEs are similar due to slightly higher FF. Thus, semi-transparent PVSCs with ECPs have reliable performances.

4-5-2 Comparison with thicker cells without ECP

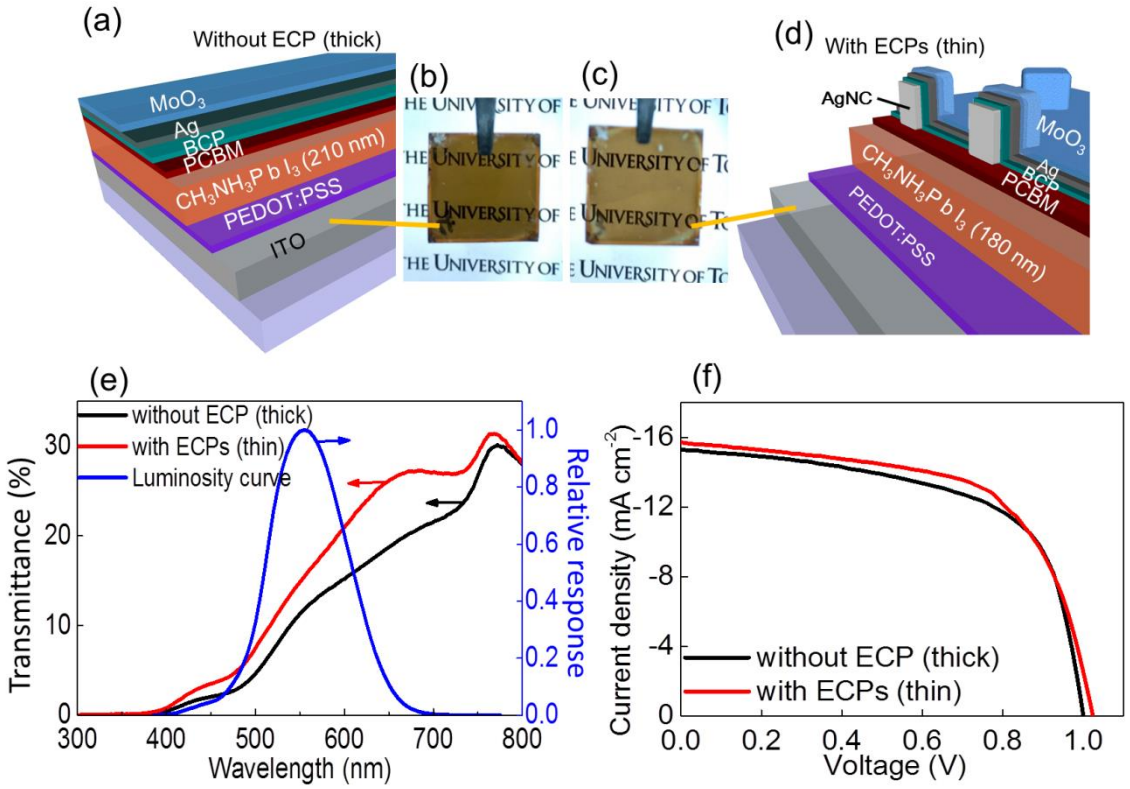

Figure 4-14. The structures and the photographs of semi-transparent PVSCs (a,b) without ECPs in which a thick perovskite layer (210 nm) is used and (c,d) those of PVSCs with ECPs in which a thin perovskite layer (180 nm) is used. (e) Transmittance spectra and (f) *J-V* characteristics of the cells. The blue line in (e) indicates luminosity curve.

The photocurrents of semi-transparent PVSCs with ECPs (180 nm-thick perovskite layers) exhibit 15.69 ± 0.11 mA cm^{-2}. To reach the similar photocurrents without using ECPs, thicker perovskite layers should be used to increase the light absorption.

Here the semi-transparent PVSCs without ECPs in which thicker perovskite layers (210 nm) were used were fabricated and their optical and electrical properties were measured (Figure 4-14). The structures illustrating all the layers and the thickness of perovskite films without and with ECPs are shown in Figure 4-14a,d and the actual cells

are displayed in Figure 4-14b,c. Obviously, the visual transmittance of thin cells with ECPs (Figure 4-14c) seems superior to that of thick cells without ECPs (Figure 4-14b). From the transmittance data measured by spectrophotometry (Figure 4-14e), the transmittance of thin cells with ECPs is higher in the entire range of spectrum than that of the thick cell without ECP. In the high luminosity region (500-600 nm), the amount of decrease in the transmittance of the thick cell is considerable, thereby the visual transparency becomes lower. The high absorption coefficient of perovskite leads to the large decrease in transmittance with the increase in thickness[15] while the amounts of absorption and scattering by ECPs are minor and localized at the absorption edge of perovskite layers. *J-V* characteristics of thick cells without ECPs were examined and compared with the thin cells with ECPs (Figure 4-14f). The PCE value of thick cells without ECP is 9.18 ± 0.19%, which is similar to that of thin cells with ECPs (9.73 ± 0.12%).

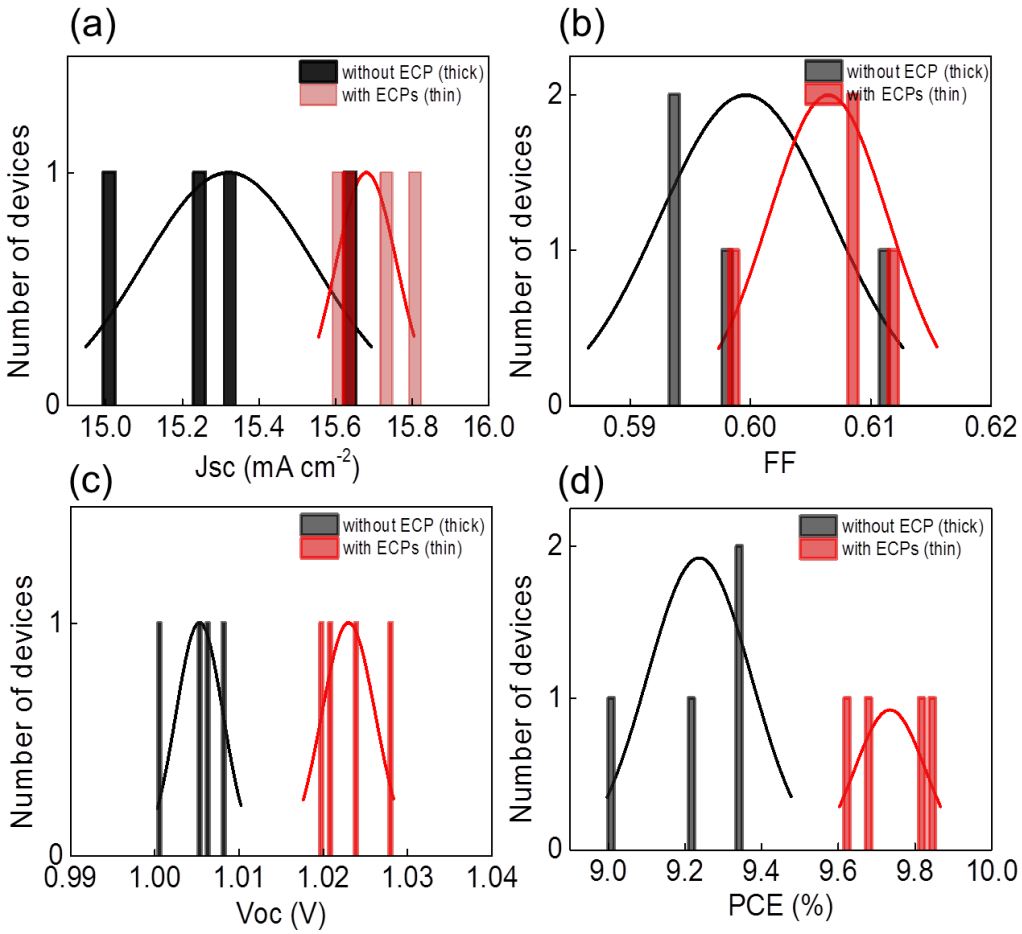

Figure 4-15. Distributions of (c) J_{sc}, (d) FF, (e) V_{oc} and (f) PCE of 4 different thick cells without ECP and thin cells with ECPs.

Figure 4-15 shows the distributions of parameters (J_{sc}, FF, V_{oc} and PCE) of 4 thick cells without ECP and thin cells with ECPs for comparison. FF values for both cells are similar and J_{sc} for the thick cells without ECPs is slightly lower. V_{oc} for thin cells with ECPs is higher, which is in accordance with the previous results described in Chapter 2, in which PVSCs with thin perovskite layers tend to have higher V_{oc}. Therefore, the PCE values of thin cells with ECPs are slightly higher despite the thin perovskite layers. These results indicate that the ECPs are efficient to increase photocurrents and visual transparency than the use of thick perovskite layers.

4-5-3 Evaluation of the visual transparencies

Transmittance of the cells measured using a spectrophotometer gives important information of how the cells transmit light, which is the main reason it has been prevalently used to evaluate semi-transparent photovoltaic cells.[2-4, 16, 17] However, as described in Chapter 2, transmittance itself is not enough to fully indicate the real visual transparency for human eyes. In this regard, two indications for the transmittance of semi-transparent PVSCs are defined; One is average transmittance (AVT) and another is visual transparency index (VTI) indicated by eqs. 4-3-1,2. It is noted that *T* and *HLF* indicate transmittance and human luminosity factor, respectively, as functions of wavelength (λ).

$$\mathrm{AVT}\ (\%) = \frac{\int_{400}^{800} T(\lambda) d\lambda}{(800-400)} \qquad \text{(eq. 4-3-1)}$$

$$\mathrm{VTI}\ (\%) = \frac{\int_{400}^{800} [T(\lambda)\, HLF(\lambda)] d\lambda}{\int_{400}^{800} HLF(\lambda) d\lambda} \qquad \text{(eq. 4-3-2)}$$

Schematic illustrations for eqs. 4-3-1,2 are shown in Figure 4-16. AVT (eq. 4-3-1) is the most popular way to evaluate overall transparency of semi-transparent cells in previous works. In Figure 4-16a, the red area indicates the numerator of eq. 4-3-1. In this work, human luminosity factor (Figure 4-16b) is also taken into account (Figure 4-16c). The red area in Figure 4-16c indicates the numerator of eq. 4-3-2. This numerator is finally divided by the integration of *HLF* to give VTI.

The values of AVT and VTI together with the parameters of *J-V* performances of all the semi-transparent PVSCs prepared in this chapter are indicated in Table 4-1. In the

case of the thin cells (180 nm-thick perovskite layers), the AVT value of cells with ECPs (17.8%) is lower than that of cells without ECP (19.8%) by 2%. However, the difference of VTI is just 0.7% suggesting that the visual transparencies of both cells are similar. The thick cells (210 nm-thick perovskite layers) have the lowest AVT and VTI values of 15.2% and 12.2%, respectively. Thus, the visual transparency of thick cells without ECP is inferior to that of thin cells either with or without ECP.

The VTI value of the thin cells with ECPs is higher than that of the thick cell without ECP by 3.4%, despite the higher PCE value.

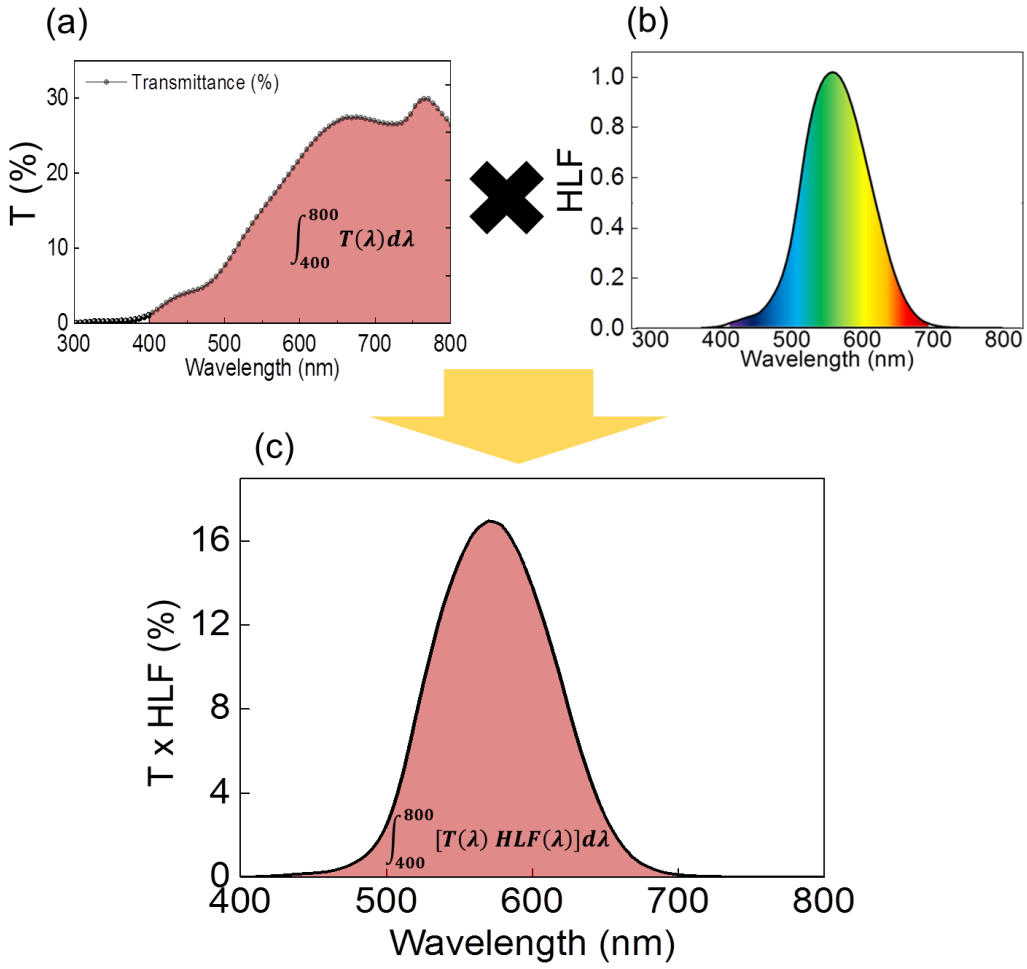

Figure 4-16. (a) Transmittance spectrum of a semi-transparent PVSC; *T (λ)*. The red area indicates the numerator of eq. 4-3-1. (b) Human luminosity curve; *HLF(λ)*. (c) *T (λ)* x *HLF(λ)*. The red area indicates the numerator of eq. 4-3-2, which is the integration of *T (λ)* x *HLF(λ)*.

4-6 Conclusions

By using the plasmon coupling between AgNCs and a thin transparent silver electrode (ECPs), high performance semi-transparent PVSCs were successfully developed. Easy tunability of plasmonic wavelength by ECPs allowed a great increase in photocurrents of the semi-transparent PVSCs in the deep red region where photosensitivity of human eyes is relatively low, leading to good visual transparency. Considering easy processability, ECPs are expected to be applied to a variety of photovoltaic cells, making thin-electrode with ECPs a promising alternative to a transparent electrode in semi-transparent cells.

4-7 References

1. E. D. Palik, *Handbook of optical constants of solids*, Academic press, 1998.
2. J. Van De Lagemaat, T. M. Barnes, G. Rumbles, S. E. Shaheen, T. J. Coutts, C. Weeks, I. Levitsky, J. Peltola and P. Glatkowski, *Appl. Phys. Lett.*, 2006, **88**, 233503.
3. J. Wu, H. A. Becerril, Z. Bao, Z. Liu, Y. Chen and P. Peumans, *Appl. Phys. Lett.*, 2008, **92**, 237.
4. C. D. Bailie, M. G. Christoforo, J. P. Mailoa, A. R. Bowring, E. L. Unger, W. H. Nguyen, J. Burschka, N. Pellet, J. Z. Lee and M. Grätzel, *Energy Environ. Sci.*, 2015, **8**, 956-963.
5. L. T. Sharpe, A. Stockman, W. Jagla and H. Jägle, *J Vis*, 2005, **5**, 3-3.
6. B. Tian, G. Williams, D. Ban and H. Aziz, *J. Appl. Phys.*, 2011, **110**, 104507.
7. K. Hong, K. Kim, S. Kim, I. Lee, H. Cho, S. Yoo, H. W. Choi, N.-Y. Lee, Y.-H. Tak and J.-L. Lee, *J. Phys. Chem. C*, 2011, **115**, 3453-3459.
8. G. H. Jung, K. Hong, W. J. Dong, S. Kim and J. L. Lee, *Adv. Energy Mater.*, 2011, **1**, 1023-1028.
9. J. B. Lassiter, F. McGuire, J. J. Mock, C. Ciracì, R. T. Hill, B. J. Wiley, A. Chilkoti and D. R. Smith, *Nano lett.*, 2013, **13**, 5866-5872.
10. T. Kawawaki, H. Wang, T. Kubo, K. Saito, J. Nakazaki, H. Segawa and T. Tatsuma, *ACS Nano*, 2015, **9**, 4165-4172.
11. K. Saito and T. Tatsuma, *Adv. Opt. Mater.*, 2015, **3**, 883-887.
12. T. Tatsuma, H. Nishi and T. Ishida, *Chem. Sci.*, 2017, **8**, 3325-3337.
13. B. Chen, M. Yang, S. Priya and K. Zhu, *J. Phys. Chem. Lett.*, 2016, **7**, 905-917.
14. J. A. Christians, J. S. Manser and P. V. Kamat, *J. Phys. Chem. Lett.*, 2015, **6**, 2086-2095.
15. J.-H. Im, C.-R. Lee, J.-W. Lee, S.-W. Park and N.-G. Park, *Nanoscale*, 2011, **3**, 4088-4093.
16. M. G. Kang, T. Xu, H. J. Park, X. Luo and L. J. Guo, *Adv. Mater.*, 2010, **22**, 4378-4383.
17. R. Betancur, P. Romero-Gomez, A. Martinez-Otero, X. Elias, M. Maymó and J. Martorell, *Nature Photon.*, 2013, **7**, 995-1000.

Chapter 5

Conclusions

The superiority of light absorption and long carrier diffusion length of organic-inorganic hybrid perovskites enable perovskite solar cells (PVSCs) to exhibit high power conversion efficiencies (PCEs) comparable to silicon-based solar cells. Due to the short history, many issues regarding PVSCs have not yet been addressed, suggesting that the space for further improvements of PVSCs is still large. The remaining issues include hysteresis and instability of PVSCs based on $CH_3NH_3PbI_3$ in ambient air. Development of semi-transparent PVSCs is also one of the interesting topics. Since the advent of solution-processed photovoltaics, fabrication of flexible and semi-transparent solar cells has become possible, enabling them to be used as wearable devices and window applications. Though high performance novel semi-transparent electrode materials such as graphenes and silver nanowires have been developed, a majority of semi-transparent solar cells exhibit low PCEs due to low light absorption of active layers. In this regard, application of PVSCs to semi-transparent cells has been considered to be a great solution to get high performances. However, the transparency of perovskites is not superior to that of other solution-processed materials because of their high absorption coefficient values and light scattering due to their rough surfaces. Thus, the improving the transparency of PVSCs with keeping their high performances is the main key to realize high performance semi-transparent PVSCs.

In the present work, development of semi-transparent PVSCs is mainly discussed. To improve the transparency of perovskite films, a novel method named short-spinning and vacuum-drying (SSVD) is developed. Also, plasmon coupling between metal nanoparticles (MNPs) and a metal electrode film, which is named electrode-coupled plasmons (ECPs), are proposed and exploited for enhancement of photovoltaic performances of the semi-transparent PVSCs in a wavelength range where human eyes are not very sensitive to light, by taking advantage of the plasmonic near-field antenna effect and far-field scattering effect. Furthermore, these two approaches are combined for development of high performance semi-transparent PVSCs.

In Chapter 1, theory of solar cells and how the cells are measured were briefly discussed. Then, the history and the limitations of PVSCs were presented followed by the introduction of localized surface plasmon resonances (LSPR) by MNPs.

In Chapter 2, fabrication methods for high performance PVSCs were mainly focused. Due to the extreme sensitivity to moisture and air, the properties of perovskite films are considerably affected by the fabrication methods. It was found out that how the perovskite precursors are dispensed largely affects perovskite films. More explicitly, dynamic dispense and static dispense of a perovskite precursor ink during spin-coating were compared with each other. The dynamic dispense method, in which the perovskite

ink is dispensed while the substrate spins, leads to fast evaporation of precursor. The precursor is exposed to air for shorter period of time than the static dispense method, in which the ink is dispensed before spinning, resulting in optically better perovskite layers. However, some issues such as hysteresis have not been solved. Then, to minimize the exposure of the precursor ink to moisture in air during evaporation of a solvent, a novel method named SSVD was devised. Since drying of the precursor does not proceed during spin-coating due to short spinning time, the exposure to moisture in this step can be prevented. After drying and annealing under vacuum, ultrasmooth and semi-transparent perovskite layers can be obtained. The superior visual transparency of the perovskite films is caused by suppressed scattering from the smooth perovskite surface. The PVSCs prepared by the SSVD method exhibit high photovoltaic performances without hysteresis. By taking advantage of the good visual transparency of the perovskite films processed by SSVD, semi-transparent PVSCs were also fabricated using thin transparent electrodes consisting of silver and MoO_3 layers. The PCEs of 11.0% and 8.7% were recorded for the front and back light irradiation without hysteresis, suggesting that the SSVD method is beneficial for the realization of semi-transparent PVSCs.

In Chapter 3, application of MNPs to PVSCs was discussed. Despite developments of new methods to fabricate perovskite films, further increase in photocurrents is difficult as the currents tend to be saturated at ~20 mA cm^{-2}. The key to enhance the photocurrents further is to increase the incident photon-to-current conversion efficiency (IPCE) at the absorption edge of perovskite layers, at which light absorption is weak. Thus, MNPs were used for the enhancement of light absorption at the absorption edge of PVSCs. Because the wavelength range of plasmonic enhancement by typical MNPs based on silver and gold is in the visible region in which the IPCEs of PVSCs tend to be saturated due to strong light absorption, further enhancement of the performances of PVSCs by MNPs has been recognized to be difficult. In this respect, plasmon coupling modes between silver nanocubes (AgNCs) and a silver electrode film (ECPs) were used in the present PVSCs. LSPR wavelength of the ECPs is tunable by controlling the AgNC-electrode distance and the size of AgNCs. Tuning of the LSPR wavelength to the absorption edge resulted in enhancement of photocurrents and thereby PCE of PVSCs from 11.86 ± 0.88% to 13.3 ± 1.12%. The enhancement effect by ECPs is more conspicuous for the PVSCs with thin perovksite films as the amount of photons reaching the AgNCs is larger due to lower absorption by the perovskite layer.

In Chapter 4, ECPs were applied to semi-transparent PVSCs. In the semi-transparent PVSCs with ECPs, the silver electrode, the thickness of which is 10 nm, functions not

only for enhancement of light absorption as a part of the plasmonic structure exhibiting ECPs but also as a transparent electrode. Despite the thin metal film, the plasmonic coupling occurs between silver film and AgNCs, exhibiting strong plasmon scattering peaks in a long wavelength region (>600 nm) and intense optical near field in the entire range of wavelength examined. The semi-transparent PVSCs with ECPs showed good visual transparency compared to the cells without ECP exhibiting comparable photovoltaic performances because the wavelength of the plasmonic enhancement by ECPs was tuned out of the sensitive region of luminosity curve, which indicates human visual perception of brightness. For quantitative analysis of visual transparency, visual transparency index (VTI) was newly defined in which the light transmittance and human luminosity factors are both considered. Regarding above-mentioned semi-transparent PVSCs with and without ECPs, the PCE values were 9.73 ± 0.12 and 9.18 ± 0.19%, respectively, and the VTI values were 15.6 and 12.2%, respectively, supporting high visual transparency of the former cells.

By using novel methods developed here, semi-transparent PVSCs showed good visual transparency and high PCEs. However, the drawbacks such as air instability and toxicity still exist. It is considered that other approaches such as substitution of Pb with non-lead materials and development of an encapsulation technique are needed to overcome above-mentioned problems, enabling them to be commercialized.

The overall studies which were dealt with in this paper are not only confined to PVSCs. SSVD is expected to be applied to a variety of devices which require spincoating of moisture-sensitive precursors. Also, plasmonic tuning can be easily done by using ECPs. Thus, adjusting plasmonic regions to low absorption region of various types of solar cells and other plasmonic devices by ECPs can increase their performances. Therefore, it is expected that the techniques presented here will open doors to emerging photovoltaic cells.

Papers

1. Gyu Min Kim and Tetsu Tatsuma,
   "Semi-Transparent Solar Cells with Ultrasmooth and Low Scattering Perovskite Thin Films"
   The Journal of Physical Chemistry C, 2016, **120**, 28933-28938. (Chapter 2)

2. Gyu Min Kim and Tetsu Tatsuma,
   "Photocurrent Enhancement of Perovskite Solar Cells at the Absorption Edge by Electrode-Coupled Plasmons of Silver Nanocubes"
   The Journal of Physical Chemistry C, 2017, **121**, 11693-11699. (Chapter 3)

3. Gyu Min Kim and Tetsu Tatsuma,
   "Semi-transparent Perovskite Solar Cells Based on Human Luminosity Function"
   submitted. (Chapter 4)

Conferences

1. Gyu Min Kim and Tetsu Tatsuma,
   "Enhancement of Visual Transparency and Photocurrents in Semi-Transparent Perovskite Solar Cells by Electrode-Coupled Plasmons"
   The 78th JSAP Autumn Meeting, Japan, Sep. 2017 in preparation.

2. Gyu Min Kim and Tetsu Tatsuma,
   "Photocurrent Enhancement of Perovskite Solar Cells by a Plasmonic Waveguide Mode"
   The Electrochemical Society of Japan, Japan, Mar. 2017.

3. Gyu Min Kim and Tetsu Tatsuma,
   "Ultrasmooth Semi-Transparent Perovskite Solar Cells with Low Scattering and Photocurrent Enhancement Using Plasmonic Silver Nanocubes"
   Asian Photochemistry Conference (APC) 2016, Singapore, Dec. 2016.

4. Gyu Min Kim and Tetsu Tatsuma,
   "Ultrasmooth Perovskite Thin Film with Low Scattering and High Transparency by Short Spinning with Vacuum Annealing (SSVA)"
   Symposium of Center for Photonics Electronics Convergence, Japan, Apr. 2016.

Acknowledgments

It feels like yesterday when I came to the Tatsuma laboratory in April, 2014. Time has flown so quickly and I am already writing acknowledgements in my thesis. Despite confronting the language barrier and different cultural backgrounds as a foreign student, I have been able to enjoy spending time in Japan, thanks to everyone in Tatsuma laboratory who is kind and considerate.

At first, I would like to express my deepest gratitude to Professor Tatsuma. He, as a supervisor, has advised me of not just the research in graduate school but also how to spend pleasant and smooth life in Japan as a foreign student.

I am also thankful to Professor Fujioka, Professor Ishii, Associate Professor Sunada and Associate Professor Yagi for reviewing my doctoral dissertation and giving me valuable advices despite their busy schedules.

Nishi sensei, as an Assistant Professor, has managed Tatsuma lab smoothly so that the lab members including me could spend harmonious time. Thanks, Nishi sensei.

Technical support specialist Kuroiwa san is the very skillful person in many fields. When I was in trouble with many things, he always helped me and solved the problems regarding computers, experimental devices and even bicycles. I admire your magic skills. Thank you.

I really appreciate for the kindness of all other members in Tatsuma lab. Because Wu san started here in Tatsuma lab at the same time, we could discuss from the research to the life in Japan. Kao san and Ishida san have given me research advice as a Postdoctoral fellow. Also, I could cultivate fundamental knowledge more deeply from the discussion with Saito san. Akiyoshi kun is the most close lab member to me. Besides the research in the lab, Akiyoshi kun and I used to hang out such as playing darts or having a party so that I could get great memories. Despite the short time, memory with Lee san is also very precious. As a synthesis specialist in the lab, he is also very good at cooking. I could enjoy the real Korean foods here in Japan. Thanks again.

Lastly, I attribute all my precious experiences through life to my parents as they are always supporting me unconditionally.

Gyu Min Kim

謝辞

立間研究室での博士課程は私にとっては学問の探求や知識を得るだけではなく、日本の生活や文化を学ぶことができたかけがえのない貴重な経験でした。

まず、指導教官であり本論文の主査である立間徹教授に心より厚くお礼申し上げます。立間徹教授は研究生として初めて立間研究室に来てから今まで、外国から留学している未熟な私を日本での生活や研究が円滑に進むよう指導して下さって大変お世話になりました。

お忙しい中、私の博士論文を審査して貴重なアドバイスをして下さいました藤岡洋教授、石井和之教授、砂田祐輔准教授、八木俊介准教授にも心より感謝申し上げます。

西弘泰助教には研究の相談や助言から、多少手間がかかる書類準備にわたっていつも笑顔で親切に手伝って下さいました。本当にありがとうございました。

研究に関する討論や助言をいただいた Kao Kun-Che 外国人特別研究員、健康的に研究できるよう一緒に筋トレやランニングを定期的にして下さった石田拓也特任研究員にも大変感謝いたします。

いつも安心して実験できたのは深夜や週末にも関わらず、研究室を守って下さった黒岩さんのおかげでした。立間研究室のお母さんである黒岩さんありがとうございました。

問題なく楽しく博士課程を過ごせたのは、同じ時期に留学して博士課程を過ごしてきた Wu さんをはじめ、先輩、後輩の皆様のおかげです。特に未熟な私の日本語をいつも修正したり教えてくれた秋吉くん、立間研究室のブレインとして理論的な助言をしていただきました齋藤さん、同じ韓国からきて研究室生活を共にしました Lee さん、ありがとうございました。

最後に、快く海外での留学生活を応援してくれましたお父さん、お母さん、ありがとうございました。

金 揆昊(キム　ギュミン)